Observations of Intergalactic Heavy-Element Enrichment in the Early Universe

Thesis by

Robert Andrew Simcoe

In Partial Fulfillment of the Requirements

for the Degree of

Doctor of Philosophy

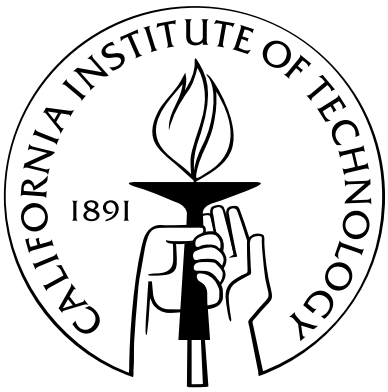

California Institute of Technology

Pasadena, California

2004

(Defended August 18, 2003)

© 2004
Robert Andrew Simcoe
All Rights Reserved

For Pat

Acknowledgements

I have always been fascinated both by the machinery of telescopes, and by the sky lying within their reach. In an age where knowledge has become ever more compartmentalized, it is rare to find an environment where one has the freedom to enjoy exploring a field from several angles. I will always be grateful to Caltech for trusting me with the opportunity to work both *on* and *with* some of the world's best telescopes.

My first few years here were spent in the Robinson sub-basement amongst the Palomar engineers. The LFC could not have been completed without their patient help and advice, and I will not forget their contributions. Special thanks are owed to Hal Petrie, Rich Goeden, Bob Weber, Bill Douglas, John Cromer and Ernest Croner for their constant interest in my progess, and their wealth of knowledge about the Hale telescope. Though not technically a Palomar engineer, John Yamasaki was always available to help with computing, electronic, or automotive questions. I greatly value his friendship both professionally and personally, and of course we will all miss his blowout barbequeues. Anne-Marie Hetman and Carlton Parker always graciously accomodated our changing schedules for the instrument shuttle and monastery reservations, and Brucato kept things running with a hand that was firm, yet fair and compassionate.

The Palomar mountain staff also made my job much easier. Karl Dunscombe and Rick Burruss helped the nights go by with their skill at teaching an old telescope new tricks. The day crew showed great diplomacy in the presence of sleepy and/or grumpy astronomers, keeping spirits light with their usual hijinks. I will always admire Bob Thicksten and Mike Doyle for their aptitude with equipment, and their professional commitment to the details needed to keep an observatory functioning smoothly. Palomar has been by far my favorite place to observe, because of its peaceful atmosphere, and its wonderfully eclectic people - despite the fact that one of the aforementioned staff (who shall remain nameless) nearly sent me plummeting from the prime focus cage. I hope future generations of astronomers can enjoy such a rich cast of characters.

I owe a few people particular thanks for encouraging my interest in instrument hardware. One of these is the LFC machinist, Gaston Araya. Gaston took a personal interest in seeing our project to completion, working sometimes at unusual hours, sometimes with hand-drawn schematics, and sometimes with nothing but a verbal description. Along the way, he gave me an informal apprentice-

ship in the art of machining and metalwork. We could never have built the instrument without his contributions, and I appreciate his dedication and friendship. Behind the scenes, Judy Cohen also boosted the project by lending us her husband, and by offering subtle encouragement and solidarity.

The most important thanks for my LFC experience go to Mark Metzger. Mark had great faith to entrust a new student with real responsibility for his instrument. He provided the motivation needed to complete the project quickly, but was patient with my learning curve. Mark taught me a tremendous amount about telescopes, observatories, instruments, and how to will a project to the finish line. I look back warmly on the time we worked together, and I wish him all the best.

Since the completion of LFC, my thesis work has relied heavily on data from the Keck telescopes, and I am greatly indebted to the competent staff in Waimea and on Mauna Kea for their assistance with these observations. In particular, I wish to thank Greg Wirth and Paola Amico for their help handling and testing a large narrowband filter we purchsed for LRIS. Back at Caltech, Keith Taylor was very helpful in advising me on the design of this filter, and has always taken the time to offer advice about my instrument questions.

Closer to home, the people in Robinson Hall have made my stay such a pleasure. Diane Fujitani has been unwaveringly scrupulous and kind in handling travel and financial arrangements. Gina Armas and Diane both put in countless rush orders for telescope parts, and Gina seemed to know the answer to just about any procedural question. They and the rest of the administrative staff were always interested in the students' life outside of astronomy - I experienced this particularly around the time of my wedding. I've enjoyed their occasional lunchtime company, not to mention Judith Mack's sumptuous filipino cooking. Cheryl Southard, Patrick Shopbell, and Anu Mahabal ran an airtight computing system, and Cheryl matched Pat and me up with the perfect cat. One of my favorite activities in Robinson was working on the rooftop telescope, and I gratefully acknowledge the departmental resources provided by Shri Kulkarni and Nick Scoville for fixing up this observatory.

My fellow students have been a source of cameraderie and welcome diversion. Several who have already graduated, especially Brad Behr and Roy Gal, helped us navigate the waters of a graduate education. I have always enjoyed the company and conversation of considerate officemates, including Kurt Adelberger, Josh Bloom, Alice Shapley, and Matt Hunt. Music making has been a vital activity outside the office, and it has been a pleasure to know George Becker and Ashley Borders, who generously shared their vocal talents and enthusiasm. Thanks also to the the St. Andrew's choir for not knowing anything about astronomy, and for keeping larger goals in our sights.

Chuck Steidel has been an important example for me over the past six years, and I am very grateful to have known him at Caltech. I appreciated his encouragement throughout my graduate career, from when I was a TA for his optics class, to when I worked on the LFC, to when I was finishing my thesis research. Through proximity to his scientific interests and to his group members' office space, I hope I have assimilated some of his aptitude for judging data, and learned to constantly

evaluate my work to maintain its focus on questions that are interesting.

Michael Rauch has been another mentor during my graduate education, and an engaging companion on many observing runs. I appreciated his careful readings and thoughtful comments on all of my writing, and his keen insights about the astronomical community and postdoc job market. Michael has a knack for thinking of creative projects, and I credit him for seeding many of the scientific ideas that were explored in this thesis. One regret during my time here is that we were never able to go hunting for archaeological artifacts out in the high desert.

I consider it a true privilege to have studied under Wal Sargent, and to have graduated from the title of "Nibsy" to "Team." Wal's breadth and depth of knowledge is matched by a singular, British fascination with people and their oddities. He knew when to teach, and when to let me discover on my own—providing constant feedback on my research, never hesitating to acknowledge when things were going well, and gently steering me back on course whenever I got caught up in boring details. I admire his talent for balancing larger science with the everyday routine of research, and for identifying interesting problems to pursue. Wal also recognized the importance of our exploits outside of Robinson Hall. He and Anneila seemed to enjoy a vicarious parenting role during my wedding planning, and Pat and I truly appreciated their generous support and help throughout. I enjoyed many a discussion with Wal about our shared appreciation of obscure music, and discovered that he values recordings largely in proportion to how eclectic they are. I now admit to a grudging appreciation of Elgar (I will remember "The Emprire" during the trio of Pomp and Circumstance #4), but I have to draw the line at the Bottesini concerti for double bass.

I feel fortunate to have shared particularly close friendships with a handful of people from Caltech, some starting even before our arrival on campus. Dave Vakil and Jon Sievers were terrific housemates and friends, and I have happy memories of dinners, bridge, and music-making at Mar Vista. Jon was also a critical member of our local contingent of the Red Sox diaspora. John Cartwright kept us all off balance with his unique wit, and I look up to his excellence both technically and scientifically. Alice Shapley has been a true friend, and a fun person with whom to share insights about the high redshift universe, the observing lifestyle, and other astronomers.

Finally, I wish to thank my family for all of their love and support from day one. Mom, Dad, and Tim all recognized this unusual interest of mine early on, and have encouraged me to follow it all the way while being models of how to lead a balanced life. And to my wife Pat, I could never ask for a better friend and companion in the whole world. Thanks for always being there.

Abstract

We present the results of a search for O VI absorption in the intergalactic medium (IGM) at $2 \lesssim z \lesssim 3$. The measurements are taken from a set of 7 quasars observed with Keck I/HIRES. We find two classes of O VI system in the high redshift IGM. The first class is more rare ($2-4$ per sightline) and also quite strong ($N_{\rm H\ I} \geq 10^{15.2}$). These systems resemble hot, collisionally ionized gas at high densities, and contain complex mixtures of H I and metals at a range of temperatures. Although we cannot measure the metallicities of individual strong absorbers, we estimate that the total population is enriched over 10 times above the level of the general IGM. We propose that the strong systems represent either accretion-shocked gas falling onto primitive large-scale structure, or (more likely) the remnants of high redshift galactic winds mixing into the IGM.

The second class of O VI absorber is much weaker, arising in low-density gas that is photoionized by metagalactic UV/X-ray radiation. We measure the metal content of these systems, down to densities of $\rho/\bar{\rho} \gtrsim 1.6$ relative to the cosmic mean. This corresponds to the filaments of the cosmic web, which contain over half of the baryons in the high redshift universe. We develop a new method to calculate the metallicity distribution function of the Ly-α forest using survival statistics. Carbon and oxygen are both distributed lognormally, with mean $\langle [O/H] \rangle \approx -2.85$ and scatter of $\sigma = 0.75$ dex. We observe no decline in metallicity toward lower densities, indicating that metals are mixed very efficiently within the filaments. Comparison with Population III and galactic wind enrichment models suggests that the enrichment was dominated by superwinds. We estimate that roughly half of all baryons in the IGM came into contact with metal-rich winds by $z \sim 2.5$. Using a "closed box" model of intergalactic enrichment, we estimate that early galaxies typically recycled $0.1-0.4\%$ of their mass back into the IGM as heavy elements prior to this epoch.

Contents

Acknowledgements **iv**

Abstract **vii**

1 Introduction **1**

1.1 Overview 1

1.2 Scientific Background 2

1.2.1 C IV in the Low-Density Intergalactic Medium 4

1.2.2 O VI in the Intergalactic Medium 5

1.3 Scientific Synopsis 7

2 Warm-Hot Gas at $z = 2.5$: Structure Formation and the Relics of Galactic Outflows **9**

2.1 Introduction 9

2.2 Observations and Data 11

2.2.1 Survey Strategy 11

2.2.2 Observations 13

2.2.3 Identification of O VI Systems 13

2.2.4 General Characteristics of Detected O VI Systems 15

2.2.5 Observed Properties of Individual Systems 18

2.2.5.1 Q1009+2956: $z = 2.253$ (Figure 2.1) 19

2.2.5.2 Q1009+2956: $z = 2.429$ (Figure 2.2) 21

2.2.5.3 Q1009+2956: $z = 2.606$ (Figure 2.3) 22

2.2.5.4 Q1442+2931: $z = 2.438$ (Figure 2.4) 23

2.2.5.5 Q1442+2931: $z = 2.623$ (Figure 2.5) 24

2.2.5.6 Q1549+1919: $z = 2.320$ (Figure 2.6) 26

2.2.5.7 Q1549+1919: $z = 2.376$ (Figure 2.7) 28

2.2.5.8 Q1549+1919: $z = 2.560$ (Figure 2.8) 29

2.2.5.9 Q1549+1919: $z = 2.636$ (Figure 2.9) 30

2.2.5.10 Q1549+1919: $z = 2.711$ (Figure 2.10) . . . 31
2.2.5.11 Q1626+6433: $z = 2.245$ (Figure 2.11) . . . 32
2.2.5.12 Q1626+6433: $z = 2.321$ (Figure 2.12) . . . 34
2.2.5.13 Q1700+6416: $z = 2.316$ (Figure 2.13) . . . 36
2.2.5.14 Q1700+6416: $z = 2.379$ (Figure 2.14) . . . 38
2.2.5.15 Q1700+6416: $z = 2.436$ (Figure 2.15) . . . 40
2.2.5.16 Q1700+6416: $z = 2.568$ (Figure 2.16) . . . 42
2.2.5.17 Q1700+6416: $z = 2.716$ (Figure 2.17) . . . 43
2.2.5.18 Q1700+6416: $z = 2.744$ (Figure 2.18) . . . 44
2.3 Analysis . . . 45
2.3.1 The Physical Environment of O VI Absorbers . . . 45
2.3.1.1 Pathlength and Gas Density Constraints . . . 45
2.3.1.2 Temperature Structure . . . 47
2.3.1.3 Multiphase Structure . . . 48
2.3.1.4 Constraints on Number Density and Cross Section . . . 52
2.3.1.5 Clustering Behavior . . . 53
2.3.2 The Contribution of Warm-Hot Gas to Ω_b . . . 56
2.3.3 Metallicity Constraints . . . 58
2.4 Discussion . . . 59
2.4.1 Shocked Infall on Large-Scale Structure? . . . 59
2.4.2 Tracer of Galactic Outflows at High Redshift? . . . 61
2.5 Summary and Conclusions . . . 62

3 The Distribution of Metallicity in the IGM at $z \sim 2.5$ 67
3.1 Introduction . . . 67
3.2 Observations . . . 69
3.2.1 Identification and Measurement of the O VI Systems . . . 70
3.2.1.1 O VI Sample Selection and Measurements . . . 70
3.2.2 Identification and Measurement of the C IV Systems . . . 71
3.2.3 Distribution in the H I /O VI and H I /C IV Planes . . . 72
3.3 Analysis . . . 74
3.3.1 Estimating [O/H], [C/H] for Ly-α Forest Lines . . . 74
3.3.2 Modeling Intergalactic Ionization Conditions . . . 74
3.3.3 Metallicites of Individual Lines, and Trends with $N_{\rm H\ I}$ . . . 77
3.3.4 Survival Analysis . . . 80
3.3.5 Corrections for False Positive O VI Identifications . . . 84

3.3.6 Final Estimates of the Metallicity Distribution 86
3.3.7 Cosmic Mass and Volume Fractions Probed by the Survey 90
3.3.8 Contribution of Intergalactic Oxygen and Carbon to Closure Density 94
3.4 Discussion 97
3.4.1 The Ultimate Closed Box? 100
3.5 Summary and Conclusions 103

A Comparison with Other Recent O VI Surveys **106**

B A Note on Models for the UV/X-Ray Ionizing Background **108**

C Effects of the X-Ray Background on Derived Oxygen, Carbon Abundances **110**

D The Large-Format Camera: A Wide-Field Imager for the Hale Telescope **112**
D.1 Introduction 112
D.2 Optical Elements, Vignetting, and Image Distortion 113
D.3 Detectors and Electronics 118
D.4 Mechanical Design 119
D.4.1 Dewar/Focal Plane 119
D.4.2 Shutter 121
D.4.3 Filter Wheel 122
D.5 Instrument Control 125
D.6 Performance 126
D.6.1 Mechanical 126
D.6.2 Electronics/Software 128
D.6.3 Optical 128
D.7 Summary 130
D.8 Team 131

List of Figures

1.1 The pixel-by-pixel optical depth method for detecting C IV in the Ly-α forest. 4

2.1 Velocity plot of the $z = 2.253$ O VI system in Q1009+2956 19
2.2 Velocity plot of the $z = 2.429$ O VI system in Q1009+2956 21
2.3 Velocity plot of the $z = 2.606$ O VI system in Q1009+2956 22
2.4 Velocity plot of the $z = 2.439$ O VI system in Q1442+2931 23
2.5 Velocity plot of the $z = 2.623$ O VI system in Q1442+2931 24
2.6 Velocity plot of the $z = 2.321$ O VI system in Q1549+1919 26
2.7 Velocity plot of the $z = 2.375$ O VI system in Q1549+1919 28
2.8 Velocity plot of the $z = 2.561$ O VI system in Q1549+1919 29
2.9 Velocity plot of the $z = 2.636$ O VI system in Q1549+1919 30
2.10 Velocity plot of the $z = 2.711$ O VI system in Q1549+1919 31
2.11 Velocity plot of the $z = 2.245$ O VI system in Q1626+6433 32
2.12 Velocity plot of the $z = 2.321$ O VI system in Q1626+6433 34
2.13 Velocity plot of the $z = 2.315$ O VI system in Q1700+6416 36
2.14 Velocity plot of the $z = 2.379$ O VI system in Q1700+6416 38
2.15 Velocity plot of the $z = 2.433/2.439$ O VI system in Q1700+6416 40
2.16 Velocity plot of the $z = 2.568$ O VI system in Q1700+6416 42
2.17 Velocity plot of the $z = 2.716$ O VI system in Q1700+6416 43
2.18 Velocity plot of the $z = 2.745$ O VI system in Q1700+6416 44
2.19 Observational constraints on the sizes and densities of the strong O VI absorbers . . . 46
2.20 Upper limits on the gas temperature of the strong O VI systems 48
2.21 CLOUDY predictions for $N_{\rm C\ IV}/N_{\rm Si\ IV}$, compared with observations 49
2.22 CLOUDY predictions of $N_{\rm O\ VI}/N_{\rm C\ IV}$, compared with observations 50
2.23 The two-point correlation function of the strong O VI systems 54

3.1 Scatter plot of individual O VI vs. H I measurements 73
3.2 Models of the UV ionizing background radiation spectrum 75
3.3 The ionization balances of oxygen and carbon in the low density IGM 76

3.4 Scatter plot of oxygen and carbon abundances as a function of H I column density . . 77
3.5 A montage of velocity plots for systems with unusually low oxygen abundances 79
3.6 Raw (uncorrected) Kaplan-Meier distribution of oxygen from the survey data 83
3.7 Illustration of the contamination correction for the Kaplan-Meier distribution 86
3.8 The cumulative distribution of oxygen abundances in the Ly-α forest 87
3.9 Comparison of the distributions of carbon and oxygen 88
3.10 The differential distribution function of intergalactic oxygen enrichment 89
3.11 Comparison of the raw KM distribution with a simple analytic model of intergalactic enrichment 90
3.12 The fraction of $\Omega_{\rm gas}$ contained in each decade of column density in the Ly-α forest . . 92
3.13 The enriched mass function of the IGM, calculated from O VI and C IV observations . 93
3.14 Comparison of observations with Population III and superwind enrichment models . . 98

D.1 Optical layout of the P200 Wynne corrector. 114
D.2 Vignetting as a function of LFC field angle 115
D.3 On-sky and display orientations of the LFC CCDs 116
D.4 Spot diagrams for the Wynne corrector 117
D.5 Defocused LFC image, showing mirror pinch 118
D.6 View of the LFC focal plane 120
D.7 Schematic of the LFC shutter assembly 121
D.8 LFC filters in mounting hardware 122
D.9 Cutaway of the total LFC mechanical assembly 123
D.10 LFC mechanical model mounted on the P200 prime focus pedestal 124
D.11 Screen shot of the LFC guider. 125
D.12 Stacked mosaic of I band LFC images 129
D.13 Optical distortions in LFC images 129

List of Tables

2.1 Quasars Observed for Strong O VI Systems 12
2.2 Summary of Observed Properties for Strong O VI Systems 16

3.1 Quasars Observed for Weak O VI Systems 69
3.2 Contribution of Intergalactic Metals to Closure Density 96

Chapter 1

Introduction

1.1 Overview

In the past decade, new observations have revealed evidence of early interactions between galaxies and intergalactic matter. After the first stars and galaxies were born, they immediately began to alter their surroundings, first by emitting ionizing radiation, and then by dispersing newly minted heavy elements into intergalactic space. When C IV was first discovered in the filaments of the intergalactic medium (IGM) at $z \sim 3$ (Meyer & York, 1987a; Cowie et al., 1995a; Tytler et al., 1995), it became clear that simple models where *in situ* chemical enrichment only occurred within galaxy haloes were incomplete. Metals fused in stars were somehow sown outside of galaxies in the early universe, signifying that the chemical feedback from early star formation was much more efficient than it is today. This vigorous recycling reveals a fundamental difference between typical galaxies at $z \gtrsim 2$ and those of the local universe. The aim of this work is to investigate the impact of early galaxies upon the large-scale IGM, using quasar absorption lines to study the dispersal and detailed distribution of heavy elements.

The bulk of the thesis describes a survey for intergalactic O VI absorption in quasar spectra at $2 \lesssim z \lesssim 3$. During this epoch, O VI was produced in two very different physical environments, providing complementary views of the relationship between early galaxies and intergalactic matter. The strongest O VI absorbers were formed in dense, hot gas which was probably collisionally ionized. Unlike the global IGM, they contained heavy concentrations of metals in both low and high ionization states. We propose that this mixture of ionization conditions resulted from the shock heating of gas followed by cooling, as high redshift galaxies interacted with the surrounding IGM. Chapter 2 (reprinted from the *Astrophysical Journal*, V. 578, p.737, written with W. Sargent and M. Rauch) details the strong systems' absorption properties and our interpretation of the observations. In Chapter 3 (also with W. Sargent and M. Rauch, reprinted from the *Astrophysical Journal*, V. 606, p.92), we describe the second observed variety of O VI absorption. These lines arose in cooler, photoionized gas typical of the global, tenuous IGM (i.e., the Ly-α forest). The trace amount of

heavy elements in the forest must have been deposited prior to $z \sim 2.5$; these elements therefore contain a fossil record of *past* galaxy/IGM interactions.

The primary scientific content of the thesis is contained in Chapters 2 and 3, and related Appendices. Following these sections, I have included in Appendix D a brief description of the Palomar Large Format Camera (LFC), a wide field imager for the 200 inch Hale telescope. I took part in the design and construction of this instrument for two years under the supervision of M. Metzger.

1.2 Scientific Background

In the early days of quasar absorption line research, most of the high redshift IGM was presumed to be chemically pristine. Heavy element absorption lines were observed in the relatively rare Damped Ly-α ($N_{\rm H\ I} \gtrsim 10^{20}$) and Lyman limit ($10^{17} \lesssim N_{\rm H\ I} \lesssim 10^{20}$) systems, but it was already suspected that these were related to galaxies and enriched with locally produced heavy elements. The spectral regions between these rare systems were suffused with weaker H I absorption lines, referred to as the Ly-α forest. The forest lines did not appear to be associated with high redshift galaxy haloes. At the time, they were thought to represent pressure confined pockets of zero metallicity gas, since distinct H I features could be seen in the quasar spectra with no corresponding heavy element absorption (Sargent et al., 1980).

This first model of the IGM—with exactly three varieties of absorption system, and chemical evolution occurring only on local scales—was soon challenged both by theory and by new observations. First, numerical simulations of structure formation began to blur the distinction between Damped absorbers, Lyman limit systems, and the Ly-α forest. According to the new models, all absorption systems were peaks in a smoothly fluctuating H I density field, and the sizes and shapes of cosmic structures depended on their density enhancement relative to the cosmic average, $\rho/\bar{\rho}$. Damped Ly-α systems and galaxies were highly overdense at $\rho/\bar{\rho} \gtrsim 10^5$; the slightly weaker Lyman limit systems occupied the $1000 \lesssim \rho/\bar{\rho} \lesssim 10,000$ range. The highest density peaks were crudely spherical, with gas density profiles that decreased with radius out to $\rho/\bar{\rho} \sim 10$ (at ~ 50 physical kpc). Below $\rho/\bar{\rho} \sim 10$ the cloud topology changed significantly. At $z \sim 2-4$, gas at $1 \lesssim \rho/\bar{\rho} \lesssim 10$ formed an interconnected network of filaments, which produced the absorption lines of the Ly-α forest. Over 90% of the baryons in the universe were contained in these slightly overdense regions at $z \geq 2$, though they occupied only a small fraction of the cosmic volume. Most of the space was permeated by large voids with densities slightly below $\rho/\bar{\rho} = 1$. Thus the entire menagerie of absorption systems was collected into a single model, founded on the basic physics of gravitational structure formation (Cen et al., 1994; Hernquist et al., 1996; Zhang et al., 1995; Davé et al., 1999).

At the same time, new observations uncovered evidence of extensive C IV absorption in the Ly-α forest at $z \sim 3$. Early work by Meyer and York (1987a) was followed by the first Keck HIRES

observations, which revealed C IV in most forest lines with $\rho/\bar{\rho} \gtrsim 7$ ($N_{\rm H\ I} \geq 10^{14.5}$; Cowie et al., 1995a; Tytler et al., 1995). These systems were 2-3 orders of magnitude weaker than the weakest Lyman limit systems, and much less dense than a typical galaxy halo. The discovery of metals in cosmic filaments suggested that the first era of chemical enrichment happened early, and was much more efficient than originally thought.

Two principal hypotheses emerged to explain the new observations. In one scenario, the intergalactic metals were forged in isolated "Population III" stars at high redshift ($z \gtrsim 10$; Ostriker & Gnedin, 1996). With masses exceeding $100 M_{\odot}$ (Abel et al., 2002; Bromm et al., 2002), these stars evolved quickly and exploded as supernovae while the average distance between haloes was relatively small (due to the $(1+z)^{-1}$ scaling for cosmic expansion). After this initial burst, the Population III stars stopped forming and left little observational signature except for their ejected heavy elements (Mackey et al., 2003). These metals would have been smoothly distributed throughout the cosmic volume, since they would have had less distance to fill between adjacent haloes, and more time to mix.

In the competing hypothesis, the enrichment era was more recent ($z \lesssim 10$), and was powered by starburst-driven outflows from massive galaxies. At these epochs galaxies were manufactuing mostly Population II stars with initial masses in the $\sim 1 - 30 M_{\odot}$ range, according to a Salpeter-like initial mass function (though perhaps slightly skewed toward high masses; Prochaska et al., 2003; Pettini et al., 2002). However, the overall star formation rate was much higher than at present, and during bursts of activity the coordinated energy of multiple supernovae ejected metal-rich material into the IGM. The "superwind" phenomenon has been observed in local starburst galaxies (Lehnert & Heckman, 1996; Heckman et al., 2001; Martin et al., 2002), and also in the spectra of many high redshift objects (Pettini et al., 2001). Spatial correlation of Lyman break galaxies with C IV absorption at $z = 3$ even reveals an excess of metal-rich material in the neighborhoods of high redshift galaxies (Adelberger et al., 2003), and the kinematics of C IV systems suggest that the metals are stirred periodically on 100 Myr timescales (Rauch et al., 2001). On the largest scales, this type of enrichment should leave a patchwork of high metallicity regions, with heavy element abundances declining away from galaxies toward the sparse regions of the IGM.

The intergalactic metallicity field thus bears the signature of early star formation in the universe. Abundance gradients toward lower density imply that recent superwinds dominated the intergalactic enrichment, while spatially uniform abundances imply that the metals were deposited by ancient Population III stars. To test these predictions, one must measure abundances over a wide range of densities, particularly in the rarefied regions of the IGM far from galaxies. Traditionally, C IV observations have been used for these measurements. However, in regions with $\rho/\bar{\rho} \lesssim 6 - 7$, even the best Keck spectra lack the sensitivity to detect individual C IV lines in the IGM, so more sophisticated methods are required to distinguish between the two enrichment scenarios.

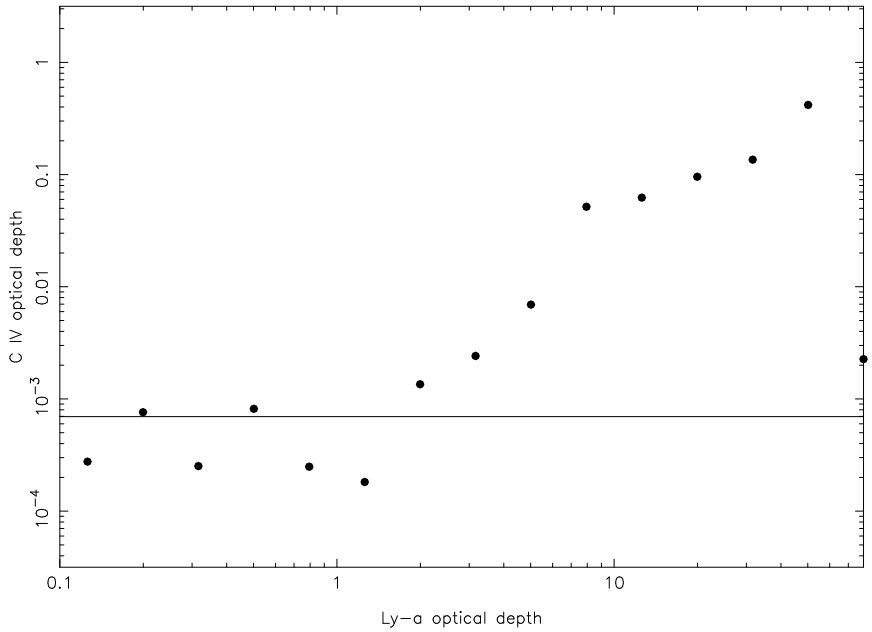

Figure 1.1 A pixel-by-pixel correlation of the optical depths of Ly-α and C IV in the spectrum of Q1549+1919.

1.2.1 C IV in the Low-Density Intergalactic Medium

To overcome this limitation, several groups developed statistical methods to extract weak C IV signals from high-resolution spectra, leading to contradictory claims. Lu et al. (1998) generated an ultra-high S/N, average C IV profile for the low-density IGM by stacking the C IV regions of many Ly-α forest lines. No C IV was detected in the composite, suggesting a sharp decline in metallicity away from local enrichment sources. However, this technique has been criticized for assuming $z_{\rm C\ IV} = z_{\rm H\ I}$, since a slight offset between the H I and C IV velocity centroids could smear out a true signal in the stacked data. These H I /C IV velocity offsets have been observed in strong H I systems (with $\sigma_v \sim 10 - 20$ km/s), although anecdotal evidence suggests that they are much smaller in weaker H I lines typical of the Ly-α forest. Nevertheless, the shift-and-stack approach has mostly fallen out of favor as a tool for measuring intergalactic abundances.

A more popular method has been to search for pixel-to-pixel correlations between the optical depths of Ly-α and C IV throughout the length of a spectrum. The idea was first introduced by Cowie and Songaila (1998) and has been refined since; its basic principle is illustrated in Figure 1.1. Data points are generated by dividing the Ly-α forest pixels into bins of varying $\tau_{\rm Ly\alpha}$. Then, for each Ly-α pixel the corresponding $\tau_{\rm C\ IV}$ is measured at the same redshift, and the *median* $\tau_{\rm C\ IV}$ is plotted for each bin of $\tau_{\rm Ly\alpha}$. A positive correlation between the Ly-α and C IV optical depths indicates a C IV detection, which can be seen in Figure 1.1 for $\tau_{\rm Ly\alpha} \geq 1$. At lower Ly-$\alpha$ strengths, the correlation flattens out due to noise in the C IV spectral region. The solid line indicates the

median optical depth of all C IV pixels; it serves as a rough indicator of the uncertainty due to spectral continuum placement.

Based on this technique, several authors have claimed detections of metals at very low cosmic densities, even at $\rho/\bar{\rho} \lesssim 1$. However, this measurement can be difficult to interpret for several reasons:

1. The Ly-α optical depths characteristic of voids lie below $\tau_{\mathrm{Ly}\alpha} = 1$, where the signal becomes much smaller than the noise plateau.

2. The C IV optical depth at low densities is $\lesssim 10^{-3}$, or just 0.1% below the continuum level. The HIRES echelle shows order-to-order variations in the continuum of a few percent between exposures. These are typically corrected by hand, and the corrections are much larger than the signal being measured.

3. The mapping between overdensity and Ly-α optical depth is not one to one: many of the pixels at $\tau_{\mathrm{Ly}-\alpha} \approx 1$ are actually from wings in the profiles of stronger lines.

4. The pixel method smooths the C IV strength over the whole spectral path. Thus a spectrum with a few strong, systems cannot easily be distinguished from one with many weak ones. The effects of strong outliers are lessened by evaluating the median $\tau_{\mathrm{C\,IV}}$ rather than the mean. However, we have tested this assumption using our highest quality data, and found that even the median can be biased by outliers at the 0.1% level required for this measurement.

Significant work has gone into understanding the meaning and reliability of the pixel-to-pixel results, including a recent sophisticated analysis that relies on hydrodynamic simulations to estimate [C/H] (Aguirre et al., 2002; Schaye et al., 2003). At $\rho/\bar{\rho} \sim 6-7$ ($N_{\mathrm{H\,I}} \geq 3 \times 10^{14}$)—where direct measurements of individual C IV lines can be compared to the pixel statistics—all methods seem to agree on an intergalactic carbon abundance of $[C/H] \sim -2.5$ [1] (Ellison et al., 2000; Davé et al., 1998; Songaila & Cowie, 1996). At lower densities, pixel methods strongly suggest the presence of additional metals, but their detailed interpretation is difficult.

1.2.2 O VI in the Intergalactic Medium

The reason low density C IV measurements are so difficult is that below $\rho/\bar{\rho} \sim 5$, intergalactic carbon atoms are photoionized to C V and higher states by the integrated light from quasars. In fact, most of the C IV in the IGM has already been observed. In very low density environments, chemical species with higher ionization potential will predominate, and the O VI ion becomes the best candidate for abundance measurements. Yield calculations for Type II and pair-instability supernovae show that

[1] According to standard convention, $[X/H]$ represents the log of the abundance (by number) for element X relative to solar, i.e., $[X/H] = \log(X/H) - \log(X/H)_{\odot}$.

oxygen should be manufactured in large quantities in the early universe (Woosley & Weaver, 1995; Heger & Woosley, 2002). When these oxygen atoms are distributed into the sparse IGM, they are quintuply ionized by the same radiation field that ionizes C IV to C V . The O VI ion produces a doublet with large oscillator strength at a rest wavelength of 1032/1037Å . It is therefore visible in ground-based optical spectra at $z \gtrsim 2$, but it is mixed in with the stronger H I absorption lines of the Ly-α forest itself. Thus, O VI observations allow us to measure intergalactic abundances *directly* near $\rho/\bar{\rho} \sim 1$, where only the stacking and pixel methods can be used for C IV. However, any reliable study of high redshift O VI must include strategies to minimize, and to understand the effects of confusion from Ly-α forest lines.

Several individual O VI systems have been observed in intermediate redshift HST/FOS spectra (e.g., Burles & Tytler, 1996; Jannuzi et al., 1998; Rollinde et al., 2001), but the first systematic O VI search at high redshift was undertaken by Davé et al. (1998) at $3 \leq z \leq 3.6$ using a spectrum of Q1422+231. These authors did not detect any distinct O VI doublets because of heavy blanketing from the forest at this redshift, although their application of the pixel-optical-depth technique to O VI yielded evidence for low level oxygen enrichment (see also Schaye et al., 2000).

Around the same time, O VI absorption was first detected in the local IGM with HST/STIS and FUSE (Tripp et al., 2000). These low-redshift observations were never *designed* to assay the low density IGM for photoionized metals. Rather, they focused on collisionally ionized O VI, which is produced within a narrow range of gas temperatures near $T \sim 300,000$ K. Considerable importance has been attached to searches for a "warm-hot" phase of the IGM - which is hotter than the Ly-α forest ($T_{\rm Ly\alpha} \sim 10,000$ K) but cooler than intracluster gas ($T_{\rm ICM} \sim 10^7$ K). Cosmological simulations predict that $\sim 30\%$ of all baryons may have been heated into the warm-hot range by $z = 0$, as pre-enriched gas settled onto large scale structure and encountered accretion shocks (Cen & Ostriker, 1999; Davé et al., 2001; Cen et al., 2001). Warm-hot gas cannot be detected in Ly-α absorption because hydrogen is almost entirely collisionally ionized above $T \sim 100,000$ K. Since gas at the low end of the warm-hot temperature range can be detected in O VI absorption, these systems have been advertised as the only probe of a significant baryon reservoir in the local universe (Tripp et al., 2000; Savage et al., 2002).

In fact, collisionally ionized O VI should be found behind many types of shocks propagating at several hundred km s^{-1} (Dopita & Sutherland, 1996). Since galactic winds travel at these speeds, shock-heated O VI can also be produced *within superwinds themselves.* Models predict that this O VI will be found near the edges of outflows, where hot outrushing gas mixes with cooler ambient material (Heckman et al., 2001; Begelman & Fabian, 1990; Edgar & Chevalier, 1986). This has been observed with FUSE in several nearby dwarf starburst galaxies, including NGC1705, NGC4214, and NGC3310 (Heckman et al., 2001; Strickland, 2001). Similar galactic outflows may have distributed the metals seen in the high redshift IGM. If low-luminosity dwarf galaxies played an enhanced

role in early enrichment, the absorption lines from shocked gas at high redshift could be the only observationally accessible signature of their feedback.

We have shown how O VI can be generated in the IGM through photoionization and collisional ionization. At high redshift, the weak photoionized O VI is produced in the low density Ly-α forest and traces the metal content of cosmic filaments. Stronger collisionally ionized systems are produced in two important situations: shock-heated gas falling onto structure, and the wake of supernova-driven galactic outflows. Each of these three environments offers a different perspective on the interaction between early galaxies and intergalactic matter.

1.3 Scientific Synopsis

To explore the implications of these interactions, we have obtained a large sample of deep, high-resolution spectra to study the distribution of intergalactic O VI at $2 \lesssim z \lesssim 3$. This is the only redshift range where one can detect distinct O VI lines using large, ground-based telescopes. At lower redshifts, the O VI doublet shifts into the UV and must be observed using satellites with smaller collecting areas. Above $z \gtrsim 3$, blending from the Ly-α forest becomes too severe, since for $z \gtrsim 1.5$ the density of Ly-α lines scales as $(1+z)^{2.8}$ (Kim et al., 2001). Even in our redshift window, it is a considerable challenge to disentangle the O VI absorption signal from the Ly-α forest.

In the high redshift sample, we detect *both* varieties of O VI: the dense collisionally ionized systems, and the cooler photoionized metals of the Ly-α forest. In Chapter 2 we discuss the properties of the warm-hot O VI systems. It is difficult to determine definitively whether these are associated with galactic outflows or structure formation. We favor the wind hypothesis, since most haloes at high redshift are not yet massive enough to shock heat accreted mass to $T \sim 300,000$ K. Also, the O VI systems' chemical and thermal properties would be unusually complex for gas that was pre-enriched in the distant past and has just begun to fall back onto structure.

Chapter 3 presents an analysis of the global distribution of heavy elements at $z \sim 2.5$. Our results extend to $\rho/\bar{\rho} \sim 1.6$ (i.e., nearly all of the cosmic filaments), and use only *direct* measurements of weak O VI and C IV in Ly-α forest systems. Often, we do not detect O VI in systems where we had expected to see it, based on the predictions of simple uniform enrichment models of the IGM. To assess the significance of these non-detections, we develop a new technique to calculate the full metallicity distribution function of the IGM, where prior studies had calculated only the mean or median metallicity. We compare our abundance estimates to recent models of Population III and superwind enrichment from the literature, and calculate the typical metal yield of galaxies prior to $z \sim 2.5$ using a closed box model of intergalactic chemical enrichment.

Combining these results with recent theoretical work on Population III and superwind enrichment, a picture emerges to describe the chemical structure of the IGM at $z \sim 2.5$. Within the

filaments of the cosmic web, there is significant random scatter in the metallicity field, but no strong overall trend of decreasing metallicity with H I column density. The abundance distribution peaks near $Z/Z_{\odot} = 10^{-2.8}$, which is over an order of magnitude above recent theoretical limits on the Population III metal production budget. Numerical simulations of realistic superwinds at high redshift match the observed abundances. We conclude that essenatially all of the heavy elements observed in the filaments were deposited by galactic winds, and that these winds have mixed very efficiently into their surroundings.

Our yield calculations indicate that on average, high redshift galaxies recycled $0.1 - 0.4\%$ of their mass back into the IGM as heavy elements. This feedback efficiency is qualitatively similar to what is seen in local dwarf starburst galaxies. At high redshift, galactic outflows appear to be common. They are observed directly in galaxy spectra, and possibly indirectly as a deficiency of H I and an excess of C IV in quasar sightlines passing near galaxies. We have discovered shock-heated O VI mixed in with lower ionization carbon and silicon lines in many of the stronger systems of the Ly-α forest. We propose that these absorbers, and indeed a significant fraction of Ly-α forest lines with $N_{\rm H\ I} = 10^{15} - 10^{17}$, arise in regions where actively evolving superwinds are mixing chemicals and kinetic energy into the IGM.

Our findings apply primarily to matter in cosmic filaments; the enrichment patterns in the voids could be quite different. However, the filaments of the Ly-α forest contain most of the baryonic mass in the high redshift universe. Hence our results imply that a large fraction of the baryons (we estimate $30 - 60\%$) have either been processed through a galaxy or mixed with material that has done so in the first 3 Gyr after the Big Bang.

Chapter 2

Warm-Hot Gas at $z = 2.5$: Structure Formation and the Relics of Galactic Outflows [1]

2.1 Introduction

Within the last decade, a picture of the evolving intergalactic medium has emerged whereby the growth of baryonic structure is described through the collapse of gravitational instabilities (Cen et al., 1994; Miralda-Escude et al., 1996; Hernquist et al., 1996; Zhang et al., 1995; Petitjean et al., 1995). According to this model, baryonic gas exists in several different states. At high redshift, most of the gas is found in the Ly-α forest, which is generally distributed and relatively cool at $T \sim 10^4$ K, its temperature governed by photoionization heating. Beginning at $z \sim 2.5 - 3$, an increasing fraction of the baryons undergo a period of shock heating as they fall onto large-scale structure. The cooling timescale for this shock-heated phase is long, so by $z = 0$ as many as 30% of the baryons may accumulate in gas with temperatures between $10^5 - 10^7$ K (Cen & Ostriker, 1999; Davé et al., 2001; Fang & Bryan, 2001). The remaining 70% of the baryons at the present epoch have either never been shock heated above $T \sim 10^4$ K, or they have cooled much further into highly overdense structures near the junctures of filaments. In these very dense environments the effects of local processes begin to play an important role.

This picture must be incomplete at some level, since a substantial fraction of the universe is already metal-enriched by $z = 4$ (Meyer & York, 1987b; Rauch et al., 1996a; Cowie et al., 1995a; Tytler et al., 1995), and the enrichment process is not included in models relying solely on gravitational instability. Models of metal absorption lines in a hierarchical scenario (Haehnelt et al., 1996; Hellsten et al., 1998; Cen & Ostriker, 1999; Fang & Bryan, 2001) have relied either on a very early ("Population III") pre-enrichment phase or on relatively simple global recipes for calculating

[1] Reprinted from the *Astrophysical Journal*, V. 578, p. 737 (Copyright 2003, The American Astronomical Society).

stellar feedback. Ongoing metal enrichment at the epoch where we observe the metal absorption systems may be important, and galactic winds (one of the possible enrichment mechanisms) have been observed at both low and high redshift (Lehnert & Heckman, 1996; Franx et al., 1997; Pettini et al., 2001). Moreover there are hints that metal enriched gas at $z = 3$ is turbulent at levels which require energy input only $10 - 100$ Myr prior to the epoch of observation (Rauch et al., 2002).

Two of the principal phases of the IGM have been extensively studied because they are easily observed in the absorption spectra of high redshift QSOs as the Ly-α forest (caused by the cool filaments) (Kim et al., 2001, 1997; Rauch et al., 1997a; McDonald et al., 2000) and Lyman limit/Damped Ly-α systems (caused by the regions of highest overdensity) (Prochaska & Wolfe, 2000). However, the hot phase of the IGM with $T > 10^5$ K is comparatively poorly understood, because at such high temperatures the collisional ionization of Hydrogen becomes significant, rendering Ly-α less effective for tracing structure. A budget of the content of the IGM based on Hydrogen absorption alone will therefore underrepresent the contribution of hot gas to the baryon total.

A more accurate account of the hot phase may be made using species with higher ionization potential than Hydrogen. The O VI 1032/1037Å doublet has long been recognized as a prime candidate for this purpose for several reasons (Chaffee et al., 1986; Davé et al., 1998; Rauch et al., 1997a). First, the intergalactic abundance of oxygen is higher than that of any element other than Hydrogen and Helium. Second, highly ionized oxygen in the form of O VI, O VII, or O VIII is among a small number of effective tracers for gas in the $T = 10^5 - 10^7$ K range typical of shocked environments in cosmological simulations (Cen & Ostriker, 1999; Davé et al., 2001; Fang & Bryan, 2001). Among these ionization states, only O VI is visible in ground-based optical spectra of QSOs, at redshifts above $z \geq 2$.

Further interest in O VI has revolved around its predicted effectiveness for tracing heavy elements in the very low density IGM - an environment very different from the shock-heated one described above. At $T \sim 10,000 - 40,000$ K, the gas in this diffuse phase is too cold for collisional ionization to produce highly ionized species such as O VI. However, its density is sufficiently low (only a few times the mean) that O VI may be produced through photoionization from the intergalactic UV radiation field.

Based upon recent simulations, one expects observable levels of photoionized O VI to exist in Ly-α forest lines with column densities in the range $13.5 < \log N_{\rm H\ I} < 15.0$ (Hellsten et al., 1998; Davé et al., 1998). This O VI absorption can therefore probe the metal content of gas with densities below the range in which C IV is most sensitive. Statistical studies involving the pixel-by-pixel comparison of optical depths of Ly-α and C IV have provided some evidence of widespread enrichment of the IGM to even the lowest column densities (Cowie & Songaila, 1998; Songaila & Cowie, 1996; Ellison et al., 2000; Aguirre et al., 2002), and more recently very similar techniques have been used to infer the statistical presence of O VI associated with the forest (Schaye et al., 2000). But to date the

number of direct metal line detections associatied with $\log N_{\rm H\,I} < 14.5$ Ly-α lines is small, so the presence of warm photoionized O VI could help validate the assumption of widespread enrichment used in some of the simulations described above.

Considerable attention has been given to the recent discovery of O VI absorbers in the local neighborhood ($z < 0.3$) using HST/STIS and the FUSE satellite (Tripp et al., 2000; Richter et al., 2001; Savage et al., 2002). Much of the early interpretation of these results has involved the difficult job of distinguishing whether particular absorption systems represent the warm photoionized, or hot collisionally ionized variety of O VI. Early indications show that the low redshift population is mixed, with a slight majority of collisionally ionized systems. Regardless of the physical interpretations of these individual lines, it seems clear that the baryonic content of the Warm-Hot IGM may be significant at low redshift - possibly as much as 30% of Ω_b.

In this paper, we describe the results of a survey for O VI at high redshift, along the lines of sight to five bright quasars observed with the Keck I telescope and HIRES spectrograph. Our survey covers the range $2.2 < z < 2.8$, which was chosen to optimize the tradeoff between signal-to-noise and contamination from the Ly-α forest. We estimate the contribution of warm-hot gas to the total baryon budget at high redshift, and attempt to identify the physical environments of the O VI systems.

In Section 2 we describe our observing strategy and methods, and provide brief descriptions of the properties of individual O VI systems. In Section 3 we characterize the physical envronment of O VI absorbers, and calculate the contribution of warm-hot gas to the baryon total. In Section 4 we discuss possible production mechanisms for the highly ionized gas in the context of cosmological simulations and galaxy feedback on the IGM. Throughout, we assume a spatially flat universe with $\Omega_M = 0.3$, $\Omega_\Lambda = 0.7$, and $H_0 = 65$ km/s/Mpc.

2.2 Observations and Data

2.2.1 Survey Strategy

Detection of the O VI 1032/1038Å doublet from the ground presents a particular challenge, as the 3000Å atmospheric cutoff (as well as the decreased sensitivity of the HIRES spectrograph blueward of 3200Å) limits searches to $z > 2$. At these redshifts, O VI is buried in both the Ly-α and Ly-β forests, whose densities increase rapidly with increasing redshift for $z > 1.3$ (Kim et al., 2001). The competition between increasing signal-to-noise ratio toward the red and decreasing contamination toward the blue led to our selection of $2.2 < z < 2.8$ as a target range for the survey. The lower bound was set by instrument sensitivity, and the upper bound was derived through consideration of existing studies of line densities in the Ly-α forest (Kim et al., 1997, 2001). The availability of UV bright QSOs in the spring observing season led us to the selection of the five sightlines listed in

Table 2.1. Quasars Observed for Strong O VI Systems

Object	Total λ coverage (Å)	z_{em}	Δz_{OVI}[1]	ΔX_{OVI}[1,2]
Q1009+2956	3200-6075	2.62	2.10-2.56	1.48
Q1442+2931	3200-6150	2.63	2.19-2.57	1.24
Q1549+1919	3160-6084	2.83	2.06-2.77	2.31
Q1626+6433	3300-6180	2.32	2.15-2.26	0.36
Q1700+6416	3250-6140	2.72	2.20-2.66	1.51
Total:				6.90

[1]Corrected to exclude regions within 5000 km/s of the QSO emission redshift.

[2]Does not include the effects of spectral blockage; see Section 2.3.1.4 for further discussion of this point.

Table 2.1, with $2.32 < z_{em} < 2.83$.

Recent observations resulting in the discovery of O VI in the low redshift universe (Tripp et al., 2000; Richter et al., 2001; Savage et al., 2002) were largely motivated by the desire to trace the hitherto undetected warm-hot (i.e. $10^5 - 10^7$) component of the IGM, which should be most prominent at low redshift. However, a major factor in the success of these surveys is the low level of contamination from the Ly-α forest near $z = 0$. In particular, below $z = 0.17$ the observed wavelength of the O VI doublet is below 1216Å, so the only H I contamination comes from higher order Lyman transitions at higher redshift. These are less numerous than Ly-α and can often be easily removed by fitting the corresponding Ly-α profile. The surveys cited above generally are limited to $z \leq 0.3$, so a portion of their pathlength has no Ly-α forest absorption, with the remainder showing contamination at levels $2 - 3$ times lower than at $z = 2.5$.

While the increase in Ly-α forest absorption makes the detection of unblended O VI more difficult at high redshift, the large absorption pathlengths sampled by the more distant surveys offset this effect to some extent. For a given redshift interval dz, the cosmology-corrected absorption pathlength

$$dX = \frac{(1+z)}{\sqrt{\Omega_M(1+z) + \frac{\Omega_\Lambda}{(1+z)^2}}}\, dz, \quad (\Omega = 1) \tag{2.1}$$

is 3.3 times longer at $z = 2.5$ than at $z = 0$ for $(\Omega_M, \Omega_\Lambda) = (0.3, 0.7)$. High redshift surveys are therefore less clean, but sample a much larger volume than their low redshift counterparts. The total pathlength of our survey is $\Delta z = 2.12, \Delta X = 6.90$ for the above cosmology, which represents a sixteenfold increase over the total distance of all published local surveys for O VI (Savage et al., 2002). In practice we can detect O VI over $\sim 40\%$ of this range because of blending with Ly-α forest

lines (See section 2.3.1.4).

2.2.2 Observations

Four of the five objects in our program were observed in excellent conditions over the nights of UT 16-17 March 2001, using the Keck I telescope and HIRES spectrograph with the UV blazed cross-disperser installed. Q1700+6416 had been observed on UT 24 March 1998 and UT 13-15 April 1999 in the blue at high S/N and was therefore also included in our sample. All exposures were taken through a 0.86 arcsecond slit providing a measured resolution of 6.6 km/s, and the slit was fixed at the parallactic angle throughout.

The raw CCD frames were processed and traces extracted to produce 2-D echelle spectra using the "makee" reduction package written by Tom Barlow. Continua were then fit to the individual exposures on an order-by-order basis, and the unity-normalized spectra were combined with inverse variance weighting onto a common wavelength scale. When combining the data, we also included data taken previously with HIRES using the red cross-disperser. The final added spectra have typical S/N ratios between 20-30 per pixel (35-50 per resolution element) in our O VI redshift window, as well as complete coverage of Ly-α , Ly-β , and several other highly ionized species such as N V , Si III , Si IV , and C IV at even higher signal-to-noise ratios.

2.2.3 Identification of O VI Systems

The reduced spectra were searched by eye for the O VI doublet at the correct wavelength separation and optical depth ratio, to create an initial sample of candidate O VI systems. At this stage, we did not subject our search to the constraint that there be absorption from any other ions at the same redshift as O VI. Each potential system from this list was then fit as a blend of Voigt profiles using the VPFIT software package to verify that the profile shapes were adequately matched in the 1032Å and 1037Å components. Other ions identified at the same redshift were fit in a similar fashion. In the case of H I , we included as many transitions as possible from the Lyman series in our fits. Typically this included at least Lyα, β, γ, but in come cases reached up to Ly-11.

This procedure resulted in the identification of 24 pairs of lines whose absorption properties are consistent with those of O VI. However, given the density of the Ly-α forest at our working redshift, one must carefully consider the possibility of contamination due to chance Ly-α pairs masquerading as O VI. Previous searches for O VI lines in HST/FOS spectra (Burles & Tytler, 1996) found a high rate of chance coincidences in monte carlo simulations, but our increase in resolution by a factor of ~ 30 should significantly decrease this source of false positive identifications.

To estimate the amount of contamination in our initial sample of 25 systems, we performed a second search of the reduced spectra for pairs of lines that are identical to the O VI doublet in every

way except that the optical depth ratio of the two components is reversed. This test should be robust, as it identically reproduces the Ly-α forest contamination, clustering, metal contamination, and S/N properties of the real search process. Using this method, we were able to identify 7 "false" systems that met the reversed doublet criteria. Our "true" O VI sample contains over three times as many identifications as this false sample, which implies that the true sample is dominated by real O VI detections rather than spurious pairings of Ly-α forest lines. With no other input to the search/selection criteria, we expect the O VI sample to be contaminated by false pairs at the $\sim 25-30\%$ level. However, it is possible to improve significantly on this figure through consideration of the properties of the individual systems we have detected.

In particular, the false systems are not found near environments populated by other heavy elements, or even Ly-α in many cases. Physically, one expects to find O VI absorption only in reasonably close velocity alignment with Ly-α absorption. In the case of low-density photoionized gas, the alignment should be extremely close: even for metallicities as high as $\frac{1}{10}Z_{\odot}$ the O VI column density can exceed the H I column by no more than $\sim 60\%$ in photoionization equilibrium. Since the oscillator strength for Ly-α is 3.2 times larger than that of O VI, photoionized O VI should always be accompanied by Ly-α in exact velocity alignment at similar or greater optical depth. Collisional ionization equilibrium calculations indicate that it is possible for very hot gas to produce absorption in O VI without strong Ly-α . However, such systems are unlikely to be found in isolation, as some heating mechanism is required to produce and sustain the high temperatures necessary for O VI production. The most likely sources are supernova-driven galactic outflows (Lehnert & Heckman, 1996), shock-heated gas falling onto large-scale filaments (Cen & Ostriker, 1999; Davé et al., 2001; Fang & Bryan, 2001), or hot gas associated with galaxy groups or proto-clusters (Mulchaey et al., 1996). All of these processes should occur near regions of high overdensity—the star-forming galaxy in the case of outflows, and filaments of $\rho/\bar{\rho} = 10 - 100$ in the large-scale structure scenario. Furthermore, both the outflow and the infall processes are characterized by velocities of $\sim 100 - 500$ km/s. In such systems, one would expect to see a broad O VI component separated by $\Delta v < 500$ km/s from a strong Ly-α system that also shows C IV and possibly other heavy element species. We therefore add another criterion to the selection process for O VI involving proximity to Ly-α and C IV absorption for the two likely physical scenarios discussed above. In the photoionized case, we expect to find Ly-α of similar or greater strength than O VI in extremely close velocity alignment, and in the collisionally ionized case we expect to see Ly-α and C IV within 500 km/s of any isolated O VI absorption. We have enforced these criteria by considering only those systems which are either 1) paired with saturated Ly-α at $\Delta v_{\mathrm{H\ I-O\ VI}} < 50$ km/s, or 2) located within 1000 km/s of a system showing C IV absorption.

Application of these two criteria to the "reversed doublet" pairs resulted in the elimination of four of the 7 false systems. These four all showed $\Delta v_{\mathrm{C\ IV-O\ VI}} > 1600$ km/s with no nearbly Ly-α .

Of the remaining three false systems, one has $\Delta v_{\rm H\ I-O\ VI} < 50$ km/s but no corresponding C IV , and two have $\Delta v_{\rm C\ IV-O\ VI} = 200$ and 675 km/s. In contrast, for the sample of 24 real potential O VI systems, 16 are located at $\Delta v_{\rm C\ IV-O\ VI} < 1000$ km/s, and 14 of these show $\Delta v_{\rm C\ IV-O\ VI} < 100$ km/s *and* $\Delta v_{\rm H\ I-O\ VI} < 100$ km/s. Six potential O VI systems were eliminated because of failure to meet the criteria outlined above. This number is encouraging, as it closely matches the number of false systems (7) detected in the reversed doublet search.

We conclude that the selection of O VI candidate systems based on doublet spacing and ratio, subject to constraints on nearby Ly-α and C IV , is effective at reducing the amount of contamination from the Ly-α forest to ~ 2 objects in a sample of 20, or $\sim 10\%$. For the 14 systems with $\Delta v_{\rm C\ IV-O\ VI} < 100$ km/s, the identification as O VI should be the most secure, while the contamination may be somewhat worse for the systems showing $100 < \Delta v_{\rm C\ IV-O\ VI} < 1000$ km/s. Nevertheless, we include these systems in the analysis because of their potential physical importance. Table 2.2 presents a list of the 18 candidate systems which survived the selection process, along with a summary of basic properties derived from the Voigt profile fitting procedure. The table is organized by system, with columns indicating 1) the system redshift, 2) the number of individual O VI components in the system, 3) the total O VI column density, 4) the number of corresponding H I components with $N_{\rm H\ I} > 10^{14.0}$, 5) the column density of the strongest single H I component, 6) the velocity separation between the system and the emission redshift of the background quasar, 7) the velocity separation between the strongest components of O VI and C IV , and 8) The figure number corresponding to the velocity plot for each system. When measuring O VI column densities, we found that the errors on individual components were often somewhat large; this was caused by blending between the components, which opens up a large region of χ^2 space where adequate fits can be obtained by trading column density between different lines in the blend. In these cases the total column density is much better constrained than would be inferred from the sum of the errors for individual components. It is this better constrained value that is quoted in Table 2.2, with accompanying 1σ errors. Figures 2.1 to 2.18 present stacked velocity plots of each system in several ions of interest, overlayed with the best-fit component model.

2.2.4 General Characteristics of Detected O VI Systems

The properties of our 18 O VI systems are not entirely uniform, and while an interpretation of their physical conditions is not possible without reference to ionization models, there are two classes which can be distingiushed by inspection. The first such group contains systems that are ejected from the background quasar. We find two examples in the data (noted in Table 2.2), and they are characterized by broad absorption that is clearly matched in the O VI 1032Å and 1037Å profiles, but for which the optical depth ratio between the doublet components is too small. This phenomenon has been observed in other high redshift QSOs (Barlow & Sargent, 1997), and is thought to result

Table 2.2. Summary of Observed Properties for Strong O VI Systems

Sightline	z_{abs}	$N_{comp,O\ VI}$	$\log(N_{O\ VI,tot})$	$N_{H\ I>14.0}$	$\log(N_{H\ I,max})$	Δv_{QSO}	$\Delta v_{O\ VI-C\ IV}$	Fig.
Q1009+2956	2.253	4	14.626± 0.014	2	17.806	$> 10,000$	91.1	2.1
	2.429	2	13.602± 0.030	3	17.687	$> 10,000$	14.3	2.2
	2.606[1]	1	12.709± 0.083	1	14.442	1,162	··· [4]	2.3
Q1442+2931	2.439	11	15.001± 0.014	3	~ 19.500	$> 10,000$	≈ 0	2.4
	2.623[1]	2	13.592± 0.034	6	15.758	3,300	14.2	2.5
Q1549+1919	2.320	8	14.506± 0.140	3	15.195	$> 10,000$	9.6	2.6
	2.376	2	13.924± 0.021	5	15.545	$> 10,000$	772	2.7
	2.560	1	13.564± 0.096	2	15.219	$> 10,000$	336	2.8
	2.636	2	13.250± 0.021	1	15.220	$> 10,000$	5.4	2.9
	2.711[2]	···	···	···	···	9,460	~ 0	2.10
Q1626+6433	2.245	2	14.827± 0.032	2	15.502	7,317	1.3	2.11
	2.321[1]	1	14.256± 0.024	4	15.423	-300	37.8	2.12
Q1700+6416	2.316	≥ 4	14.968± 0.026	2	17.623	$> 10,000$	13.7	2.13
	2.379	1	13.542± 0.028	2	15.405	$> 10,000$	6.8	2.14
	2.436	9	14.426± 0.081	7	16.943	$> 10,000$	≈ 10	2.15
	2.568	2	13.587± 0.039	1	14.552	$> 10,000$	7.5	2.16
	2.716[2]	4	···	···	···	2250	3.0	2.17
	2.744[1]	3	13.782± 0.058	0	13.840	1500	··· [4]	2.18

[1]Excluded from cosmological statistics because of proximity to background quasar.

[2]Ejected system.

[4]No C IV detected

from partial coverage of the continuum source by small, dense clouds close to the central engine of the QSO. These clouds give rise to saturated absorption over the covered fraction of the central engine, so the doublet ratio approaces unity for these patches. In the uncovered region, unattenuated continuum radiation is able to escape, raising the zero level of the flux to create the appearance of a pair of unsaturated lines with equal strength.

Another group of absorbers which we distinguish from the general population contains systems that are found in the immediate vicinity of the background quasar ($\Delta v < 5000$ km/s). The ionization environment of these systems should differ significantly from the general IGM because of the locally enhanced UV radiation field (Weymann et al., 1981). Also, since QSOs are likely to be found in regions of high overdensity the inclusion of this class could skew statistical results because of clustering effects. Four systems (also noted in Table 2.2) fall into this class, which we hereafter refer to as the "proximity" systems.

After separating out the two populations which are local to the quasar environment, we are left with a total of 12 true cosmological O VI systems, which we call the "intergalactic" sample and which will form the principal focus of this paper. In 10 of these 12 systems, we have detected other highly ionized metals within $\Delta v < 100$ km/s of O VI, including at least C IV , but usually also Si III , Si IV and also other lower ionization species. These 10 also show strong, saturated Ly-α absorption with $\log N_{H\ I} > 14.55$, (for 9 of the 10, $\log N_{H\ I} > 15.2$). The identification of these systems as O VI appears to be very secure.

For the remaining 2 intergalactic systems, the O VI absorption is significantly offset from the nearest large concentration of C IV (by 336 km/s and 772 km/s). These systems are much more difficult to distinguish from chance Ly-α associations, as there is no closely aligned absorption from any ion other than O VI—including Ly-α and N V . Based on our detection of two reversed doublet systems for which $\Delta v < 700$ km/s, these pairs might seem to be likely candidates for contamination. However, the two offset systems differ from the false pairs in that their nearest respective Ly-α systems are exceptionally rich. One shows a cluster of 5 lines with $\log N_{\rm H\ I} > 15.5$ within a 700 km/s range, and other has an H I column density of $\log N_{\rm H\ I} = 16.0$. The Ly-α lines are accompanied by extensive metal line absorption including C IV , Si IV , and Si III . No reversed doublet systems were observed in the vicinity of such strong Ly-α and C IV , and even the two reversed doublet systems showing $\Delta v_{\rm C\ IV-O\ VI} < 1000$ km/s did not have associated Si IV or Si III . The proximity of the offset O VI candidates to several of the strongest absorption line systems in our survey, along with the fact that the offset velocities are exactly those expected in the infall/outflow scenarios discussed above, have led us to consider these systems as highly probable identifications despite the increased possibility of contamination.

Inspecting the final sample of 12 intergalactic systems in Table 2.2 and Figures 2.1-2.18, we see that these selection criteria uncover primarily strong absorbers, with saturated Ly-α and associated heavy element ions. All of our intergalactic systems show $\log(N_{\rm H\ I}) \geq 14.5$ and C IV absorption—i.e. we have not detected any "O VI only" absorbers in the forest (although we do see two such cases in the proximity sample). In fact, our selection has not produced a single convincing example of an O VI doublet aligned with a Ly-α forest line in the column density range $13.5 < \log N_{\rm H\ I} < 14.5$. Such weak O VI lines could escape selection in regions with lower signal-to-noise ratios, and heavier Ly-α forest blending—particularly since we did not remove blended H I lines from O VI profiles until after the O VI was already identified. Thus it is possible that our selection is biased against the weakest O VI lines, since these are most easily lost in blends. For lines with $N_{\rm O\ VI}$ and $b_{\rm O\ VI}$ similar to the systems in Table 2.2, our survey is $\approx 40\%$ complete (see Section 2.3.1.4 for a detailed discussion of the completeness estimation). The completeness is probably lower for the weakest systems; we have accepted this tradeoff to minimize the number of false positive detections in our sample.

Nevertheless, there are several systems that show no O VI absorption despite having high signal-to-noise ratios and being free of Ly-α blends. In these systems we should see O VI even if the metallicity is an order of magnitude below [O/H]=-2.5, assuming a Haardt and Madau (1996) shaped UV background. It is not clear whether these systems are consistent with simple scatter in the cosmic metallicity and/or ionizing radiation field, or whether they represent a distinct population of metal-poor absorbers. We address this more complex issue in a companion paper (Reprinted in Chapter 3). [2] For the remainder of this chapter, we limit our discussion to the strong systems listed in Table

[2] Also, since publication of this paper several other authors have reported on O VI observations in the same redshift

2.2.

2.2.5 Observed Properties of Individual Systems

In this section we present brief summaries of the notable spectral features in each O VI system. We describe only their observed properties; the absorbers' physical conditions are discussed in Section 2.3. The velocity plots in Figures 2.1-2.18 show both the observed data (as a thick histogram) and the best-fit Voigt profile model (as a thin, smooth curve). The quoted temperatures are calculated from line widths, according to the formula $T \leq A(b/0.129)^2$, where b is the line's doppler parameter and A is the ion's atomic mass number. When only a single ion is used to measure the temperature, an upper limit is obtained because the relative contributions from thermal broadening and bulk gas flows are not known. When two ions of different mass are measured for the same absorption component, it is possible to solve for the thermal and bulk broadening separately, yielding a direct temperature measurement.

range, in some cases finding evidence for more weak systems. We compare our results with these studies in Appendix A.

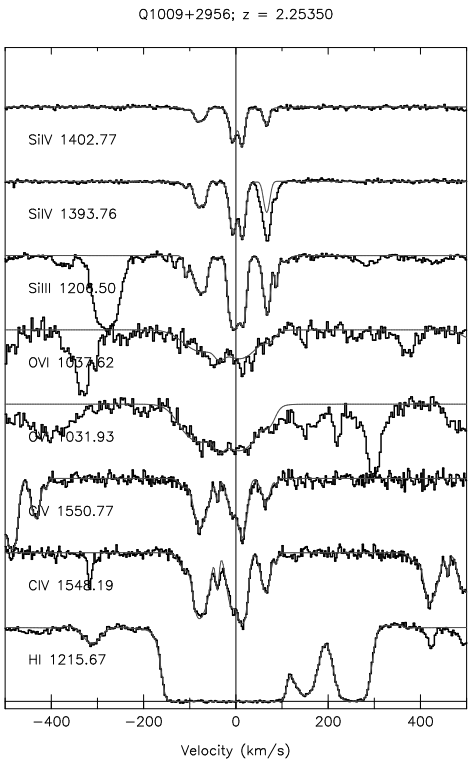

Figure 2.1 Stacked velocity plot of the $z = 2.253$ system in Q1009+2956 (Described in Section 2.2.5.1 of the text). The thin solid line in this figure and all following velocity plots shows the best-fit model obtained from the VPFIT profile fitting software.

2.2.5.1 Q1009+2956: $z = 2.253$ (Figure 2.1)

Our first O VI candidate is located in the vicinity of a strong Lyman limit system (LLS, $\log N_{\rm H\ I} = 17.8$). Both Ly-α and Ly-β were used to fit for the H I column density; higher order Lyman transitions could not be used due to the presence of another Lyman Limit system at higher redshift. Complex chemical absorption containing C IV , Si IV , and Si III and spanning roughly 200 km/s is associated with the strongest H I absorption. The velocity structure in these ions is closely aligned, although the C IV /Si IV ratio varies across the profile, suggesting a spatial variation in ionization conditions. Our Voigt profile fits indicate that the alignment and relative widths of C IV and Si IV are consistent with pure thermal broadening of the profile at $T_{C,Si} = 0.8 - 1.2 \times 10^5$ K (reflecting the range for different individual components).

The O VI profile differs markedly from those of Si IV and C IV , and is characterized by a broad trough with little substructure. This smooth, blended nature causes the Voigt fit parameters to be poorly constrained—particularly the line widths. However, it is still evident from inspection of the profiles that the structure of the O VI line does not mirror that of C IV and Si IV . Taking the best-fit Voigt parameters at face value, the measured limits on the O VI temperature range from $T_{\rm O\ VI} \leq 0.2 - 2.1 \times 10^6$ K for various components, roughly an order of magnitude above the measured

temperatures for C IV and Si IV .

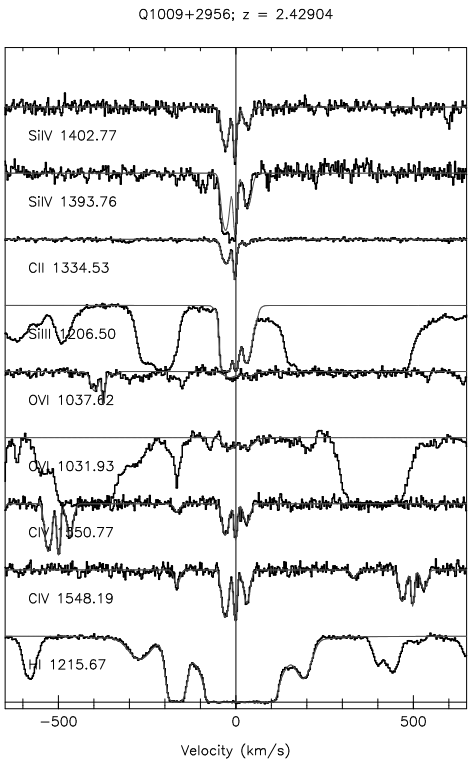

Figure 2.2 Stacked velocity plot of the $z = 2.429$ system in Q1009+2956 (Described in Section 2.2.5.2 of the text).

2.2.5.2 Q1009+2956: $z = 2.429$ (Figure 2.2)

This system is dominated by a single strong H I component, whose column density was measured at $\log(N_{\rm H\ I}) = 17.687$ using Ly-α ,β, γ and δ. As expected for such a strong H I system, significant absorption is present in lower ionization species including C II , Si II , and Al II . The C IV , Si IV , and Si III profiles are closely aligned, and contain at least one very narrow ($b_{\rm C\ IV} = 4.8$ km/s) component that aligns with C II and implies a temperature of $T < 14,000$ K. Similar linewidths for the Si IV and C IV profiles indicate that their broadening may be largely non-thermal, and the temperatures even lower.

The O VI profile contains two subcomponents, neither of which aligns in velocity with the lower ionization lines. Their line widths of $b_{\rm O\ VI} = 22.2, 24.7$ km/s imply upper limits of $T_{\rm O\ VI} < 5 \times 10^5$ K.

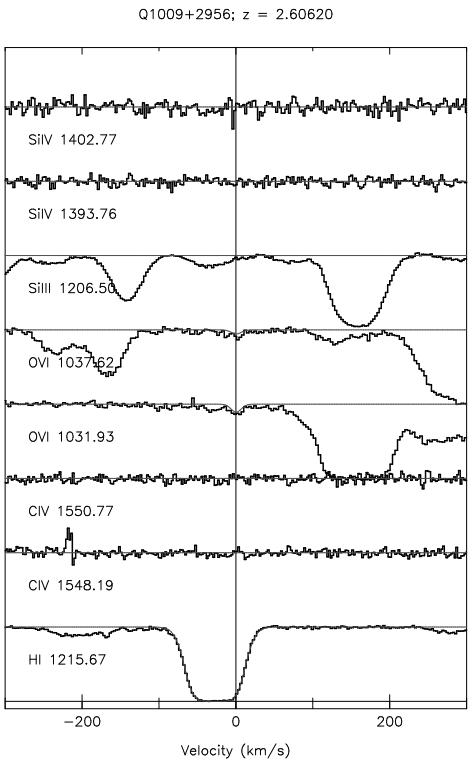

Figure 2.3 Stacked velocity plot of the $z = 2.606$ system in Q1009+2956 (Described in Section 2.2.5.3 of the text). This system has been excluded from the cosmological statistics due to its proximity to the background quasar.

2.2.5.3 Q1009+2956: $z = 2.606$ (Figure 2.3)

This system consists of a single, isolated Ly-α line with associated O VI, but no absorption from any other heavy elements. The H I resembles a typical Ly-α forest line, at $\log(N_{\rm H\ I}) = 14.442$ and $b_{\rm O\ VI} = 25.6$ km/s. A single O VI line is detected at the $\geq 3\sigma$ level, and is measured to have $\log(N_{\rm O\ VI}) = 12.709$ and $b_{\rm O\ VI} = 8.0$ km/s ($T_{\rm O\ VI} \leq 6.2 \times 10^4$ K). This is an example of the type of system we had expected to detect in large numbers in our survey. However, this particular absorber is located only 3050 km/s from the background quasar and its ionization state is likely to be affected by UV radiation from the QSO. It has therefore been grouped with the "proximity" sample and not included in our discussion of cosmological O VI absorbers. However, its detection illustrates that the survey is sufficiently sensitive to uncover "O VI only" systems, even though we have found none in the more tenuous regions of the IGM.

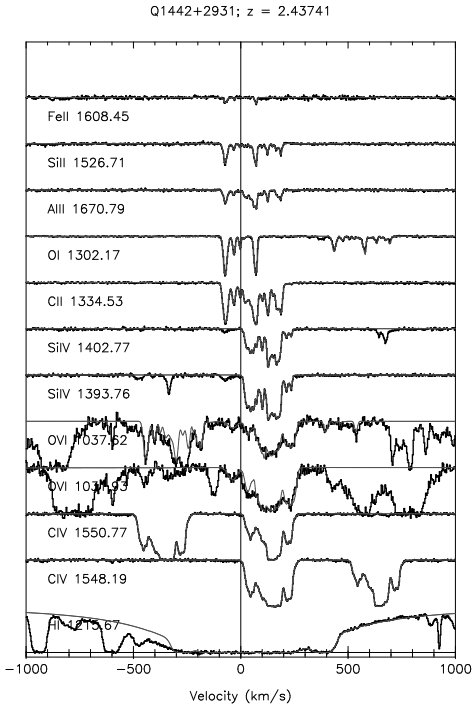

Figure 2.4 Stacked velocity plot of the $z = 2.439$ system in Q1442+2931, which is a weak DLA and the strongest system in the survey (Described in Section 2.2.5.4 of the text). The additional absorption shown in the O VI 1037Å fit is due to the 1036Å transition of C II . Likewise, the absorption at +500 km/s in the O I profile is caused by Si II 1304Å.

2.2.5.4 Q1442+2931: $z = 2.438$ (Figure 2.4)

This O VI absorption is associated with a weak damped Ly-α (DLA) system. The damping wings of the profile spread over several echelle orders, complicating attempts to determine the exact H I column density. However, based on the presence of the modest damping wings, and a relatively weak saturation level in the core by DLA standards, we estimate that $\log N_{\rm H\ I} \sim 19.0 - 20.0$. A rich metal line structure is detected both in low ionization (O I , Si II , Fe II , Al II , C II) and high ionization (C IV , Si IV) species. The kinematic spread of the lowest ionization gas (e.g., Fe II , O I) spans a range of ~ 200 km/s and is centered near the strongest H I absorption. The highest ionization gas (C IV, Si IV, O VI) also spans a $\sim 200 - 250$ km/s velocity interval, but is offset ~ 200 km/s to the red of the low ionization species. Several intermediate ionization lines (Si II , C II , Al III) bridge the velocity range between the high and low ionization species, sharing absorption components with both varieties of gas.

The O VI kinematics strongly resemble those of C IV , where a strong absorption trough at $z = 2.390$ is flanked by two weaker structures at ± 100 km/s. A detailed comparison of the central regions of the profiles is not possible because of saturation in the C IV core.

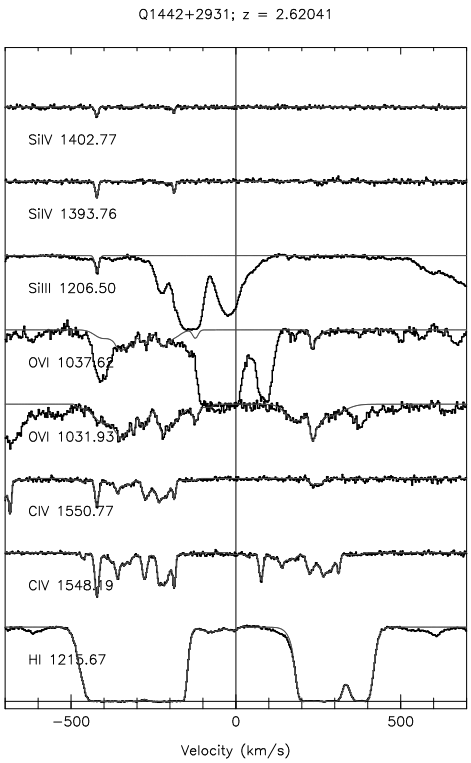

Figure 2.5 Stacked velocity plot of the $z = 2.623$ system in Q1442+2931 (Described in Section 2.2.5.5 of the text). This system has been excluded from the cosmological statistics due to its proximity to the background quasar.

2.2.5.5 Q1442+2931: $z = 2.623$ (Figure 2.5)

This O VI absorption is associated with a pair of strong H I systems, seen at $\sim \pm 300$ km/s in Figure 2.5. The H I at -300 km/s splits into three strong components in higher order Lyman lines, and we measure these to have column densities of $\log(N_{\rm H\ I}) = 15.3, 15.3$, and 14.6. The group at $+300$ km/s is dominated by a single line with $\log(N_{\rm H\ I}) = 15.8$. The whole complex is located near the background quasar at $\Delta v \approx 3100$ km/s, so we have grouped it in the proximity sample and excluded it from our cosmological statistics.

This system was originally identified as an O VI absorber based on the narrow line located near $+250$ km/s in the figure. Though this line is blended with Ly-α absorption from the forest in the 1032 Å component, a sharp core is quite visible in the profile that mirrors the shape of the uncontaminated O VI 1037 A line. The width of this core is relatively small at $b = 7.41$ km/s, and implies an upper limit of $T_{\rm O\ VI} \leq 5.27 \times 10^4$ K. A second, much broader component ($b = 19$ km/s) is also seen in the red wing of this line. C IV is detected in the same velocity range as the sharp O VI component, further securing the O VI identification for the system. The O VI and C IV may come from the same gas, as the redshifts are identical to within the 1σ errors, and the velocity widths are also within 1σ of a simulateneous solution of $T_{\rm C\ IV,O\ VI} = 8.5 \times 10^4$ K. The column density ratio

for these lines is $\log(N_{\rm O\ VI}/N_{\rm C\ IV}) = 0.454$.

The absorption complex at -300 km/s shows a much richer chemical structure, containing kinematically complex C IV , and also weak Si IV and Si III . We did not originally identify O VI associated with this H I using our search strategy, because we could not be certain that much of the absorption in the 1037 Å profile over this range was not Ly-α contamination. However, in light of the nearby sharp O VI line discussed in the preceeding paragraph, the strong H I , C IV , Si IV , and Si III , and the good match of the 1032 Å and 1037 Å profiles, we treat this as a tentative O VI identification. If this absorption actually represents O VI, its properties are different from those of the C IV and Si IV lines. Solving simultaneously for the temperature using the C IV and Si IV linewidths , we find $T_{C,Si} = 1.2 - 2.6 \times 10^4$ K, while attempts to fit the O VI profile yield linewidths in the range $b_{\rm O\ VI} = 10.6 - 32.8$ km/s, or $T_{\rm O\ VI} \leq 1 \times 10^5 - 1 \times 10^6$ K.

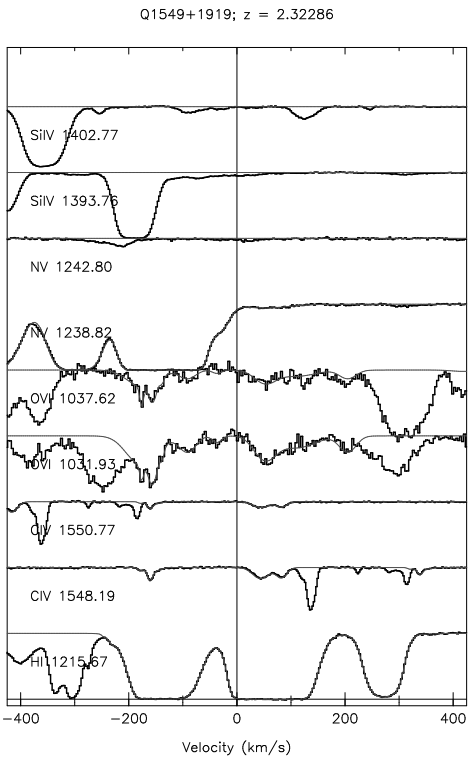

Figure 2.6 Stacked velocity plot of the $z = 2.321$ system in Q1549+1919 (Described in Section 2.2.5.6 of the text). The O VI 1032Å profile has been adjusted to remove a Ly-β line which was blended over the range 0-200 km/s in the figure.

2.2.5.6 Q1549+1919: $z = 2.320$ (Figure 2.6)

This example contains a broad complex of O VI distributed over $\Delta v \sim 500$ km/s. The associated H I is once again not dominated by a single line, but rather by a cluster of three moderately strong lines ($\log N_{\rm H\ I} = 15.195, 14.627, 14.111$) within a small velocity interval. The O VI in this system was originally identified by the presence of two narrow lines seen at the blue end of the profile. We detect a single weak C IV line associated with this narrow O VI component. Although the C IV and O VI do not align exactly in velocity, their doppler widths both indicate upper limits on the temperature which are quite cool, in the range $T \leq 3.2 - 7.4 \times 10^4$ K. One of the O VI lines is extremely narrow at 1.46 km/s ($T_{\rm O\ VI} \leq 2000$ K), although this may be a noise artifact.

A second pair of C IV lines is detected near the strongest Ly-α line in the system. This additional C IV is unusually broad and featureless—the velocity width of one of the two C IV components is measured at $b = 19.67$ km/s, or $T_{\rm C\ IV} \leq 2.8 \times 10^5$ K. Such an environment should be conducive to the production of other very highly ionized species, including O VI. However, we did not at first identify any O VI associated with the broad C IV because the O VI 1032 Å line was blended with a higher redshift Ly-β line. The contamination was removed by fitting the corresponding Ly-α profile to infer the Ly-β line strength, revealing the profile shown in the figure.

The shape of the deblended profile suggests that O VI exists over the entire range of H I absorption. Most of this O VI is lacking in detailed substructure. Our Voigt profile fits help to characterize several of the apparently broad features, although the errors on the fit parameters are significant because of the smoothness of the profile. The strongest distinct feature is a broad line near the strongest H I component and wide C IV (+50 km/s in Figure 2.6). Its measured $b_{\mathrm{O\ VI}} = 26.43$ implies an upper limit on the temperature of $T \leq 6.7 \times 10^5$ K. This matches the high temperature inferred from C IV to within 1σ errors, although the different shapes of the O VI and C IV profiles indicate that the absorption probably does not arise in the same gas.

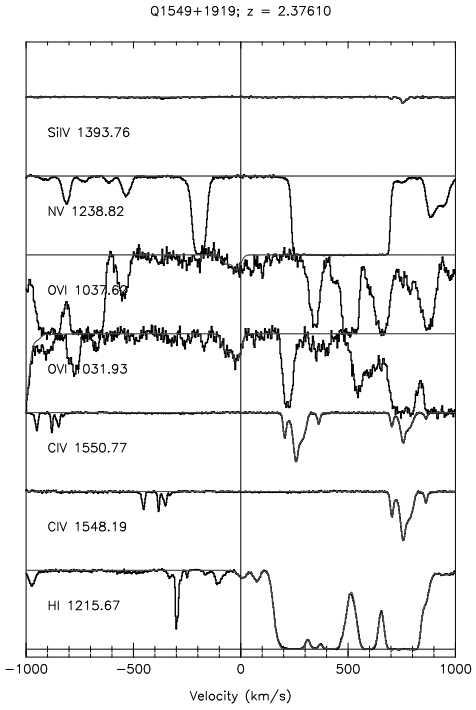

Figure 2.7 Stacked velocity plot of the $z = 2.375$ system in Q1549+1919 (Described in Section 2.2.5.7 of the text).

2.2.5.7 Q1549+1919: $z = 2.376$ (Figure 2.7)

This system is offset by more than 700 km/s from the nearest C IV line. No absorption is seen from any ion including H I at the O VI redshift, so the identification rests on the similarity of the doublet profiles alone. These are identical to within the noise over most of their length, though some blending is present in the 1037Å component.

The nearest H I to this system is an unusual complex, containing five lines of $\log(N_{\rm H\ I}) > 14.0$ within a span of 600 km/s. No single line dominates the complex; the strongest (located at +750 km/s from the O VI) is measured at $\log(N_{\rm H\ I}) = 15.6$. C IV , Si III , and Si IV are clearly detected in association with the strongest H I component, but the O VI profile suffers from heavy Ly-α forest blending in this region. Using profile fits of the C and Si ions to solve simulatneously for the gas temperature and non-thermal motions, we estimate $T_{C-Si} = 2.2 \times 10^4$ K.

Our best fit Voigt profile for the O VI (based primarily on the unblended 1032 Å component) requires two lines, with widths of $b = 25.24, 26.70$ km/s. The implied upper limits on the O VI temperature are $T_{\rm O\ VI} \leq 6.5 \times 10^5$ K—over an order of magnitude higher than that of C or Si, although the O VI measurement is only an upper limit. High quality data in the C IV and N V regions ($\frac{S}{N}$(C IV) $\approx 150, \frac{S}{N}$(N V) ≈ 120 per pixel) allow to set extremely strong limits on the non-detection of other ions associated with O VI: in particular $\log(N_{\rm O\ VI}/N_{\rm N\ V}) > 2.398$ and $\log(N_{\rm O\ VI}/N_{\rm C\ IV}) > 2.717$.

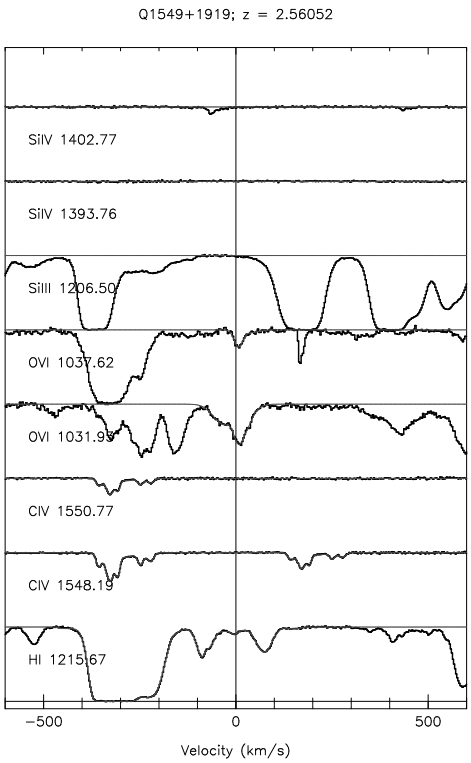

Figure 2.8 Stacked velocity plot of the $z = 2.561$ system in Q1549+1919 (Described in Section 2.2.5.8 of the text).

2.2.5.8 Q1549+1919: $z = 2.560$ (Figure 2.8)

This system contains a single O VI line with no associated H I absorption, although a strong H I absorber of $\log(N_{\rm H\ I}) = 15.219$ is located 336 km/s to the blue. The O VI 1032 Å line is blended with interloping H I , but a distinct narrow component is still visible in this blend, matching in redshift and doppler parameter with the clean O VI 1037 Å profile. The measured $b_{\rm O\ VI} = 14.6$ km/s translates to an upper limit of $T_{\rm O\ VI} \leq 2.0 \times 10^5$ K.

As in the preceding example, no absorption is seen from any other heavy elements at the redshift of the O VI line: we measure limits of $\log(N({\rm O\ VI})/N({\rm C\ IV})) \geq 2.701$ and $\log(N({\rm O\ VI})/N({\rm N\ V})) \geq 2.038$. However, significant C IV is associated with the Ly-α complex at -336 km/s. In this region, the detailed structure of the O VI 1032 Å profile seems to mirror that of the C IV , suggesting that there may be further O VI locked up in this system. Indeed, the observed O VI substructure is almost certainly not the product of chance Ly-α forest absorption, as it varies on velocity scales of ~ 10 km/s, whereas characteristic velocity widths in the Ly-α forest are $b > 20$ km/s. Nevertheless, we do not claim a direct detection of O VI in this part of the profile, as the O VI 1037Å line is saturated by a blended Ly-α forest line, and the 1032Å component appears to suffer from blending as well.

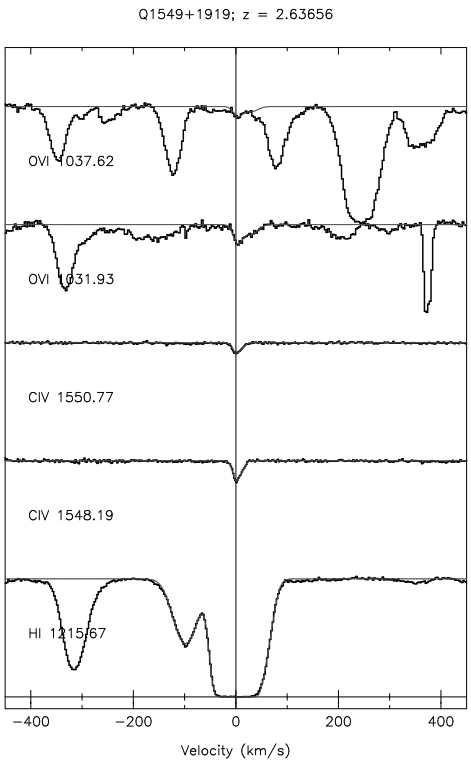

Figure 2.9 Stacked velocity plot of the $z = 2.636$ system in Q1549+1919 (Described in Section 2.2.5.9 of the text).

2.2.5.9 Q1549+1919: $z = 2.636$ (Figure 2.9)

This system has a particularly simple chemical and velocity structure. The Ly-α profile is dominated by a single H I line with $\log(N_{\rm H\ I}) = 15.220$, which places it among the weakest systems in the survey. Several other systems contain groups of lines with similar H I column densities, but this system is unusual in its isolation from other strong H I .

Heavy element absorption is only seen in C IV and O VI, both of which are adequately fit by a pair of Voigt profile components. The velocity alignment between the ions is relatively close, but for both components the O VI linewidth exceeds that of C IV despite the fact that O VI is a heavier ion than C IV . The C IV linewidth constrains its temperature to be below $T_{\rm C\ IV} < 5.0 \times 10^4$ K, while the O VI linewidth permits temperatures in the range $T_{\rm O\ VI} < 1.3, 2.6 \times 10^5$ K for the two components.

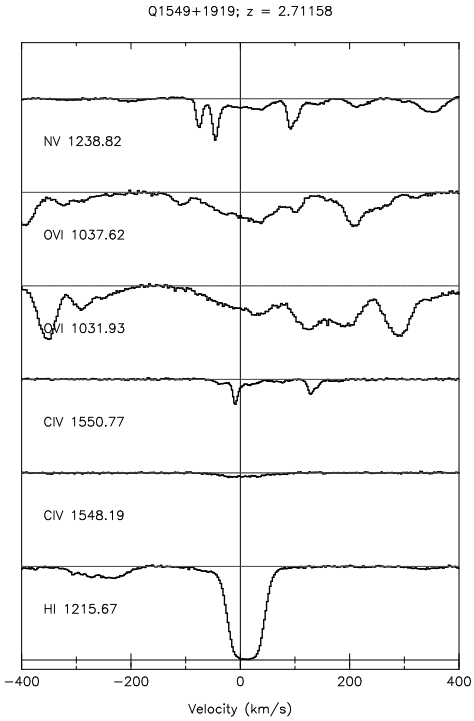

Figure 2.10 Stacked velocity plot of the $z = 2.711$ system in Q1549+1919 (Described in Section 2.2.5.10 of the text). Because the O VI doublet ratio is unity over the whole profile, we classify this as an ejected system which is partially covering the continuum source.

2.2.5.10 Q1549+1919: $z = 2.711$ (Figure 2.10)

This absorber is an example of highly ionized ejecta from the background QSO, moving at $v_{ej} \approx 10,000$ km/s. A wide, sloping absorption profile is seen in O VI, C IV , and N V (only N V 1238 Å is shown, as the 1242 Å line is contaminated by Ly-α forest absorption). The H I seen at the same redshift is not likely to be associated with the ejecta, as it shows no sign of the unusual kinematics that characterize the high ionization lines. The principal evidence for the ejection hypothesis comes from the doublet ratios of O VI, C IV, and N V, which are unity over their whole profiles rather than the value deduced from the oscillator strengths of different transitions (see Section 2.4 for a more thorough discussion of this phenomenon). Accordingly, we have excluded this system from our further statistical analysis.

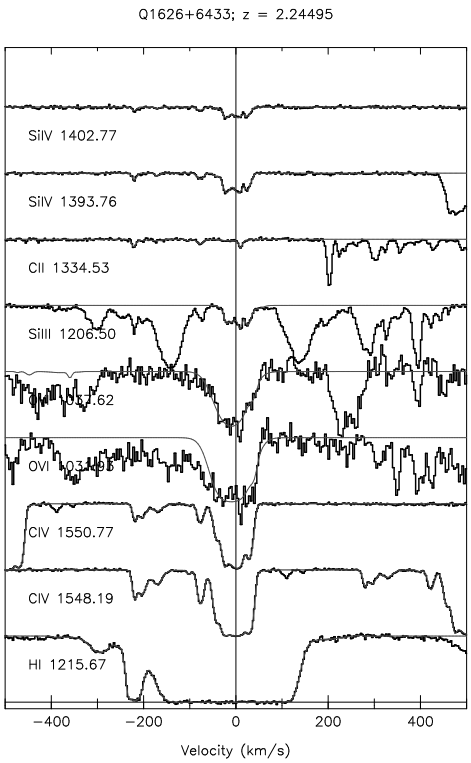

Figure 2.11 Stacked velocity plot of the $z = 2.245$ system in Q1626+6433 (Described in Section 2.2.5.11 of the text).

2.2.5.11 Q1626+6433: $z = 2.245$ (Figure 2.11)

This O VI system—our lowest redshift example—is somewhat difficult to interpret due blending and saturation in the O VI 1032 Å component, and a relatively low signal-to-noise ratio (~ 7). It is associated with a multicomponent H I complex of total column density $\log(N_{\rm H\ I}) = 15.544$ seen as a single line in Ly-α , although a fit to Ly-β reveals several subcomponents. The strongest of these is saturated in both Ly-α and Ly-β , but higher order transitions could not be used in the fit because of their poor signal-to-noise ratios.

Heavy element absorption is seen in C II , C IV , Si IV , and Si III . In each case, the metals are in two clusters—one associated with the densest H I , and a second, weaker group near a smaller H I line at -200 km/s. The O VI absorption is only found near the stronger line, though a weak signal at -200 km/s could be masked by noise. Since the strong C IV profile is saturated in the 1548Å component, we have used only the unsaturated 1551Å component to measure the velocity profile. The individual elements of the C IV , Si III , and Si IV absorption align well in velocity, and the fits indicate a temperature range of $T = 2 - 8 \times 10^4$ K for the carbon and silicon gas.

Because of lower data quality, it is difficult to judge whether the velocity structure of O VI matches that of the C IV and Si IV profiles. The overall velocity extent appears to be similar, but any substructure is lost in the noise. We have therefore compared two different approaches to measure

the system's properties. The first of these assumes that the O VI absorption comes from the same gas as C IV , Si III , and Si IV , and is motivated by the similar extent of O VI and C IV in velocity space. To test the plausibility of this hypothesis, we have fit a model O VI profile that contains 8 components with the same redshifts and b parameters (reweighted by $\sqrt{m_{\rm C\ IV}/m_{\rm O\ VI}}$) as the C IV profile. The column densities were then allowed to vary to achieve the best fit. The O VI line strengths measured in this way yield typical ratios of $\log(N_{\rm O\ VI}/N_{\rm C\ IV}) \sim 0.3$ and $\log(N_{\rm O\ VI}/N_{\rm Si\ IV}) = 1.5 - 2.2$ for individual absorption components. We then compared these ratios with the predictions of ionization simulations (described in detail in section 3.1.3) to see if they are consistent with a photoioniation interpretation. From this exercise we found that if the C IV and Si IV are produced in the same gas, then the observed O VI line strength is much stronger then expected. We therefore consider it likely that the O VI gas is physially distinct from the C IV and Si IV gas, which is similar to what is seen in most other systems.

Our second approach assumes that the C and Si absorption are associated, but that the O VI is contained in a separate phase. A Voigt profile fit to the O VI 1037Å profile requires only two components to adequately represent the data ($\chi^2_\nu = 1.02$). The fit does not match the 1032 Å profile exactly, but the discrepancy can be attributed to forest contamination. Most of the O VI absorption is contained in a single component with $\log(N_{\rm O\ VI}) = 14.8$ and $b_{\rm O\ VI} = 38$ km/s ($T_{\rm O\ VI} \leq 1.4 \times 10^6$ K). This total column density is actually quite similar to the total column measured using the first approach, but the upper limit on the temperature is significantly higher. This second hypothesis can be plausibly reconciled with collisoinal ionization predictions, so we consider it to be the more likely of the two scenarios.

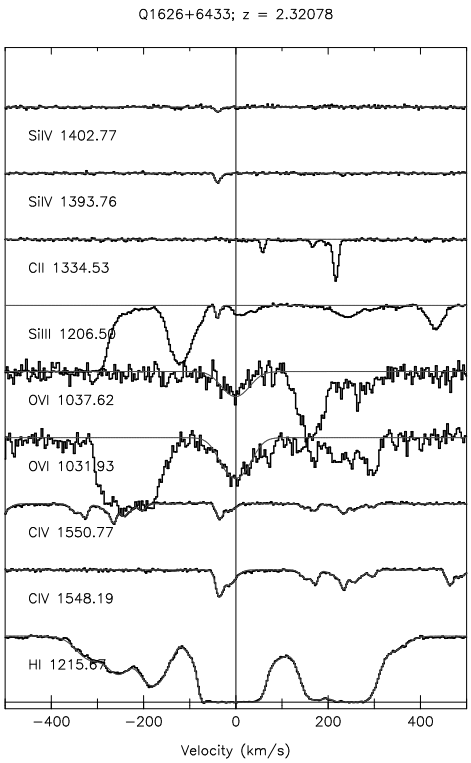

Figure 2.12 Stacked velocity plot of the $z = 2.321$ system in Q1626+6433 (Described in Section 2.2.5.12 of the text). This system is located 200 km/s *redward* of the emission redshift of the QSO (measured from Ly-α). It is therefore excluded from the cosmological statistics, though we believe it is likely caused by the QSO host galaxy itself or a very nearby companion.

2.2.5.12 Q1626+6433: $z = 2.321$ (Figure 2.12)

This unusual system is actually located 300 km/s *redward* of the Ly-α emission line of the QSO, an effect that can be caused by a 300-500 km/s blueshift of of the Ly-α emission line relative to the "true" QSO redshift as measured from narrow forbidden lines (Tytler & Fan, 1992). However, the properties of this system favor its interpretation as an intervening rather than ejected absorption system. Ultimately we do not include it in the cosmological sample because of its proximity to the background quasar.

The H I structure consists of a group of four moderately strong lines ($14.0 < \log N_{\rm H\ I} < 15.5$) within a $\Delta v \sim 500$ km/s velocity interval—similar to what is seen in many of the other O VI absorbers we have detected. C IV , Si III , Si IV , and O VI are all seen in the vicinity of the central, strongest H I line and the velocity structure in all of these ions is identical except for O VI. The velocity profiles of the moderate ionization lines are consistent with their production occurring in a single common gas phase at $T = 2.25 \times 10^4$ K.

The O VI profile is much stronger and broader than those of all the other observed species. A single $b_{\rm O\ VI} = 37$ km/s Voigt profile provides our best fit to the data, and sets an upper bound on

the temperature of $T_{\rm O\ VI} \leq 1.3 \times 10^6$ K—almost two orders of magnitude higher than the lower ionization species.

One could interpret the large velocity width of O VI, and its high ionization state as a sign that the O VI gas is ejected from the QSO rather than intervening. While this possibility cannot be disproven, the 300 km/s redshift of the O VI line relative to Ly-α requires that the ejection velocity $v_{ej} \leq 200$ km/s even after including a +500 km/s correction to the Ly-α redshift. This velocity is very small compared to values of several thousand km/s typical of material ejected from QSOs (Turnshek, 1984). Furthermore, the close alignment of the O VI and other ions ($\Delta v < 40$ km/s), the accuracy of the doublet ratio implying full coverage of the continuum source, and the quiescent kinematics of C IV and other lower ionization species, all point away from the ejection hypothesis for this absorber. We favor the interpretation that the absorption arises in intervening gas, possibly associated with the QSO host galaxy or a nearby companion.

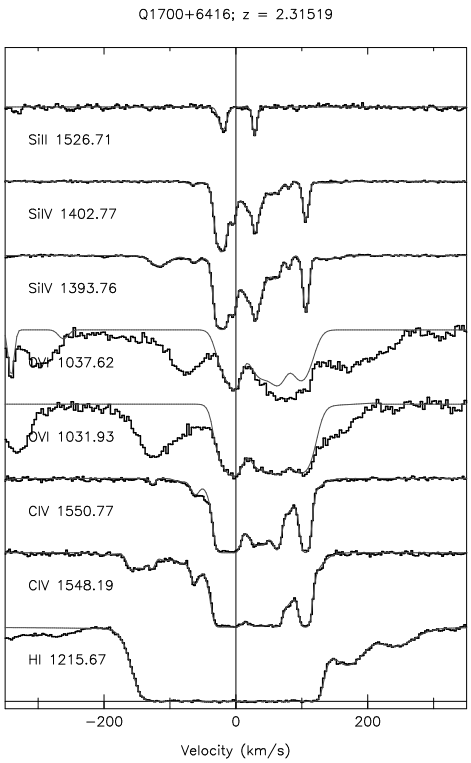

Figure 2.13 Stacked velocity plot of the $z = 2.315$ system in Q1700+6416 (Described in Section 2.2.5.13 of the text).

2.2.5.13 Q1700+6416: $z = 2.316$ (Figure 2.13)

This O VI absorption is associated with a Lyman limit system, of column density $\log(N_{\rm H\ I}) = 17.6$, although only Ly-$\alpha$ and Ly-β could be used in the measurement and both were saturated. Rich heavy element absorption is seen in both high ionization species (C IV, Si IV, and O VI) and low ionization species (C II, Al II, Si II).

The low ionization species all share a similar kinematic structure, concentrated around two lines separated by ~ 45 km/s in the very core of the H I profile. The narrow widths of these lines imply low temperatures in the range $T_{\rm O\ VI} \leq 0.7 - 7 \times 10^4$ K, as would be expected in the central regions of a strong H I system.

The highly ionized species are very strong, and in the case of C IV we observe significant saturation. The velocity structure of the gas can be read from the Si IV line, which appears to match the C IV profile but is probably not related to O VI. The temperature of the C-Si phase derived from the Si IV line widths is quite cool, and resembles that of the low ionization gas at $T \leq 2 - 3 \times 10^4$ K. However, C IV and Si IV are much more widespread, spanning ~ 150 km/s. The O VI profile is significantly contaminated by Ly-α forest absorption, particularly in the 1037 Å component. At least one line, located at -20 km/s in Figure 2.13, is clearly distinguished and may be associated with the strongest C IV and Si IV lines even though the redshifts do not align exactly. Our best-fit

Voigt profile for this line contains two components, with b parameters of 14.35 and 11.53 km/s ($T_{\rm O\ VI} = 1.27 - 1.97 \times 10^5$ K) and column densities of $\log(N_{\rm O\ VI}) = 14.0, 14.2$. The column densities derived from fitting the rest of the profile are all similar, though the linewidths are larger ($b = 15 - 25$ km/s). While this may be an indication of higher temperature gas, the model for this part of the O VI profile is highly uncertain because of the strong forest contamination.

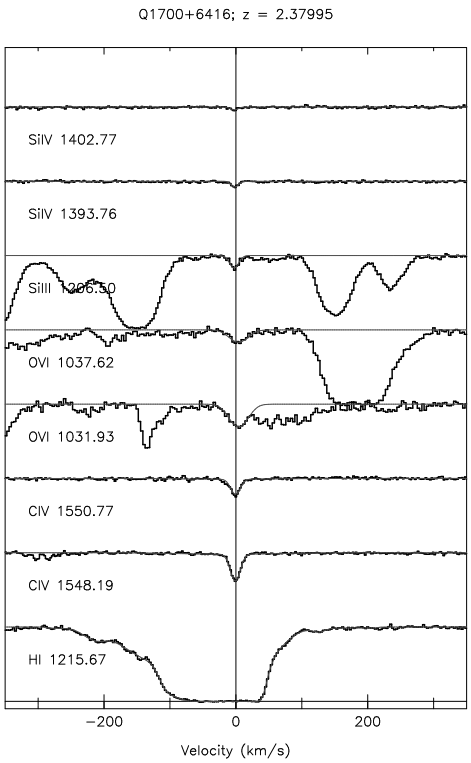

Figure 2.14 Stacked velocity plot of the $z = 2.379$ in Q1700+6416 (Described in Section 2.2.5.14 of the text).

2.2.5.14 Q1700+6416: $z = 2.379$ (Figure 2.14)

This is the most kinematically simple O VI system we have detected in our survey; each of the observed metal lines contains only a single absorption component. The H I line is at the strong end of the Ly-α forest regime, with two dominant components at $\log(N_{\rm H\ I}) = 14.8, 15.4$. Besides O VI, we detect most of the common high ionization species, including C IV , Si III , and Si IV , however no N V is detected. We also do not see any low ionization lines.

Our fits to the Si and C lines may be accurately explained with a single gas phase, with $T_{C,Si} = 3 \times 10^4$ K, characteristic of low density gas in the Ly-α forest. The O VI line differs from these other species slightly in both redshift, which is offset by 10 km/s (a 6σ difference), and doppler width, measured at 19 km/s. This width admits the possibility of a high termperature gas, i.e. $T_{\rm O\ VI} \leq 3.4 \times 10^5$ K. Although one might expect some uncertainty in the line widths because of blending in the O VI 1032 line, we have used only the 1037 A component of the doublet in our fit, and found that it matches the 1032 Å profile extremely well (in fact, the blending is caused by Ly-δ absorption from a system at higher redshift; the correspondence is even better when this is fit out of the profile). The measured column densiy ratios for O VI, and Si IV are $\log(N_{\rm O\ VI}/N_{\rm C\ IV}) = 0.323$, and $\log(N_{\rm O\ VI}/N_{\rm Si\ IV}) = 1.570$. We will discuss in Section 2.3.1.3 why these ratios do not agree with the predictions of simple single phase photoionization models for C IV and Si IV . The O VI is

probably physically distinct from these other species.

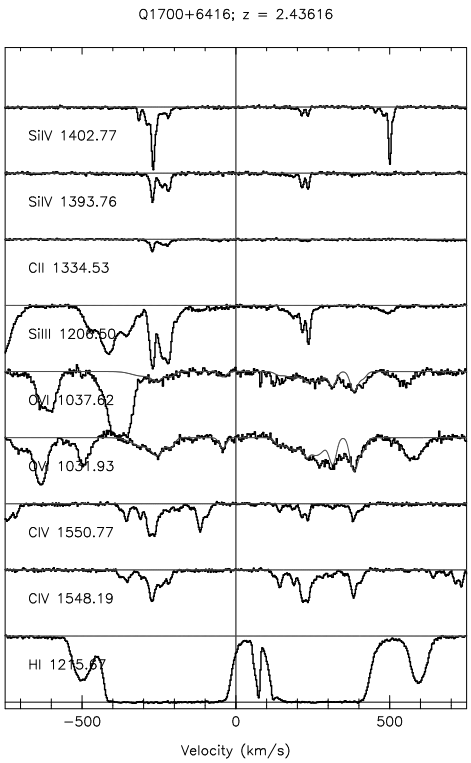

Figure 2.15 Stacked velocity plot of the $z = 2.433/2.439$ system in Q1700+6416 (Described in Section 2.2.5.15 of the text). The O VI 1032Å profile has been adjusted to remove an interloping Ly-β line at $z = 2.463$ (+300 km/s), to better illustrate the correspondence of the O VI doublet profiles.

2.2.5.15 Q1700+6416: $z = 2.436$ (Figure 2.15)

This complex system contains a number of lines distributed over ~ 1000 km/s. The lines are grouped into two distinct clusters separated by $\sim 5 - 600$ km/s, and each cluster contains absorption from both low ionization species (e.g., C II) and high ionization species, including C IV , Si III , Si IV , and O VI.

The H I absorption in this system contains 8 lines with $\log(N_{\rm H\,I}) > 14.0$ in a 1000 km/s velocity interval. The H I near the blue line cluster is dominated by a single line with $\log(N_{\rm H\,I}) = 16.943$. The red cluster's H I splits into several components in the higher order Lyman lines, and is dominated by three lines with $\log(N_{\rm H\,I}) = 14.860, 15.706$, and 15.806. The sharp line seen between the two strong H I features is an unrelated Si III 1206 line at $z = 2.463$.

In both of the line clusters, blending from the Ly-α forest complicates the measurement of O VI parameters. This is apparent for the absorption at -300 km/s in Figure 2.15, for which the 1037Å component is blended with a strong H I line. Though not obvious in the Figure, it is also true for the absorption at +300 km/s, which is blended with a $z = 2.46$ Ly-β line. By fitting the corresponding Ly-α line ($\log(N_{\rm H\,I}) = 14.4$), we were able to remove the Ly-β contamination, revealing the profile shown in the figure.

Kinematically complex C IV is seen in the neighborhood of each of the absorption clumps, and Si III and Si IV are also strong, through not as distributed in velocity. Low ionization species (C II and Si II) are seen in the same vicinity as some Si III and Si IV , though only near the strongest of the H I lines in the blue line cluster. The linewidths of the low and moderate ionization gas are consistent with thermal broadening at $T = 4 - 7 \times 10^4$ K.

The kinematics of the O VI gas are more difficult to constrain because of Ly-α forest contamination. For the blue line cluster, we have treated all the absorption in the O VI 1032 Å line as actual O VI. Under this assumption, a three component model is sufficient to describe the data. Two of the components can be matched to the 1037 Å profile in the wing of the blended Ly-α , but the third component is completely blended and therefore more suspect. All three of the lines are broad; the doppler widths for the two secure lines are $b_{\rm O\ VI} = 22.14, 23.48$ km/s, or $T_{\rm O\ VI} \leq 5.3 \times 10^5$ K. In the redder cluster of lines, the velocity widths are difficult to measure because the profile is not easily described by discrete lines. Our best-fit model again shows lines that are broader than those of other ions, near $b_{\rm O\ VI} = 15$ km/s or $T_{\rm O\ VI} \leq 2.2 \times 10^5$ K. One line is much broader yet at 40 km/s.

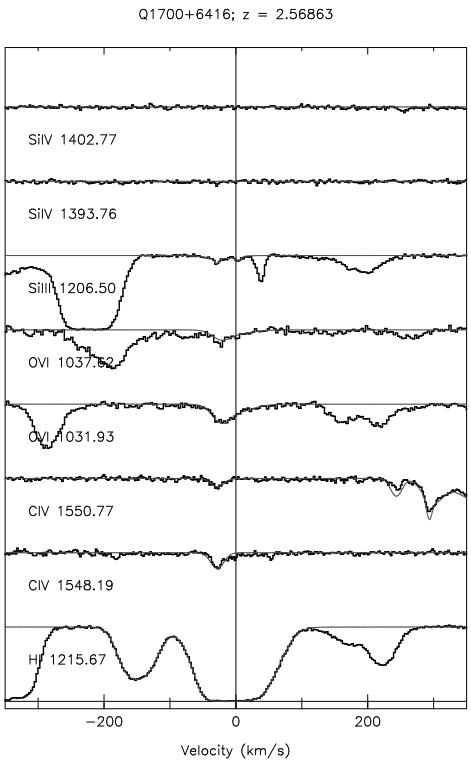

Figure 2.16 Stacked velocity plot of the $z = 2.568$ system in Q1700+6416 (Described in Section 2.2.5.16 of the text).

2.2.5.16 Q1700+6416: $z = 2.568$ (Figure 2.16)

This system has a simple velocity structure, and is centered near a moderate Ly-α absorber ($\log N_{\rm H\ I} = 14.5$). A single, narrow heavy element line with weak flanking absorption is seen in C IV and Si III ; a very weak Si IV feature is also detected, but is not strong enough to provide detailed velocity information. The C IV linewidth is an intermediate $b = 12.9$ km/s ($T \leq 1.2 \times 10^5$), while Si III is very narrow, implying $T \leq 2 \times 10^4$ K.

The shapes of the O VI 1032 and O VI 1037 Å components do not match in detail, probably because of blending in the 1032 Å line. The O VI 1037 line profile does however resemble the shape of C IV , although our best fit shows it to be offset by 10-12 km/s. Our estimate of 17.8 km/s for the O VI linewidth implies a higher temperature for the O VI gas, with an upper limit of $T \leq 3.0 \times 10^5$ K. However, we caution that blending in the O VI core makes it difficult to obtain a reliable measurement of the width. While the coincidence with C IV increases the probability of this system being O VI, we still regard its identification as tentative.

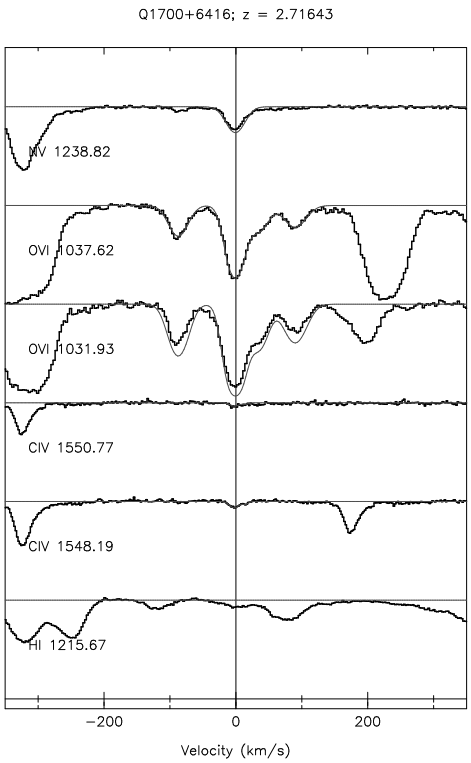

Figure 2.17 Stacked velocity plot of the $z = 2.716$ system in Q1700+6416 (Described in Section 2.2.5.17 of the text). The model fit shown in the figure illustrates the expected strength of the O VI 1032Å line based on a fit to the 1037Å profile. Because the observed profile does not match the expected doublet ratio, we have surmised that this absorber is ejected from the background QSO and only partially covers the central engine. It has been excluded from the cosmological statistics.

2.2.5.17 Q1700+6416: $z = 2.716$ (Figure 2.17)

The system is another example of gas ejected from the background quasar, in this case at 2250 km/s. The system was identified by an unmistakable correspondence between the profiles of the O VI doublet components. Strong absorption is seen in O VI, C IV, and N V, and in each case the ratio of the line strengths for the two components of the doublet is smaller than the expected value, indicating partial coverage of the continuum source. Because this is an ejected rather than intervening source, we have excluded it from further analysis.

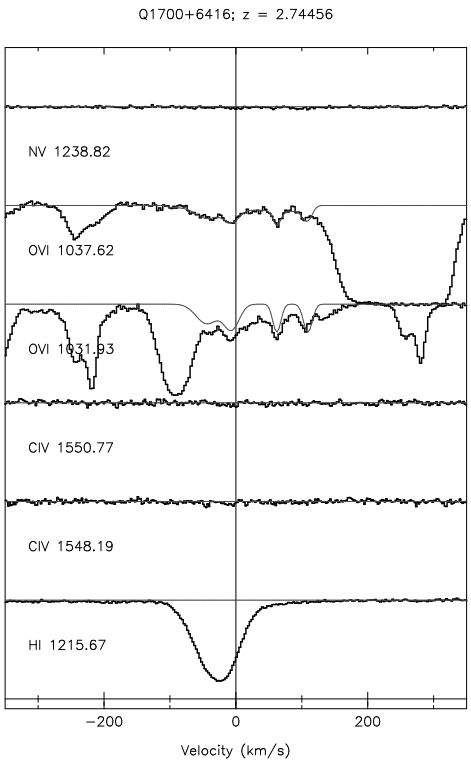

Figure 2.18 Stacked velocity plot of the $z = 2.745$ system in Q1700+6416 (Described in Section 2.2.5.18 of the text). This system has been excluded from the cosmological statistics sue to its proximity to the background QSO.

2.2.5.18 Q1700+6416: $z = 2.744$ (Figure 2.18)

The last system we discuss contains four distinct components, neighboring a single weak H I line. No heavy elements other than O VI are detected. The measured linewidths for the three O VI components range from 7.14 km/s to 15.27 km/s ($T_{\rm O\ VI} \leq 5 \times 10^4 - 2.2 \times 10^5$ K. Since this system is extremely close to the background QSO, we do not include it in our cosmological statistics. The quasar is known to be ejecting O VI (see previous section), so the absorption could be caused by additional outflow.

2.3 Analysis

2.3.1 The Physical Environment of O VI Absorbers

The production of O VI is thought to take place in two very different environments: either low density, photoionized plasmas such as would be found in the Ly-α forest, or shock heated, collisionally ionized plasmas, as would be found at the interface between dense structures and the general IGM. The common association we observe between O VI absorbers and strong, metal-rich H I systems causes us to favor *a priori* the collisional hypothesis. In the following sections, we draw comparisons between the measured properties of the O VI absorption and the predictions of ionization simulations to see if the two are consistent with this qualitative conclusion.

For the ionization calculations, we have used the CLOUDY96 software package (Ferland et al., 1998). The gas was modeled as an optically thin plane-parallel slab in the presence of a Haardt and Madau (1996) shaped ionizing background spectrum for $z = 2.5$. The intensity of the ionizing background was normalized to $J_{-21} = 1.0$ (Scott et al., 2000), and the gas assumed to have a metallicity of $Z = \frac{1}{10} Z_{\odot}$ with solar relative abundances for the heavy elements. A grid of models was then computed by varying the gas density and examining the resulting ionization fractions and column densities of observable ions. For one of the runs, the temperature was allowed to converge on the thermal photoionization equilibrium value. Then, subsequent runs were performed at increasing fixed temperatures, to examine the effect of collisional processes on the ionization balance of the gas.

2.3.1.1 Pathlength and Gas Density Constraints

With the aid of the ionization simulations, it is straightforward to calculate the absorption pathlength through a cloud given its column density:

$$L = \frac{N_{\rm O\ VI}}{n_H f_{\rm O\ VI}} \left(\frac{O}{H}\right)^{-1}. \tag{2.2}$$

Here the oxygen abundance is an input to the simulations, and the ionization fraction $f_{\rm O\ VI} = n_{\rm O\ VI}/n_O$ is output as a function of the gas number density n_H. Figure 2.19 depicts this relation for a cloud with $N_{\rm O\ VI} = 10^{13.5}$ cm^{-2} of O VI absorption, which corresponds approximately to the weakest system in the survey. The right axis of the plot shows the instrinsic line broadening expected for structures of different sizes due to Hubble expansion. Again, we assume a flat, $\Omega_M = 0.3, \Omega_\Lambda = 0.7$ cosmology, for which $H(z = 2.5) = 239 h_{65}$ km s^{-1} Mpc^{-1}. The solid line represents the photoionization equilibrium solution; other lines represent fixed temperature solutions as indicated.

By comparing the broadening due to the Hubble flow with the observed distribution of b pa-

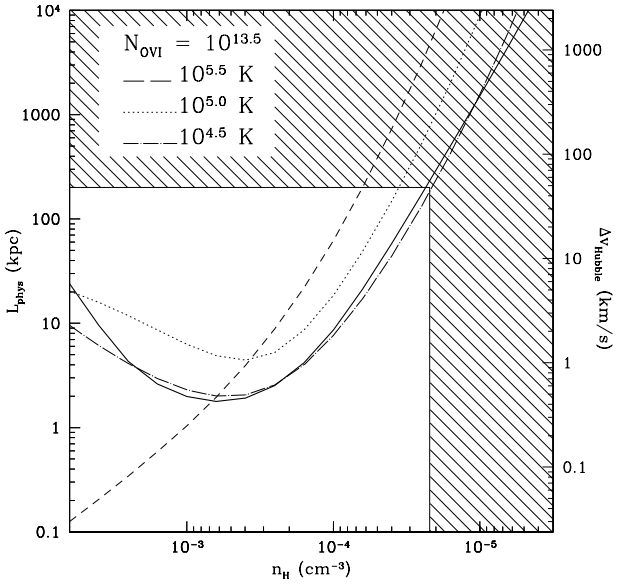

Figure 2.19 O VI absorption pathlength for a line with $N_{\rm O\ VI} = 10^{13.5}$ cm^{-2}, for different gas number densities, derived from CLOUDY calculations. The right axis shows the expected broadening $\Delta v = H_{(z=2.5)}L$ for lines corresponding to structures of different sizes. The solid line shows the photoionization equilibrium value; other lines indicate solutions at fixed temperatures as indicated. The shaded portions of the diagram are ruled out by the observed linewidths, which have an upper limit of 48 km/s. The excluded region in density is derived from the most conservative model curve (the photoionization equilibrium model). Note that the density scale is shown decreasing to the right, for consistency with Figures 2.21 and 2.22.

rameters, the data shown in Figure 2.19 may be used to constrain the sizes and gas densities of the O VI absorbing regions. In the figure, we have shaded the region above $\Delta v_{\rm Hubble} = 48$ km/s, which represents the maximum b parameter measured from the O VI lines in the survey. A series of tests has shown no substantial dropoff in the completeness of our sample with increasing b out to $b \sim 50$ km/s, except for the weakest lines (See Section 2.3.1.4). We therefore expect that we could have detected modestly broader lines if they existed in the data, though it is possible that very broad lines ($b \sim 100$ km/s) might be missed.

Referring to Figure 2.19, the choice of $b_{max} = 48$ km/s coupled with a pure photoionization model provides the most conservative lower limit on the O VI gas density, at $n_H \geq 2 \times 10^{-5}$ for a cloud of size $L \leq 200$ kpc (shown as the unshaded region). According to this prescription, and assuming that $\Omega_b h_{100}^2 = 0.02$ (O'Meara et al., 2001) we find that at $z = 2.5$ the O VI absorption lines arise in structures with $\rho/\bar{\rho} \geq 2.5$. In reality, most of the lines we observe are much narrower, with a median width of $b_{\rm O\ VI} = 16$ km/s. Use of this value instead of the more conservative 48 km/s yields a characteristic pathlength of $L \sim 60$ kpc, and a density limit roughly twice as high. If the model metallicity were reduced to $0.01 Z_\odot$, the lower limit on $\rho/\bar{\rho}$ would rise further by a factor of ~ 3, or if the gas were hot and collisionally ionized $\rho/\bar{\rho}$ would increase by a factor of ~ 3.5.

In short, we find from comparison of the simulations to observed linewidths that O VI absorbers have sizes of $L \leq 200$ kpc and overdensities of $\rho/\bar{\rho} \geq 2.5$, with true typical values probably nearer $L \sim 60$ kpc and $\rho/\bar{\rho} \sim 10-30$. Cosmological simulations suggest that such structures may correspond to previously metal-enriched gas which is in transition from the cool, distributed Ly-α forest to a denser, more compact phase (Zhang et al., 1995; Cen et al., 1994; Cen & Simcoe, 1997). It is in this neighborhood ($10^{-5} < n_H < 10^{-4}$) that the temperature-density relation for the photoionized Ly-α forest begins to break down due to shock heating of the infalling gas (McDonald et al., 2000).

2.3.1.2 Temperature Structure

In principle, one of the most powerful methods for distinguishing between photoionized and collisionally ionized O VI is simply to measure the temperature of the gas. Clouds found in the more tenuous regions of the IGM are in photoionization equilibrium, and exhibit a maximum characteristic temperature of $T \sim 40,000$ K. The effect of collisional ionization at this temperature is minimal. Indeed, collisional processes only become important above $T > 10^5$ K, and as the temperature rises they soon dominate the physics of the gas regardless of its density. The O VI ionization fraction peaks at $T \approx 10^{5.5}$ K (Sutherland & Dopita, 1993).

In practice, this ideal bimodal temperature distribution with peaks at $T \sim 20,000$K and $T \sim 300,000$K is not observed. Line broadening in cool, low density photoionized gas is enhanced by Hubble expansion and peculiar velocities. However, we find that the statistical distribution of O VI linewidths relative to those of other species does provide some evidence that the O VI gas is distinct from that of the other ions. Figure 2.20 illustrates these distributions for C IV , Si IV , and O VI, expressed as the temperature $T_{max} = A(b/0.129)^2$, where b is the measured line width and A is the atomic mass number of each ion. Since this estimate of the temperature does not account for non-thermal broadening, T_{max} represents only an upper bound on the gas temperature for a given line.

Despite this limitation, we find that the O VI distribution differs significantly from those of the other ions in the sense that it favors broader lines. A qualitative similarity between the Si IV and C IV distributions is confirmed by a Kolmogorov-Smirnov test, which indicates with 88% probability that they are drawn from the same parent population. The probablility that the O VI shares the same parent distribution was found to be only 0.0006%. The evidence suggests that the gas producing the O VI absorption is physically distinct from, and probably hotter than a second phase which is the source of both C IV and Si IV . While the temperatures plotted represent only upper limits, it is intriguing that the O VI histogram is distributed roughly evenly about $\log(T_{\rm max}) = 5.5$, the temperature at which the collisional ionization of O VI peaks (shown as a solid vertical line). In fact, the median value of $T_{\rm max}$ for O VI is 2.1×10^5 K, and and 62% of all systems lie in the range $5.0 \leq \log T_{max} \leq 6.0$. While this does not constitute direct evidence of a hotter O VI phase with

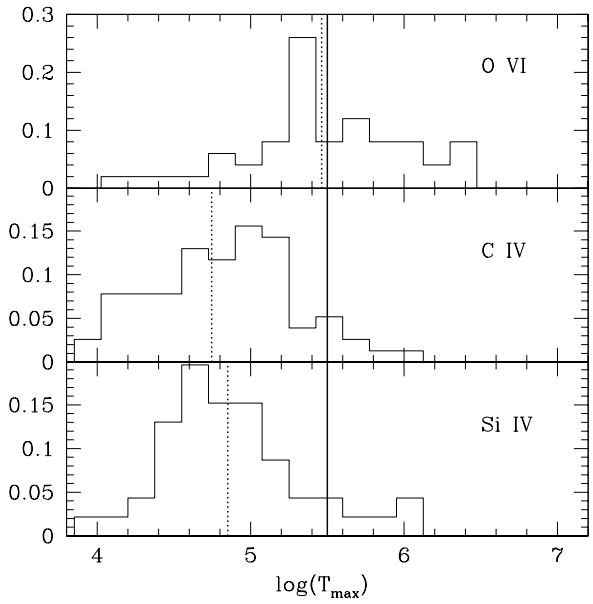

Figure 2.20 Histogram of upper limits on the temperature for all O VI, C IV, and Si IV components observed in our systems, assuming completely thermal line broadening. The solid vertical line drawn at $\log(T_{\rm max}) = 5.5$ indicates the approximate temperature where collisional production of O VI should peak. The three vertical dashed lines indicate the mean value of $T_{\rm max}$ for each ion. The C IV and Si IV temperatures are clearly too low to support the collisional ionization of O VI, and appear to be contained in a diferent phase than the O VI. The distribution of $T_{\rm max}$ for O VI tentatively appears to favor hotter temperatures characteristic of collisionally ionized O VI, though the true distribution may be lower due to non-thermal (e.g., turbulent) line broadening.

significant collisional ionization, it is at least consistent with such an interpretation.

2.3.1.3 Multiphase Structure

The evidence presented thus far indicates that high redshift O VI is found in the neighborhood of complex systems where multiple gas phases coexist. In this section, we examine the CLOUDY predictions of relative absorption strengths for different ions, in an attempt to identify the distinguishing physical characteristics of these phases. We recall that for these calculations, the relative element abundances are held fixed at the solar level.

Figures 2.21 and 2.22 illustrate the predictions for the column density ratios $N_{\rm C\ IV}/N_{\rm Si\ IV}$ and $N_{\rm O\ VI}/N_{\rm C\ IV}$ (expressed in logarithmic units). In both plots, the solid line represents a thermal photoionization equilibrium (PIE) solution, and other lines represent runs made at fixed temperatures to isolate the effects of collisional ionization as the gas is heated. The PIE curve and the $T = 10^{4.5}$ K curve are quite similar for both O VI/C IV and C IV/Si IV , indicating as expected that collisional processes have minimal effect on the ionization balance at low temperature. As the temperature rises, collisional processes tend to drive the column density ratios toward the expected value for pure collisional ionization equilibrium (CIE, with 1.9 for $N_{\rm C\ IV}/N_{\rm Si\ IV}$, and 2.1 for $N_{\rm O\ VI}/N_{\rm C\ IV}$, again in

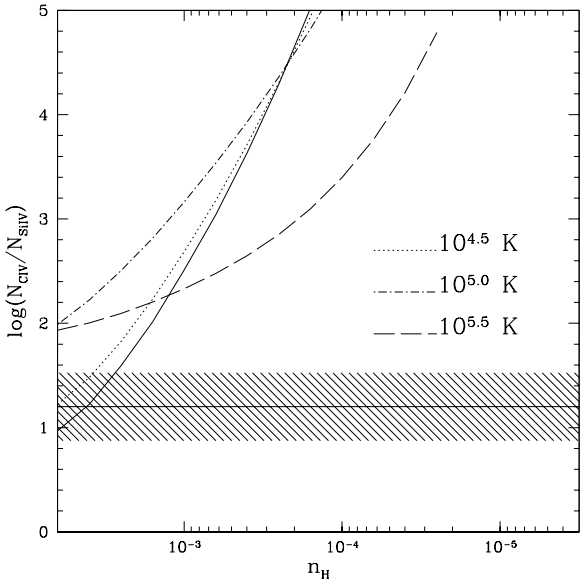

Figure 2.21 C IV /Si IV column density ratio predicted by CLOUDY as a function of gas number density (Note that the density scale *decreases* to the right, corresponding to an increasing ionization parameter). The solid line is the photoionization equilibrium solution, other lines are at fixed temperatures. The shaded region indicates the $\pm 1\sigma$ range in the ratio measured in O VI systems where both Si IV and C IV were detected. Models with $T > 10^{4.6}$ K are ruled out at any density; the most likely model is a photoionized gas with $n_H \geq 4 \times 10^{-3}$ at $T = 1 - 5 \times 10^4$ K. This temperature is consistent with measurements of the C IV and Si IV linewidths, when one uses both ions to solve for the thermal and non-thermal contributions to line broadening simultaneously.

logarithmic units). This value is roughly density-independent, as the collisional ionization rate and recombination rate both vary as n_H^2. Accordingly, at high densities where PIE tends to favor lower ion ratios than does CIE, the ratios rise with temperature. In both cases this transition is quite abrupt—we see that the high density gas changes from a photoionization-dominated state to a collisionally ionized state over a factor of 3 range in temperature. At low densities, the tradeoff between collisional and photon processes differ in Figures 2.21 and 2.22. For C IV /Si IV , at low density the CIE ratio is actually lower than the PIE value: an increase in temperature only increases the recombination rate, and drives the ratio downward. For the O VI/C IV case, the CIE and photoionization equilibrium ratios are similar, so the combined processes enhance the O VI/C IV ratio 7-10 times higher than the expected value for either process acting alone.

In Figure 2.21, we have shaded a region which approximates the $\pm 1\sigma$ range of values for C IV /Si IV that we detect in the survey. The only region where the data and models overlap is at high density and low temperature: the data rule out models with densities below $n_H \sim 3 \times 10^{-3}$, or gas temperatures above 10^5 K at any density. Evidently, the C IV and Si IV absorption arise in a fairly dense phase ($n_H \sim 5 \times 10^{-3}$) which is in photoionizaton equilibrium with the UV background, at $T \sim 1 - 5 \times 10^4$ K. These properties are identical to the C IV and Si IV systems commonly observed

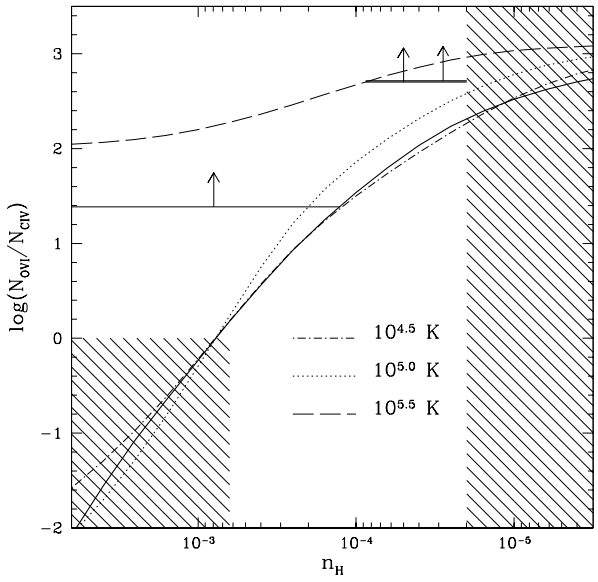

Figure 2.22 O VI/C IV column density ratio predicted by CLOUDY as a function of gas number density (Note that the density scale decreases to the right, as in Figure 2.21). Solid line represents a photoionization equilibrium solution, other lines are at fixed temperatures as indicated. Shaded region at right is excluded based on the pathlength arguments presented in Section 2.3.1.1. Shaded region at lower left is excluded based on the observed properties of C IV and Si IV . Horizontal solid lines indicate upper limits on the ratio from the two systems where a measurement could reliably be made. For most systems, an accurate measurement could not be made because of confusion in the C IV profile with absorption from the cooler carbon-silicon phase.

in quasar spectra, which have been extensively characterized (Songaila & Cowie, 1996; Boksenberg et al., 2003).

In Figure 2.22, we see that for the densities and temperatures inferred for C IV and Si IV , the predicted O VI strength should be quite small—10-100 times weaker than C IV , and therefore likely undetectable. In other words, we find that whenever coincident absorption of C IV and Si IV is observed, models require a separate, colder, condensed gas phase that is unlikely to be seen in O VI. This argument may be extended to other low ionization species such as Si II, Si III, or C II as well. Strong O VI observed in connection with these systems *cannot* come from the same gas as the C IV and Si IV—it must be contained in a separate gas phase. This conclusion is consistent with the interpretation of the temperature distributions given in 2.3.1.2. It is also consistent with the visual appearance of the line profiles, whose C and Si substructures match closely, and appear to be independent of the O VI substructure.

It is difficult to place firm constraints on the ionization mechanism for O VI itself precisely because of this multiphase nature. In the C IV region, relatively strong and defined absorption from the cool carbon-silicon phase masks the presence of any weak C IV that might be associated with a hot O VI phase, rendering an accurate measurement of O VI/C IV impossible. In theory, the

O VI/N V ratio should also provide a useful ionization probe, but unfortunately in our spectra the N V region is contaminated by interloping Ly-α forest absorption in nearly every O VI system.

For two systems, it is possible to obtain accurate lower limits on the O VI/C IV ratio due to velocity offsets between O VI and the cold C IV /Si IV phase. In Figure 2.22, we have shown these measurements as horizontal lines with arrows. We have extended the lines over the range in density framed by the complete photoionization model and the complete collisional ionization model, except where this violates the shaded constraints which are described below. For one of these systems (located at $\log(N_{\rm O\ VI}/N_{\rm C\ IV}) \sim 2.5$) the lower limits cannot be explained except through collisional ionization. For the other (located at $\log(N_{\rm O\ VI}/N_{\rm C\ IV}) \sim 1.4$ due to lower signal-to-noise in the C IV region) a pure photoionization model is allowed, but only at $n_H \sim 10^{-4}$. This is significantly lower than what is seen for the cooler C IV /Si IV phase present in many absorbers. Collisional solutions are also allowed for this system over a wide range of densities.

Given that the accuracy of direct O VI/C IV measurements is limited, we instead examine Figure 2.22 to determine which regions may be reasonably excluded from consideration. First, based on the pathlength/density constraints described in 2.3.1.1, we exclude the shaded region to the right of the figure corresponding to the $\rho/\bar{\rho} \sim 1 - 2.5$ Ly-α forest. The lower left region of the diagram, corresponding to a high density phase in PIE, may also be ruled out because it cannot be simultaneously reconciled with the C IV and Si IV line strengths.

Two allowed regions remain: one to the upper left of the diagram, and one covering the middle of the plot, in the density range $2 \times 10^{-5} < n_H < 2 \times 10^{-4}$. The first of these corresponds to condensed structures with similar overdensities as the C-Si phase ($\rho/\bar{\rho} \geq 100$), but which are hot ($T > 10^5$ K) and essentially entirely collisionally ionized. The second allowed region covers the overdensity range $3 \leq \rho/\bar{\rho} \leq 30$, in the transition area between the Ly-α forest and condensed structures. Both photoionization and collisional ionization are viable mechanisms for O VI production in this regime. Since the density is only an order of magnitude higher than in the Ly-α forest the gas can be efficiently ionized by the UV background, but simulations also indicate that as structures with these densities collapse, shocks at the IGM interface heat the gas to $T = 10^5 - 10^7$ K where collisional ionization should dominate (Cen & Ostriker, 1999; Davé et al., 2001; Fang & Bryan, 2001). It is likely that the ionization balance in this density range is actually governed by a mixture of the two processes, where gas that is already somewhat highly photoionized has its ionization level enhanced further upon rapid heating.

The results of this section may be summarized as follows. Comparison of O VI, C IV, and Si IV line ratios indicates that a multiphase structure is required to explain the simultaneous existence of highly ionized O VI and lower ionization species such as Si IV . The low ionization elements are contained along with C IV in a cool, condensed phase with overdensities of $\rho/\bar{\rho} > 100$ and $T \sim 1 - 5 \times 10^4$ K. This gas is in photoionization equilibrium with the UV background and its properties are identical

to the C IV and Si IV systems commonly seen in quasar spectra. The O VI gas is contained in a separate phase, which traces either high density ($\rho/\bar{\rho} > 100$), high temperature ($T > 10^5$ K) gas, or structures of overdensity $3 < \rho/\bar{\rho} < 30$ at the boundary between condensed regions and the distributed IGM.

2.3.1.4 Constraints on Number Density and Cross Section

Let us now examine constraints on the number density (n) and cross section (σ) of high redshift O VI systems. In this context, we refer to a "system" as a physical complex of gas, which may contain several individual subcomponents or lines. Assuming that both n and σ are constant throughout the survey volume, the expected number of O VI detections is given as

$$N = f_c \left(n\sigma \times \frac{c}{H_0} \sum \Delta X \right) \tag{2.3}$$

where $\sum \Delta X$ is the survey pathlength defined in Equation 2.1. The factor f_c is an estimate of the survey's completeness, to account for lines that remain undetected due to blending from the Ly-α forest.

To quantify the completeness, we have run a series of tests where artificial O VI doublets were added to each survey sightline to measure the recovery efficiency of our seach method. The column densities and doppler b parameters of these lines were assigned according to the same joint probability distribution $p(b, N)$ as the actual lines detected in the survey. Furthermore, we imposed a lower limit on the O VI column density of $\log(N_{\rm O\ VI}) \geq 13.4$—the strength of the weakest intergalactic system found in the survey. Five such realizations were generated for each quasar sightline, and the numbers and properties of the artificial lines were hidden from the users to avoid any bias in the search process. This sample does not test whether the systems detected in the survey are representative of the parent population of all O VI absorbers; however, it does provide an accurate estimate of the fraction of systems like those observed that remain undetected.

Upon searching the generated spectra in the same manner as the survey data, we consistently recovered $\sim 40\%$ of the artificial O VI lines with individual sightlines ranging from 38% to 44%. Closer examination revealed that essentially all of the unrecovered lines were lost due to blending with H I rather than a poor signal-to-noise ratio. In clean portions of the spectra, our detection threshold varied between $12.0 \leq \log(N_{\rm O\ VI}) \leq 13.0$, which is almost an order of magnitude below the level where blending from the forest begins to cause completeness problems. Our search method was most effective at recovering systems with $\log(N_{\rm O\ VI}) \geq 13.5$. Above this column density the completeness is probably $45-50\%$ and shows surprisingly little dependence on the doppler parameter until one reaches $b \leq 10 - 15$ km/s, at which point the efficiency goes up dramatically. For $b \geq 15$, the completeness is nearly constant with b at $\sim 35\%$ all the way to $b \sim 50$, the largest doppler

parameter measured in the survey. At column densities below $\log(N_{\rm O\ VI}) = 13.5$ the completeness begins to drop, and not surprisingly the lines that are lost tend to be broad, weak lines in blends. However, even at lower column density we recover the narrow lines ($b < 20$ km/s) in roughly $20-25\%$ of the cases. For the calculations below, we have adopted a completeness level of $f_c = 0.41$, which corresponds to the average for all sightlines, and includes the entire range of column densities and doppler parameters seen in the survey.

Given that we have detected 12 intergalactic systems in a path of $\sum \Delta X = 6.90$, we can invert Equation 2.3 to constrain the product of the space density and size of the O VI absorbers. For spherical O VI clouds with (proper) radius R and (proper) density n, we find

$$\left(\frac{n}{1\ {\rm Mpc}^{-3}}\right)\left(\frac{R}{17\ {\rm kpc}}\right)^2 = 1.0. \tag{2.4}$$

We note that a characteristic cloud size of $L = 2R \sim 40$ kpc is roughly consistent with estimates made using the completely different method of pathlength calculation from ionization simulations described in 2.3.1.1. The implied volume filling factor for such clouds is quite small at $f_v = 2.0 \times 10^{-5}\left(\frac{R}{17{\rm kpc}}\right)$. Taking into account the size constraint $R = L/2 < 100$ kpc from Section 2.3.1.1, we estimate $f_v \leq 1.1 \times 10^{-4}$. It therefore seems unlikely that the clouds are generally distributed, as in the Ly-α forest whose filling factor is much more substantial. The cross sectional constraint is more consistent with a compact topology, as one might expect to find in the surrounding areas of galaxies or clusters.

2.3.1.5 Clustering Behavior

In Figure 2.23, we show the two-point correlation function (TPCF) of the O VI absorbers. Special care was taken to account for the effects of spectral blockage from the Ly-α forest when calculating the TPCF. To produce the version shown in the figure, we have simulated 1000 realizations of the set of 5 sightlines from the survey. Selection functions were carefully constructed for each sightline, excluding regions where strong lines in the actual data prohibit O VI detection (roughly $\tau > 0.5$). Each simulated sightline was populated with O VI at random redshifts, requiring that both components of the doublet fall in an unblocked region of the spectrum. The randomly distributed systems were then collated by pairwise velocity separation, and compared to the distribution of velocity separations in the data to calculate the correlation: $\xi(\Delta v) = N_{\rm data}(\Delta v)/N_{\rm random}(\Delta v) - 1$.

Although we have only identified 12 O VI systems in the data, each system has several subcomponents and for the calculation of the correlation function we have used the full set of these subcomponents as determined by VPFIT. The TPCF constructed in this way probes the structure both within individual systems and between different systems. Poisson errorbars (1σ) are shown in the Figure to indicate the level of uncertainty due to finite sample size.

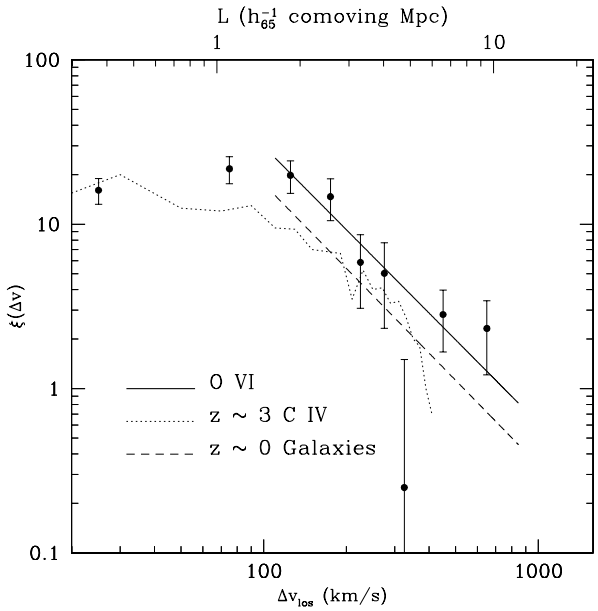

Figure 2.23 Two-point correlation function of O VI clouds along the line of sight for all intergalactic systems in the survey. The errorbars represent 1σ uncertainties due to finite sample size. The solid line denotes our best fit power law, given in Equation 2.5. For comparison, the C IV correlation function from Rauch et al. (1996b) is shown as a dotted line, and the correlation function of local galaxies (Loveday et al., 1995) is shown as a dashed line.

The data show evidence for strong clustering at separations of $\Delta v < 300$ km/s, and a weaker signal out to $\Delta v \sim 750$ km/s. This clustering pattern differs from that of the Ly-α forest, which shows almost no signal except for a weak amplitude at the shortest velocity scales ($\Delta v \sim 100$ km/s, Cristiani et al 1997). We have also calculated the TPCF for the C IV absorption associated with our O VI selected systems using the same window function, to test for differences between the O VI and C IV clustering properties within our sample. Except at the smallest velocity separations ($\Delta v < 100$ km/s) which probably reflect the internal dynamics of the systems more than their spatial clustering, we find no statistically significant differences between the O VI and C IV clustering in the O VI selected systems. At small separations the O VI clustering amplitude is $\sim 50\%$ lower than that of C IV , likely a reflection of the smoothness of the O VI absorption profiles.

For reference, Figure 2.23 also shows the TPCF for a larger sample of C IV absorbers that is not O VI selected, taken from Rauch et al. (1996b). In general, the O VI correlation resembles that of the larger C IV sample. There is some evidence for an enhancement of O VI clustering at the $\sim 2\sigma$ level for $70 \leq \Delta v \leq 200$ km/s. This excess clustering is seen in the O VI selected C IV lines as well, and may reflect the qualitative impression that O VI is often associated with very strong, kinematically complex absorption systems. More inclusive samples such as Rauch et al. (1996b) pick up a larger fraction of weaker H I systems that have one or a few C IV components.

The range over which we measure correlation signal in O VI extends to larger values than the

$100 - 200$ km/s typical of virialized, galactic scale structures. This could mean that the individual O VI lines, which arise in structures of $L \sim 60 h_{65}^{-1}$ kpc, actually trace large-scale structure in an ensemble sense. According to this picture, the signal at large velocity separations—corresponding to coherence at $L \sim 7 - 10 h_{65}^{-1}$ comoving Mpc scales—results from chance alignments with cosmological filaments along the line of sight. The solid line in Figure 2.23 represents a simple power law fit to the TPCF over the range $100 \leq \Delta v \leq 1000$ km/s. We find

$$\xi(\Delta v) = \left(\frac{\Delta v}{750 \text{ km/s}} \right)^{-1.68} . \tag{2.5}$$

The form of this power law is similar to its three dimensional analog measured in local galaxy redshift surveys, which find best fit exponents of $-1.7 < \gamma < -1.8$ (Connolly et al., 2002; Norberg et al., 2001; Le Fevre et al., 1996; Loveday et al., 1995). For comparison, we have shown the correlation function of local galaxies measured from the Automated Plate Measuring (APM) survey (Loveday et al., 1995) as a dashed line in Figure 2.23. If the high velocity tail of the O VI TPCF is driven by cosmological expansion alone, then the correlation length for O VI at $z = 2.5$ is $L = 10.8 h_{65}^{-1}$ comoving Mpc. This is slightly larger than the galaxy correlation length found in the APM and other local surveys, but it is less than that of clusters at the present epoch (Bahcall, 1988). At higher redshift, Lyman break galaxies show a similar power law slope, though the amplitude is somewhat weaker than for O VI (Giavalisco et al., 1998). In most structure formation models the the overall normalization of the power law is predicted to evolve with redshift (Benson et al., 2001) but not the slope. The -1.7 power law for the O VI TPCF is therefore a natural outcome if the O VI systems are tracing large-scale structure.

Thus far we have ignored the effects of peculiar velocities on the TPCF. The signature of gas motions within the potential wells of L^* type galaxies has been well documented (Sargent et al., 1988), and it is thought that such motions are unlikely to account for signals on scales of $\Delta v > 150$ km/s. However, for highly ionized gas such as O VI one might expect to see correlations on larger velocity scales caused by galactic winds. In this scenario, pairwise velocity separations of $400 - 800$ km/s are produced in bidirectional outflows which drive material both towards and away from the Earth at projected velocities of 200–400 km/s.

To characterize this effect on the TPCF, we consider a naive, spherically symmetric outflow model where all material is ejected from a central source at a common velocity v_0. Assuming the outflow is finite in size, the area over which a given velocity splitting Δv can be observed scales as

$$A(\Delta v) \propto 1 - \left(\frac{\Delta v}{2 v_0} \right)^2 , \tag{2.6}$$

with a maximum observable $\Delta v = 2 v_0$ when the outflow vector is parallel to the line of sight. The

area-weighted mean velocity splitting for this model is $\langle \Delta v \rangle = \frac{3}{4} v_0$. For $v_0 = 400$ km/s, which is chosen to match the high-end cutoff in the TPCF for our data and represents a reasonable ejection velocity for starburst-driven winds (Lehnert & Heckman, 1996; Pettini et al., 2001), the model predicts a maximum in the correlation signal at $\Delta v \sim 300$ km/s. It also predicts that roughly equal numbers of pairs should be observed with splittings above and below 300 km/s—i.e., the TPCF should be much flatter than what is actually observed. This problem with the wind model could in principle be solved by assuming a distribution in wind ejection velocities skewed toward low values, or a hybrid model where the correlation signal at low Δv is dominated by motions within galaxy potentials and the large separation pairs are caused by winds. Given that such models would require significant tuning, and that a power law fit motivated by local observations of large-scale structure matches the data reasonably well, the simplest interpretation is that the O VI TPCF signal is dominated by large-scale structure.

Ultimately, comparison of the O VI TPCF with simulations of structure formation can provide a more realistic physical description than we attempt here. Also, we note that the lack of strong outflow signature in the O VI-O VI TPCF does not preclude the existence of O VI rich winds. In a bipolar outflow geometry, a single sightline might only encounter one of two lobes. In this case, velocity offsets between O VI and other ions such as C IV provide better probes of the wind physics than O VI-O VI comparisons.

2.3.2 The Contribution of Warm-Hot Gas to Ω_b

Having completed our analysis at the level of individual systems, we now estimate the contribution of the total ensemble of O VI systems to the baryon budget. For this discussion, we shall use the term $\Omega_{\rm WH}$ to denote the cosmological mass density of the *complete warm-hot gas mixture* containing O VI; when referring only to the contribution of quintuply ionized oxygen atoms to the closure density we use the term $\Omega_{\rm O\ VI}$. The former contains ionization and abundance corrections which are highly uncertain, while the latter is a direct observable. For the calculation of $\Omega_{\rm WH}$, we use a slightly modified version of the the standard formula (Tripp et al., 2000; Burles & Tytler, 1996) for the cosmological mass density:

$$\Omega_{\rm WH} = \frac{1}{\rho_c} \times \frac{\mu m_H}{f_{\rm O\ VI}} \left(\frac{O}{H}\right)^{-1} \times \frac{\frac{1}{f_c} \sum N_{{\rm O\ VI},i}}{\frac{c}{H_0} \sum \Delta X_i}. \tag{2.7}$$

The outer terms in this equation are easily calculated, the first being a normalization to the critical density at the present epoch, and the third being the cosmological number density of O VI ions, expressed as the ratio of the total O VI column density to the total comoving pathlength of the survey. The $\frac{1}{f_c}$ factor accounts for incompleteness, and its determination is described in Section 2.3.1.4. The second term—a conversion from number density of O VI ions to mass density of a gas

mixture containing O VI—is highly uncertain and contains the abundance and ionization fraction corrections mentioned above. For ease of comparison with local O VI surveys, we have adopted the same values as Tripp et al. (2001) for these quantities—a mean atomic weight of $\mu = 1.3$, an O VI ionization fraction of $f_{\rm O\ VI} = n_{\rm O\ VI}/n_O = 0.2$, and an oxygen abundance corresponding to $\frac{1}{2}Z_\odot$ for $\log\left(\frac{O}{H}\right)_\odot = -3.17$ (Grevesse & Sauval, 1998). As noted by Tripp et al, the values for the ionization fraction and oxygen abundance represent upper limits—indeed, at high redshift the abundance in particular is likely to be lower by as much as a factor of $50 - 100$. As such, the value of $\Omega_{\rm WH}$ we derive is only a lower bound.

Combining Equation 2.7 with our survey results, the assumptions described above, and the incompleteness correction, we obtain the following lower limit on the cosmological mass density of warm-hot gas:

$$\Omega_{\rm WH} h_{65} \geq 0.00032, \tag{2.8}$$

or about 0.5% of the total Ω_b. This result is consistent with the generally accepted model of the high redshift IGM, where most of the baryons ($\geq 90\%$) are contained in the relatively cool and less dense ($T \sim 10^4$ K, $\rho/\bar{\rho} \sim 1 - 5$) Ly-$\alpha$ forest network (Rauch et al., 1997c; Weinberg et al., 1997).

Our result is very similar to the most recent low redshift estimates of $\Omega_{\rm WH}$ from FUSE and STIS/HST, which indicate $\Omega_{\rm WH} h_{65} \geq 0.00046$ at $z \sim 0$—only $\sim 25\%$ higher than our $z = 2.5$ estimate (Savage et al., 2002) [2]. It is also in agreement with the estimate of Burles and Tytler (1996) made at intermediate redshift ($0.5 < z < 2$) using lower resolution FOS data, provided one rescales their measured quantities to match our (and Tripp's) assumptions.

The weak evolution we observe in $\Omega_{\rm WH}$ is in apparent contradiction with simulations, which describe the properties of low redshift O VI quite accurately, but predict a decrease in $\Omega_{\rm WH}/\Omega_b$ from $\sim 30 - 40\%$ at $z = 0$ to $\sim 1 - 10\%$ at $z = 2.5$ (Cen & Ostriker, 1999; Davé et al., 2001; Fang & Bryan, 2001; Chen et al., 2002). Both our measurements and those of Savage et al. (2002) are only lower limits, but Equation 2.7 illustrates that with the observed quantities essentially constant, the only way to produce a strong decrease in $\Omega_{\rm WH}$ towards higher redshift is to let the product of $f_{\rm O\ VI} \times \left(\frac{O}{H}\right)$ *increase* with redshift. This is somewhat surprising since one generally expects the cosmic metallicity to be lower at earlier epochs.

A possible explanation for this effect could be that the type of system being traced by O VI differs at high and low redshift. For example, the low redshift O VI could be found in cosmological filaments and sample metallicies closer to the cosmic mean, whereas the high redshift systems could be located near galaxies or groups and be subject to local metallicity enhancements and/or heating processes.

[2]Note that for this calculation we have matched our metallicity and ionization assumptions to the *most conservative* set of assumptions from Savage et al. (2002) and Tripp et al. (2000). The more commonly quoted value of $\Omega_{\rm WH} h_{65} \geq 0.002$ at low redshift is obtained by changing the assumed metallicity, so a comparison of this number with our survey would require a similar rescaling of $\Omega_{\rm WH}(z = 2.5)$ upward by a factor of 5. The 25% evolution we quote is a change in directly observable quantities (i.e., the third factor in Equation 2.7).

Such a scenario would explain both the agreement between low redshift observations and simulations, and also the similar values of $\Omega_{\rm WH}$ at low and high redshift.

Another factor is that the O VI we see in absorption does not trace the bulk of the mass in the warm-hot medium. In fact, from Figure 5 of Davé et al. (2001), we see that most of the gas—particularly at low redshift—should be hotter than the optimal range for O VI production, at $T > 10^6$ K. Prospects of detecting this gas are better in soft X-ray emission, or absorption from higher ionization lines such as O VII or O VIII. Indeed spectra taken recently with Chandra-HETG may have already revealed the presence of intergalactic $T > 10^6$ K gas through such absorption (Fang et al., 2002; Nicastro et al., 2002).

If the majority of the warm-hot intergalactic medium resides in a reservoir of higher temperature gas, the relatively weak evolution we observe in $\Omega_{\rm WH}$ might be explained if the O VI traces a short-lived phase in the cooling cycle of a pre-heated plasma. Recent cooling models for highly ionized plasmas (Benjamin et al., 2001) show a peak in the cooling curve over the range $10^5 < T < 10^6$, where O VI should be most abundant. The interpretation of evolutionary trends in $\Omega_{\rm WH}$ may be complicated if the O VI only measures an instantaneous snapshot of rapidly cooling non-equilibrium gas, rather than the total amount of shocked gas integrated over cosmic time.

2.3.3 Metallicity Constraints

Because of the multiphase nature of the O VI systems, it is impossible to directly measure the oxygen abundance for individual absorbers. Typically, the cool phase that gives rise to C IV and Si IV also produces strong H I absorption which overwhelms the weaker H I signal from the hot gas, and leads to erroneously small estimates of [O/H]. Rather than attempting to disentangle the phase structure of these systems, we estimate the average metallicity of the gas in all O VI systems, using reasonable assumptions about the distribution of baryons in the high redshift universe.

If one assumes that the O VI systems we detect are distinct from the Ly-α forest, and that $\Omega_{\rm Ly\alpha}/\Omega_b \geq 0.9$ (i.e., $\Omega_{\rm WH}/\Omega_b \leq 0.1$; Rauch et al 1997b, Weinberg et al 1997), the solution of Equation 2.7 may be inverted to place constraints on the metallicity of the O VI absorbers:

$$f_{\rm O\ VI} \times \left(\frac{O}{H}\right) \geq \frac{\mu m_H}{0.1\ \Omega_b\ \rho_c}\ \frac{\frac{1}{f_c}\sum N_{\rm O\ VI,i}}{\frac{c}{H_0}\sum \Delta X_i} = 4.3 \times 10^{-6} \tag{2.9}$$

Combining this with our assumed upper limit of $f_{\rm O\ VI} \sim 0.2$, the corresponding limit on the metallicity is $[O/H] \geq -1.49$, or $Z \geq 0.03 Z_\odot$. This limit is higher than the commonly quoted value of $[O/H] \sim -2.5$ for the generally distributed IGM (Songaila & Cowie, 1996; Ellison et al., 2000; Schaye et al., 2000), but it is close to the average abundance measured in damped Ly-α systems, which also exhibit only minimal evolution in number density and metallicity over a wide range of redshifts (Prochaska & Wolfe, 2000; Ellison et al., 2001). If correct, this high metallicity estimate

suggests that the O VI systems in our survey are found near regions with significant local enrichment and do not probe the metal content of the more widespread IGM.

2.4 Discussion

In the preceeding sections, we have characterized O VI systems by their association with rare, high density environments in the early universe. However, we have not explicitly linked O VI production with any specific process occurring in this environment. In this section, we examine two of the most likely sources for O VI production: shock heating of the IGM as it falls onto dense structures (hereafter referred to as the infall hypothesis), and the ejection of galactic superwinds associated with high redshift star formation (hereafter the outflow hypothesis). Both of these processes play an important role in the assembly of galaxies and the chemical enrichment of the IGM, and both are known to occur at the redshifts probed by our survey. We cannot definitively distinguish which of these dominates on the basis of the O VI data alone, so we weigh the merits of each below.

2.4.1 Shocked Infall on Large-Scale Structure?

There is currently little observational evidence either for or against the existence of large-scale gas inflows at high redshift, but clearly the process is required to take place at some time in any viable structure formation model. In particular, the notion of O VI as a tracer of a shock-heated, warm-hot phase of the IGM has generated recent enthusiasm, because warm-hot gas provides a natural source of "missing baryons" at low redshift, and simulations have been fairly succesful at reproducing the observed numbers and strengths of low redshift O VI lines (Cen & Ostriker, 1999; Davé et al., 2001; Fang & Bryan, 2001; Tripp & Savage, 2000). In this scenario, low density gas in the IGM which has been chemically pre-enriched crosses shock boundaries as it settles onto large-scale structure. For post-shock temperatrues of $10^5 - 10^7$ K, hydrogen Ly-α absorption is suppressed by collisional ionization and the production of O VI and other highly ionized species is enhanced. At $z = 0$, the simulations predict that this O VI should be visible in absorption, and that most of the absorption should occur in widely distributed filamentary structure, away from the sites of formed galaxies.

While the prediction of a *filamentary* warm-hot phase at first seems to be at odds with the analysis presented here, it is important to note that this was made for the local universe, and that the warm-hot gas is expected to evolve strongly with time. Davé et al. (2001) have examined some of the evolutionary properties of the warm-hot IGM, and demonstrated that as one moves to higher redshift, the production of warm-hot gas is governed by the amount of time structure has had to accumulate and shock heat infalling gas. We therefore expect that at high redshift O VI should trace more overdense structures than it does locally, since these regions should be the first to accrete significantly and form shocks strong enough to heat gas above the thermal

photoionization equilibrium temperature.

The properties of the warm-hot gas whose evolution is explicity tracked by Davé et al seem to be in agreement with our observations at high redshift. For example, at $2 < z < 3$, the simulations predict that the mass of the warm-hot medium is dominated by structures with $10 < \rho/\bar{\rho} < 30$, which coincides with our crude overdensity estimates of $3 < \rho/\bar{\rho} < 30$ for O VI systems. Furthermore, the authors claim that warm-hot gas is distributed across a wide range in temperature, peaking near 10^6 K with negligible effects from radiative cooling. If most of the gas is trapped in this hot state which is unable to radiatively dissipate the heat generated from shocks, then as time progresses, an increasing portion of the mass in the warm hot phase will pile up in this reservoir that is too hot to be seen in O VI. Essentially, all the gas that is heated to temperatures above the O VI range will remain in this hot state, while the gas which is heated only to O VI temperatures will cool very efficiently via line radiation until the O VI recombines and is no longer seen. This could provide an explanation for the similar values we observe for $\Omega_{\rm WH}$ at low and high redshift, as the O VI would effectively trace only the instantaneous amount of gas undergoing shock heating, rather than the total amount of gas which has passed through a shock at some time in its history.

The overdensities seen in our survey fall in the range where structures in cosmological simulations make a topological transition from connected filaments to isolated spheres. Because of computational limits it is difficult to accurately predict the both the numbers and sizes of these clouds: the large simulation cubes required to minimize shot noise in n tend to resolve the structures of interest only marginally, while higher resolution grids tend to sample a small number of objects. For example, Cen and Simcoe (1997) use a large $10h^{-1}$ comoving Mpc box to estimate the numbers and sizes of discrete Ly-α "clouds" as a function of overdensity. For overdensities of $\rho/\bar{\rho} = 30$, they distinguish ~ 10 clouds/Mpc^{-3}, which have a median size of $R \sim 26$ kpc. Comparing these numbers to the $n\sigma$ product in Equation 2.4, we find that the observed value is overestimated by a factor of ~ 15. However, the true spatial resolution of this simulation at $z = 2.5$ is only ~ 30 physical kpc, so the structures of interest are not well-sampled. It is therefore possible that either the average cloud cross section is overestimated, or structures that would collapse to smaller highly overdense regions are smoothed by the simulation resolution, resulting in an overestimate of the number density.

The alternative approach is taken by Rauch et al. (1997a), who simulate a much smaller $1.4h^{-1}$ comoving Mpc box at higher resolution to study the assembly of proto-galactic clumps (PGCs) and small galaxy groups. Mulchaey et al. (1996) have also outlined the expected observational signature of these type of structures. Their main prediction is that quasar sightlines passing through small groups should penetrate multiphase absorbers with strong H I . One of the phases is hot, highly ionized, and seen principally in O VI—this represents the intra-group medium. A second, cooler phase with lower ionization species (e.g., C IV, Si IV) is associated with the extended haloes of the galaxies themselves. The agreement between these predictions and our observations, as well as

observations of galaxy clustering at high redshift (Steidel et al., 1998; Venemans et al., 2002), lend merit to this hypothesis.

In Rauch et al. (1997a), the authors note the size of PGC structures at a given temperature, finding that gas with $T \geq 10^5$ K is found in spheroidal envelopes within ~ 30 kpc of PGCs at $z = 3$. From their Figure 2, we estimate that $\sim 2-3$ such regions exist in a volume of approximately 0.23 physical Mpc (scaled to $z = 2.5$). From Equation 2.4 we see that the implied $n\sigma$ product is again overestimated by a factor of $\sim 15-20$. However, the volume for this high resolution grid is not entirely representative, in that it was explicity chosen to include several proto-galactic clumps and probably overestimates the true global number density. Even with this selection, the small number of PGCs results in significant poisson error in n.

If the mapping between O VI absorbers and structures in the simulations is correct, and if the size and density estimates of the simulations are accurate, the overestimate of the $n\sigma$ product would argue against the widespread intergalactic distribution of oxygen, as has been suggested in connection with Population III enrichment scenaria. However, the good agreement between simulations and observations at low redshift suggests that inflow shocks are producing O VI at some level. Lacking direct access to simulations, our comparisons here are necessarily crude; a more sophisticated comparison with current and future generations of simulations is warranted to determine if the discrepancies at high redshift are essentially physical or numerical.

2.4.2 Tracer of Galactic Outflows at High Redshift?

The second mechanism we consider for O VI production is the collisional ionization of hot winds expelled from galactic environments. This model provides a natural explanation for the high metallicities we have found for the O VI systems in Section 2.3.3. Also, unlike infall models, the outflow hypothesis is supported directly by observations of galactic winds at high and low redshift (Pettini et al., 2001; Franx et al., 1997; Dawson et al., 2002).

The existence of large-scale galactic outflows is a well-documented phenomenon in the nearby universe, and is usually assocated with regions of intense star-forming activity (see Heckman 2001 for a review). Recent observations with the FUSE satellite have directly confirmed the presence of substantial O VI in a supernova-driven superbubble flowing out of the dwarf starburst NGC 1705 (Heckman et al., 2001). Many of this system's properties strongly resemble those of the systems found in our survey. These include the wind velocity ($\Delta v \sim 100$ km/s), the gas metallicity ($[O/H] \sim -1.5$), and column density ($N_{\rm O\ VI} \sim 10^{14.3}$). The physical gas density in the NCG 1705 wind is somewhat higher than the range we have considered at $n_H \sim 0.03$, but since the O VI in a galactic wind is dominated by collisional ionization, the gas density of the high redshift systems is essentially unconstrained and could take on any value. The gas in NGC1705 appears to be in a "breakout" phase, where the shell of an expanding bubble fragments in the wake of the wind. The

O VI is produced in a thin layer near the interface of the fragmenting shell and the onrushing gas, which is thought to be capable of escaping to large distances.

There is some evidence that winds may be even more frequent at high redshift, as the outflow signature is a ubiquitous feature in the spectra of Lyman Break galaxies (LBGs) at $z = 3$ (Pettini et al., 2001). These winds are seen in interstellar absorption lines which are blueshifted by several hundred km/s from the H II lines thought to trace the stellar population. As a simple consistency test, if we compare the comoving number density of LBGs ($\phi_* = 0.004$ Mpc^{-3}; Adelberger & Steidel 2000) with our estimates of the $n\sigma$ product for O VI absorbers, we find that at $z = 2.5$ LBGs can account for all of the observed O VI absorption in our survey if they blow winds out to radii of 41 kpc. This is in close agreement with size estimates for the O VI absorbers based upon pathlength considerations, and is easily achieved in superwinds like those seen in low redshift star forming galaxies (Lehnert & Heckman, 1996). For winds moving at $100 - 200$ km/s, the timescale required for a wind to entrain this volume is $\tau_{\rm wind} \sim 250 - 500$ Myr, or about 15% of the Hubble time at $z = 2.5$. This wind timescale is in agreement with the median star formation age of 320 Myr found from spectral fitting to the rest-frame optical colors of LBGs (Shapley et al., 2001). This does not establish a direct connection between LBGs and O VI production, but it demonstrates that known galaxy populations at high redshift could produce winds similar to those required to explain the properties of O VI.

2.5 Summary and Conclusions

We have performed a survey for O VI absorption in the intergalactic medium at $2.2 < z < 2.8$ along the lines of sight to five quasars. Eighteen O VI systems were identified, 12 of which constitute the primary sample for this paper. The remaining six systems are located near their respective background quasars, and are either ejected from the central engine or affected by the strong local radiation field. At high redshift, blending from the Ly-α forest is a significant limitation in O VI searches. Accordingly, we have provided quantitative estimates of both the completeness of the sample and its contamination level. The completeness—a measure of the fraction of true O VI systems that are detected (i.e. not blocked by the forest)—is $f_c \approx 41\%$. The contamination level, which measures the number of Ly-α line pairs in the forest masquerading as O VI doublets, is estimated at $\leq 10\%$ of our identified O VI systems.

The intergalactic systems we have detected share the following directly observable properties:

1. They are located in highly overdense environments. These regions are characterized by strong Ly-α absorption, either as a Lyman-limit system or as a collection of several clouds with $N_{\rm H\,I} \sim 10^{15.5}$. One O VI system is associated with a weak damped Ly-α absorber.

2. C IV absorption is seen in the environment of every O VI system, and other lower ionization species (Si IV , C II , Si III , Si II) are often present as well.

3. The detailed velocity structure of O VI does not generally match that of the other heavy elements. The O VI profiles typically show less substructure than C IV or Si IV , and are sometimes offset from lower ionization lines by several hundred km/s.

Our selection method has not revealed O VI lines associated with lower density regions of the Ly-α forest. Cosmological simulations (Hellsten et al., 1998; Rauch et al., 1997a) predict that photoionized O VI should be an efficient tracer of metals in clouds with $13.5 < \log(N_{\rm H\ I}) < 14.5$, yet we detect no intergalactic O VI lines near regions with H I column densities below $\log(N_{\rm H\ I}) = 14.6$. The survey data were originally taken to the standards required to detect O VI in forest lines with [O/H]=-2.5, and we find several clean systems where O VI should be seen in the data at this level but is not. However, there are many systems where we would not detect weak O VI because of forest blending or noise, and it remains to be seen whether this finding is statistically significant or is simply a reflection of cosmological scatter in the oxygen abundance or ionizing radiation field. These questions will be addressed in forthcoming work [3].

To aid in our interpretation of the detected systems, we have performed a suite of ionization simulations using the CLOUDY software package. Runs were made for the photoionization equilibrium case, and also at a range of fixed temperatures between $10^4 - 10^6$ K to investigate the onset of collisional O VI production. From comparisons between the observations and ionization calculations, we have assembled a basic physical description of high redshift O VI systems that may be summarized as follows:

1. Their physical extent and gas density may be conservatively constrained at $L \leq 200$ kpc and $\rho/\bar{\rho} \geq 2.5$. This was calculated by comparing the maximum observed O VI linewidth with the broadening expected for clouds of different sizes due to the Hubble flow. For the median observed value of $b_{\rm O\ VI} = 16$ km/s, the inferred cloud sizes and densities are $L \sim 60$ kpc and $\rho/\bar{\rho} \sim 10 - 30$.

2. They possess at least two distinct gas phases. One of these gives rise to absorption in photoionized C IV and Si IV , and has temperatures in the range $T = 20,000 - 40,000$ K, and overdensities of $\rho/\bar{\rho} \sim 500$. This is the same variety of gas which gives rise to the common C IV and Si IV absorption seen in all high redshift quasar spectra. The second phase is physically distinct, and traced only in O VI absorption. Its temperature is difficult to constrain because of uncertainties in the nonthermal contribution to line broadening. However, the distribution of $T_{\rm max}$ shown in Figure 2.20 indicates that the O VI temperature structure differs

[3] See Chapter 3 and Appendix A.

from that of C IV and Si IV , and favors higher temperatures where collisional production of O VI would be significant.

3. They are strongly clustered on velocity scales of $\Delta v = 100 - 300$ km/s, and show weaker clustering signal out to $\Delta v = 750$ km/s. The power law slope of the two-point correlation function is similar to that seen from local galaxy and cluster surveys, with a comoving correlation length of $\sim 11 h_{65}^{-1}$ Mpc, intermediate between galactic and cluster scales. While the correlation at large velocities could be the signature of galactic winds, a simple geometric wind model does not accurately predict the shape of the TPCF over the entire velocity range where signal is seen. We have argued that the signal in the O VI TPCF is dominated by the signature of large-scale clustering. This does not rule out the possibility that its shape is slightly modified by peculiar motions or outflows.

4. On average, they possess oxygen abundances of $[O/H] \geq -1.5$, about 10 times higher than the level observed in the general IGM. This level of enrichment probably requires additional metal input above the level supposed to originate from Population III stars. This conclusion assumes that the O VI absorbers contain $\leq 10\%$ of the baryons at high redshift, i.e., that they are distinct from the more tenuous IGM that gives rise to the Ly-α forest and contains $\geq 90\%$ of the baryons.

5. The integrated mass of warm-hot gas at $z \sim 2.5$ amounts to $\geq 0.5\%$ of Ω_b. This may be compared with the latest estimates of Savage et al. (2002), who measure $\Omega_{\rm WH}$ at low redshift to be only 25% higher using identical assumptions. If the average metallicity of the universe increases with time, the difference is even less pronounced. This relatively weak evolution may indicate that O VI is seen only during a short phase in the cooling history of pre-heated gas. In this case, the balance of the shock heated IGM, integrated over time, could reside in gas with $T > 10^6$ K, which has long cooling timescales and is not efficiently traced by O VI.

Based on the absorption data alone, we cannot make a strong distinction between the scenario where O VI is produced in wind-induced shocks, and the scenario where it is produced in accretion shocks due to structure formation. The high average metallicity we have measured in the O VI absorbers seems to point towards the wind hypothesis, though we cannot measure metallicities on a system-by-system basis. The overdensities we associate with the observed O VI systems are between those observed in the Ly-α forest and collapsed structures. At the low end of the allowed density range, O VI with properties similar to those observed can be produced through either collisional ionization or photoionization, though some systems can only be explained by collisional processes even at low density. At higher densities than $n_H \sim 3 \times 10^{-4}$ collisional ionization is required to explain the strength of O VI relative to other ions for solar relative abundances.

We have compared the O VI absorbers to structures of similar overdensity and temperature in cosmological simulations to test the plausibility of the accretion hypothesis. Using estimates of the number density and cross section of these structures, we find that the number of O VI detections predicted for the survey is too high by a factor of ~ 15. However, the comparison is not always straightforward because simulations in the literature typically contain either sufficient spatial dynamic range to resolve the scales of interest, or a large enough volume to minimize cosmic variance—but not both. The generation of simulations currently running should be able to address this question more accurately, to distinguish whether this discrepancy is physical or numerical.

A critical assessment of the wind model is also difficult, as current cosmological simulations are not capable of treating such a complex processes in full physical detail. However, we have compared our results with the most well studied population of wind-producing galaxies at high redshift, the Lyman break galaxies. Using current estimates of the LBG comoving number density, we find that they are capable of producing all of the observed O VI absorption if each LBG drives winds to a radius of ~ 41 kpc—similar to the size inferred from our pathlength analysis. Furthermore, the time required to drive winds to this distance at $v_{\rm wind} = 100 - 200$ km/s is in agreement with recent estimates of the star formation ages of the LBGs. While this coincidence does not constitute a direct connection between LBGs and O VI absorbers, it does demonstrate that known galaxy populations could plausibly give rise to the amount of O VI seen in our survey.

Ultimately, much of the warm-hot gas that has been suggested as a baryon reservoir at low redshift may be hotter than 10^6 K, and hence be undetectable in O VI. The fact that $T_{\rm max}$ for O VI spans the entire range from $10^5 < T < 10^6$ K without any clear peak suggests that the high temperature limit for O VI lines results from further ionization of the oxygen, rather than the actual detection of a maximum gas temperature. Gas which is shocked to temperatures of 2×10^6 K (near the peak of the predicted warm-hot temperature distribution from Davé et al 2001) at $\rho/\bar{\rho} \sim 5$ would have a cooling timescale of $\tau_{\rm cool} \sim 1.5$ Gyr, which amounts to 60% of the Hubble time at $z = 2.5$. At the same density, gas in the O VI temperature range cools ~ 30 times faster, owing to its lower initial energy, and its location at the peak of the cooling curve. If this is the case, then O VI absorption would trace the "tip of the iceberg" with respect to the total amount of warm-hot gas produced over cosmic time. In principle, the prospect of detecting the rest of the gas is better in O VII or O VIII X-ray absorption, but the number of extragalactic objects bright enough for high resolution X-ray absorption spectroscopy on current instruments is small, and all are at low redshift. The indications from the O VI data, along with a handful of O VII and O VIII detections, suggest that this hot gas exists, but it may be some time before it can be observationally characterized in a statistically robust sense.

Since the lifetime of gas in the O VI state is short, sources of energy input are needed to produce and maintain the high state of ionization in these systems. Hence, the primary utility of O VI may

not be for measuring the total content of the warm-hot intergalactic medium, or tracing the metal content of the lowest density regions of the forest, but rather for probing physics at the interface between galaxies and the IGM. This connection has been suggested by the association of galaxy groups and O VI absorption at low redshift (Savage et al., 2002); an analogous connection at high redshift could aid in the characterization of processes thought to have significant impact on the thermal and chemical history of the IGM.

Chapter 3

The Distribution of Metallicity in the IGM at $z \sim 2.5$ [1]

3.1 Introduction

Observations of C IV absorption in QSO spectra have unambiguously revealed the presence of heavy elements in the Ly-α forest at $z = 3$ (Meyer & York, 1987a; Cowie et al., 1995a; Ellison et al., 2000; Cowie et al., 1995b; Rauch et al., 1997b, 1996b). These results have been interpreted as evidence of widespread enrichment of the universe with the byproducts of stellar nucleosynthesis, but the data at present permit the possibility of several enrichment mechanisms, from an early ($z > 10$) generation of massive short-lived stars (e.g., Ostriker & Gnedin, 1996) to more recent ($z < 7$) pollution by winds from star forming galaxies (Adelberger et al., 2003; Aguirre et al., 2001; Springel & Hernquist, 2003). Measurements of the IGM metallicity can usefully constrain the history of star formation and stellar recycling on cosmological scales. However, at a limiting associated H I column of $\sim 10^{14.5}$ cm^{-2}, existing C IV measurements only probe regions with gas overdensities of $\rho/\bar{\rho} \geq 7$ relative to the cosmic mean. This corresponds to the densest $\sim 15\%$ of the baryons in the Ly-α forest, which occupy $\lesssim 1\%$ of the total volume of the universe.

At H I column densities below $10^{14.5}$ cm^{-2}, C IV searches are limited by signal-to-noise ratio even in the best available spectra. A decline in the overall carbon column in low density gas is exacerbated by the increasing ionization state of the gas, which favors C V and higher levels in the more tenuous regions of the IGM. To combat this effect, several studies have employed sensitive statistical techniques to extract averaged estimates of [C/H] at lower densities. These studies generally fall into two categories: either a shift-and-stack approach to generate a high signal-to-noise, composite C IV line (Lu et al., 1998), or a pixel-by-pixel statisical analysis of the relative optical depths of H I and C IV throughout the run of a spectrum (Cowie & Songaila, 1998; Songaila & Cowie, 1996; Ellison et al., 2000; Aguirre et al., 2002). The reader is referred to Ellison et al. (2000)

[1] Reprinted from the *Astrophysical Journal*, V. 606, p. 92 (Copyright 2004, The American Astronomical Society).

for a review of these two methods. Over time, pixel methods have seen more extensive use, although they can be difficult or impossible to interpret without recourse to simulations, and our experience has shown that they are extremely sensitive to slight systematics (e.g. continuum placement).

In this work, we descibe a new effort to pursue metallicity measurements in the IGM to near the cosmic mean density through observations of weak O VI absorption in a sample of 7 QSOs. This is supported by new observations of C IV absorption in high signal to noise spectra of two sample objects. We have limited our measurements to a single observed quantity: the column density of detected O VI and C IV lines (or 3σ upper limit on $N_{\rm O\ VI}, N_{\rm C\ IV}$ for non-detections). This paper therefore represents our best effort to describe the enrichment of the IGM using the direct, local properties of individual systems. This approach accepts a slight sacrifice in sensitivity over the more statistical methods quoted above, in return for a localized description of the metallicity field and a straightforward assessment of possible systematic biases. It also allows for an easy division of the total sample into subsets to study trends of metallicity with other external variants, such as H I column density, or proximity to galaxies (though the latter is beyond the scope of this paper).

The literature contains several examples of intergalactic O VI searches, as it has long been known that its ionization potential and high abundance are very favorable for production in the low density IGM [2]. The principal hurdle faced by these searches is the unfortunate rest wavelength of the O VI doublet ($1032, 1037\mathring{A}$). This locates the weak O VI lines deep in the Ly-α forest, which smothers the signal of many real systems and further introduces a number of false positive identifications. Many of the O VI systems discovered in these surveys display large equivalent widths and rich chemical structure, such as would be expected in galactic environments (Burles & Tytler, 1996; Simcoe et al., 2002). Using a single spectrum of Q1422+2309, Davé et al. (1998) statistically explored the O VI content of the low density IGM at $z \sim 3.5$, and more recently Carswell et al. (2002) have discovered evidence for O VI enrichment in a number of individual systems with $N_{\rm H\ I} \sim 10^{14.5}$ at $z \sim 2.3$.

This paper expands upon these studies using an increased number of sightlines observed at high resolution, and also by incorporating the full use of non-detections in the analysis. These additional measurements have allowed us to use the methods of survival analysis to construct the distribution function of [O/H] and [C/H] in the Ly-α forest. In Section 3.2 we describe the observations, sample definition, and measurement methods; Section 3.3 explains the conversion of column density measurements to abundance estimates and the application of survival statistics to estimate the [O/H] distribution; and Section 3.4 discusses the cosmological implications of the observed metallicity

[2]It should be noted that searches for metals in the high redshift Ly-α forest are qualitatively different from the recent low redshift O VI surveys undertaken with FUSE and STIS (Tripp & Savage, 2000; Tripp et al., 2001; Savage et al., 2002). The local, "warm-hot" variety of O VI is usually collisionally ionized through interactions with galaxies, or by accretion shocks as pre-enriched material falls onto large scale structure. The weak, high redshift systems represent much cooler gas that is photoionized by the integrated light from quasars. They are physically distinct from the "warm-hot" phase of the IGM (Davé et al., 2001).

Table 3.1. Quasars Observed for Weak O VI Systems

Object	z_{em}	Δz_{OVI}[1]
Q1009+2956	2.62	2.295-2.553
Q1217+4957	2.70	2.374-2.635
Q1347-2457	2.53	2.329-2.525
Q1442+2931	2.63	2.270-2.556[2]
Q1549+1919	2.83	2.273-2.767
Q1603+3820	2.51	2.201-2.415[3]
Q1700+6416	2.72	2.259-2.651

[1]Corrected to exclude regions within 5000 km/s of the QSO emission redshift.

[2]The region $2.41 < z < 2.46$ was excluded for this object due to the presence of a weak Damped Ly-α system in this wavelength range.

[3]The region $2.415 < z < 2.450$ was excluded for this object due to the presence of a strong system which appears to be ejected from the QSO.

distribution.

3.2 Observations

Our search targets 7 bright QSOs in the redshift range $2.5 < z < 2.8$, which was chosen to balance three important factors regarding the existence and observability of O VI: contamination from the Ly-α forest (which worsens toward higher redshift), strength of the metagalactic UV ionizing flux (which is maximized at $2.5 < z < 3.0$), and accesibility from large aperture, ground-based telescopes (to improve S/N for the weakest lines). The sightlines are listed in Table 3.1, along with their QSO emission redshifts and the range of redshift covered by the absorption line measurements. Four of the seven spectra were used in our earlier analysis of strong O VI systems (Simcoe et al., 2002), and the details of those observations are found therein. New observations of Q1217+4957, Q1347-2457, and Q1603+3820 were taken in April 2002 under variable conditions; Q1626+6433 was used in the previous paper but is omitted here because of the data's lower signal to noise ratio and small redshift coverage. The observations were taken with the HIRES spectrograph on the Keck I telescope, using the UV blazed cross disperser. All exposures were taken through an $0.86''$ slit fixed at the parallactic angle, for a spectral resolution of 6.6 km s^{-1}, and the data were processed using T. Barlow's "makee" echelle reduction package.

3.2.1 Identification and Measurement of the O VI Systems

Because of the placement of O VI within the Ly-α ,Ly-β , and higher-order Lyman forests, our first step has been to follow the procedure of Carswell et al. (2002), fitting the entire Ly-α forest region to remove high order H I transitions from the data. Beginning at the emission redshift of the quasar, each H I line in the forest was fit with a combination of Voigt profiles using the VPFIT [3] software package. This procedure was extended to lower redshift until the observed wavelength of Ly-α was equal to the observed wavelength of O VI at the emission redshift of the QSO. For the handful of cases in each spectrum with $N_{\rm H\ I} > 10^{15}$ (where H I lies on the flat part of the curve of growth) we performed joint fits for the H I column density using Ly-α ,Ly-β ,Ly-γ , and Ly-δ . In all other cases, only Ly-α was used, as the primary goal was to remove these higher order lines. As a side benefit, we obtain a full statistical description of the forest in the redshift range of the O VI survey. This information is used in Section 3.7 to estimate the mass fraction of baryons probed in the sample.

Once a satisfactory fit was obtained for the forest, we adjusted the original data and error arrays, using the model fit to remove the signal of Ly-β and higher order Lyman series transitions. Even small fluctuations around the continuum level were often caused by Ly-γ to Ly-7 transitions from higher redshift systems. By removing this signal the useful O VI pathlength in each spectrum is nearly doubled, correspondingly doubling the size of our line sample.

3.2.1.1 O VI Sample Selection and Measurements

For the O VI measurements, we have focused on the subset of systems with H I column densities above $N_{\rm H\ I} = 10^{13.6}$ cm^{-2}. This represents almost an order of magnitude increase in H I depth over past C IV and O VI surveys, and corresponds to clouds with overdensities of $\rho/\bar{\rho} \sim 1.6$ relative to the cosmic mean at $z \sim 2.5$. The quality of the O VI data varies throughout the survey according to sightline and redshift, and not all regions are sufficiently sensitive to reveal O VI lines at the level expected for the weakest H I systems in the sample. However, in some regions the data quality is very high, and we shall describe below how measurements from the best regions can be combined consistently with upper limits measured in portions of the spectrum with lower signal-to-noise ratios.

We selected candidate systems using H I column densities obtained from our Voigt profile fits to the Ly-α forest. For each line in the $N_{\rm H\ I} \geq 10^{13.6}$ sample, we examined the spectrum (now free of higher order H I lines) for O VI at each sample redshift. In instances where a possible O VI line was detected at $\geq 3\sigma$ significance, we used VPFIT to determine the column density and b parameter of the O VI line. At this stage, systems were flagged as possible detections if both components of the O VI doublet were clearly visible, or if absorption was present in one component but the other was strongly blended with a Ly-α forest line. If no O VI absorption was present at the expected location of one or both doublet components, we determined 3σ upper limits on the O VI absorbing column.

[3] Provided by R. Carswell, J. Webb, A. Cooke, & M. Irwin - http://www.ast.cam.ac.uk/∼rfc/vpfit.html

The upper limits were measured from the O VI 1032Å transition except in cases where Ly-α forest blending led to a cleaner result from O VI 1037Å.

When no O VI is detected, the measurement of an upper limit on $N_{\rm O\ VI}$ depends upon the choice of linewidth, b, which cannot be determined from the data. Rather than guessing at the correct value to use, we have measured two upper limits for each system. For one measurement, we fix $b_{\rm O\ VI}$ to the value for completely thermal line broadening in the H I -O VI gas mixture: $b_{\rm O\ VI} = b_{\rm H\ I} \times \sqrt{m_{\rm H\ I}/m_{\rm O\ VI}}$. The other limit correponds to broadening from turbulent or bulk gas flows: $b_{\rm O\ VI} = b_{\rm H\ I}$. The actual value should lie between these two extremes. We also fix $z_{\rm O\ VI} = z_{\rm H\ I}$ for measuring limits on non-detections; for detections we allow the redshift to vary up to ~ 40 km s^{-1} to optimize the fit. Often velocity differences are observed between $z_{\rm H\ I}$, $z_{\rm O\ VI}$, and $z_{\rm C\ IV}$ in strong systems. However, for our non-detections the upper limits are not strongly sensitive to the exact placement of $z_{\rm O\ VI}$, as the noise properties of the data tend to be fairly uniform over the ~ 20 km s^{-1} velocity offsets sometimes observed between different ions. All quoted upper limits are at the 3σ level when no line could be fit. In cases where VPFIT was able to fit a line with N_{vp} at $\leq 3\sigma$ significance, we quote an upper limit of $N_{\rm O\ VI} \leq N_{vp} + 3\sigma$. Regions where VPFIT found absorption at the 3σ level or greater are reported as detections with the best fit column density.

In most of our systems, one component of the O VI doublet is blended with a Ly-α forest line. If the other transition is clean of blends and shows no O VI its interpretation as a non-detection is secure. This situtation is fairly common, and we denote it as a *bn* system, for "blend/non-detection". But often one transition is blended with a forest line while the other shows weak absorption that could be either O VI or another interloping Ly-α line. These systems, hereafter called the *bd* sample ("blend-detection"), comprise a potentially serious source of false positive O VI identifications. A conservative approach is to treat all *bd*s as upper limits due to their unsure identification. However, if we assign upper limits to all *bn*s *and bd*s we would downweight many true detections and bias our results toward low metallicities. Yet if we were to restrict our sample to those systems where both components of the doublet are completely free of blending (accordingly, the *dd* detections and *nn* nondetections) the sample would be too small to provide physically interesting constraints on the metallicity of the IGM. At the measurement stage, our approach has been to treat all *bn* and *nn* systems as upper limits, and all *bd* and *dd* systems as detections for completeness. Later in the analysis, we use Monte Carlo simulations to estimate the degree of contamination from false positives in the *bd* subsample, and correct for their effects statistically.

3.2.2 Identification and Measurement of the C IV Systems

For two of the objects in the sample, we have obtained particularly high quality spectra to search for extremely weak C IV absorption features. Our intent is to compare the distribution of [C/H] with that of [O/H], both to check for consistency and to test the accuracy of the ionization corrections that

we will use to estimate metallicities. By far the best spectrum in the sample is that of Q1549+1919, with an average signal to noise ratio of ~ 350 per resolution element throughout the C IV region. We also analyze the C IV absorption in Q1700+6416, whose spectrum has $S/N \sim 175$ per resolution element. While the second spectrum is not as sensitive for measuring the weakest C IV lines, we have included it to increase the C IV pathlength and improve the statistics of stronger absorbers.

As before, we use Voigt profile fits to the Ly-α forest to determine the subset of lines to be examined for C IV absorption. However, even with such high quality data the predicted C IV strength drops so precipitously with $N_{\rm H\ I}$ that we cannot probe overdensities as low as with O VI. Therefore, we limit the C IV sample to systems with H I column densities above $N_{\rm H\ I} = 10^{14.0}$ cm^{-2}. Because the same objects were observed for O VI, we were able to fit across the Lyman series for saturated H I lines so the H I columns are very accurately known. At each sample redshift, we examine the location of the C IV 1548.202Å line and measure its strength if a detection is made. If no feature is present, we determine a 3σ upper limit on the C IV column density for both the thermal and turbulent broadening cases. For nearly all of the systems, we used the 1548.202Å component to measure upper limits. In the unusual case where this line was blended with a line from another redshift system, we used the 1550.774Å component to measure the limits.

3.2.3 Distribution in the H I /O VI and H I /C IV Planes

We have measured O VI and H I column densities for a total of 232 Ly-α forest lines with $N_{\rm H\ I} \geq 10^{13.6}$ cm^{-2} in 7 sightlines, and C IV and H I column densities for a total of 83 systems with $N_{\rm H\ I} \geq 10^{14.0}$ cm^{-2} in two sightlines. These data are summarized in Figure 3.1, where we plot measurements or 3σ upper limits for each O VI and C IV line against its H I column density. The upper limits shown in the plots are for the thermal line broadening case.

In the O VI figure, we have subdivided the detected systems according to our confidence in their identification. Heavy round points denote highly probable O VI, where both components of the doublet are seen in the proper ratio of strengths (the *dd* sample). Smaller squares are used for the *bd* sample, where only one of the two doublet components could be measured due to Ly-α forest blending with the other line. Again, we stress that this subsample contains spurious measurements from interloping H I lines - in Section 3.5 we estimate that only $\sim 40\%$ of these points are actually O VI. In these cases the measurements still provide upper limits on the O VI column density, so in truth some $\sim 60\%$ of the square points would be replaced with upper limit symbols. The C IV sample does not suffer from this sort of contamination, and all detections are weighted equally.

The solid curve in each panel indicates the locus of points predicted for Ly-α forest clouds enriched to [O/H]=[C/H]=-2.5, and illuminated by a slightly modified version of the Haardt and Madau (1996) ionizing background spectrum (see Sections 3.1 and 3.2 for a description of how these model predictions are generated). Our observations have reached the sensitivity required to detect

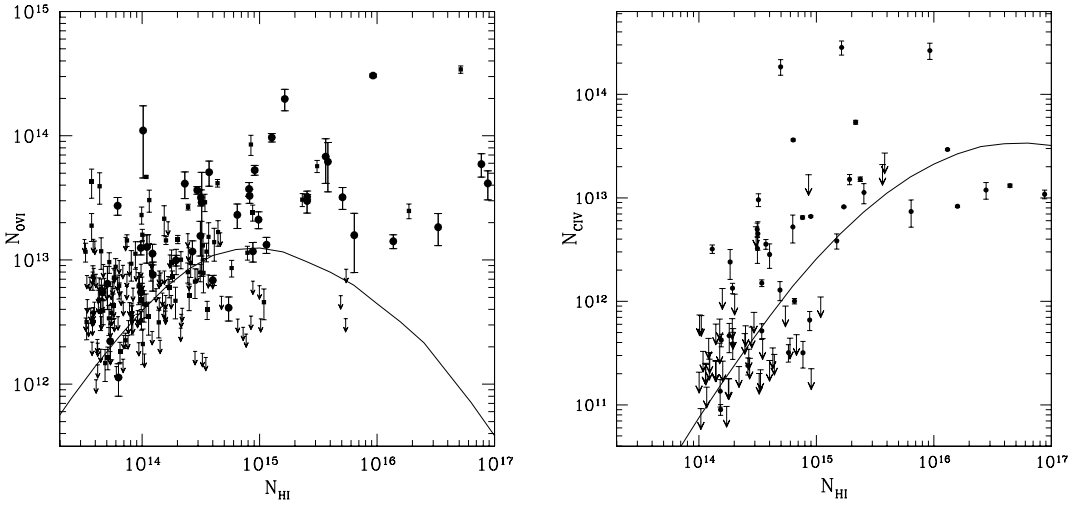

Figure 3.1 Scatter plot of detections and upper limits in the $N_{\rm H\ I}/N_{\rm O\ VI}$ and $N_{\rm H\ I}/N_{\rm C\ IV}$ planes. For O VI, the solid round points with errors represent the *dd* variety of O VI detections, and small squares represent *bd* detections. Arrows indicate 3σ upper limits for undetected lines assuming thermal broadening. The solid line drawn through the data represents the expected locus of points for a mean $[O/H] = -2.5$ and the HM1.80 UV background.

metal lines at this commonly quoted abundance level for much of the sample. Even at $N_{\rm H\ I} < 10^{14.0}$, some of our O VI measurements are able to meaningfully probe the metal distribution, although the presence of several upper limits above the model curve indicate the increasing challenge at the lowest $N_{\rm H\ I}$.

Generally, the O VI and C IV data points follow the trends traced by the model predictions, with a few exceptions. At high column densities (about $N_{\rm H\ I} > 2\times10^{15}$) most H I systems appear to contain O VI, but the O VI is often significantly stronger than the model prediction. This discrepancy is not surprising, and could be due to several factors. First, the recipe for producing the model curve assumes a scaling between physical gas density and H I column which may break down at higher densities where cosmic structure becomes nonlinear. More importantly, the models calculate metal strengths assuming a pure photoionization equilibrium, whereas the strongest systems may be collisionally dominated. Finally, the dense systems are likely sites of local chemical enrichment so their metallicity could be higher by an order of magnitude or more.

At lower $N_{\rm H\ I}$ there are several systems with exceptionally *low* metal to H I ratios, for both C IV and O VI. In some cases these lie almost an order of magnitude below the model prediction, even though the model should be most accurate in this regime. The presence of several such systems was initially a puzzle as we expected to find O VI and C IV absorption throughout the IGM. It is not obvious from Figure 3.1 whether these outlying systems are consistent with simple scatter about a trend, or whether they represent a different population of lines that is statistically distinct from the rest of the sample. This question will be addressed in detail below as we construct a quantitative

distribution function of the intergalactic metallicity field.

3.3 Analysis

Having fit O VI and C IV line strengths for the H I selected systems, we now translate these measurements into metallicity estimates for each line in the sample. In the following sections we describe the methods used to build the metallicity distribution using survival statistics, including corrections for false positive O VI identifications.

3.3.1 Estimating [O/H], [C/H] for Ly-α Forest Lines

Using measurements of O VI and H I , the oxygen abundance for a single system is calculated as

$$\left[\frac{O}{H}\right] = \log\left(\frac{N_{\rm O\ VI}}{N_{\rm H\ I}}\right) + \log\left(\frac{f_{\rm H\ I}}{f_{\rm O\ VI}}\right) - \log\left(\frac{O}{H}\right)_{\odot}, \tag{3.1}$$

where $f_{\rm O\ VI} = n_{\rm O\ VI}/n_{\rm O}$ and $f_{\rm H\ I} = n_{\rm H\ I}/n_{\rm H}$ are ionization fractions and we have assumed solar relative elemental abundances. Throughout, we use the meteoritic solar abundances of Grevesse and Sauval (1998), with $A_{\rm oxygen} = 8.83$ and $A_{\rm carbon} = 8.52$ on a scale where $A_{\rm hydrogen} = 12$. Clearly the same method may be applied to calculate [C/H] from our C IV line sample. Also, the equation may be inverted to predict $N_{\rm O\ VI}$ for different values of $N_{\rm H\ I}$ if [O/H] is already known (this is the method used to produce the model curves in Figure 3.1).

3.3.2 Modeling Intergalactic Ionization Conditions

The principal challenge of our metallicity calculation is an accurate estimation the ionization correction term in Equation 3.1. We have run simulations of the ionization conditions in the IGM to calculate this term as a function of H I column density for each line in the sample.

In the low density Ly-α forest, there exists a tight correlation between physical gas density and observed H I column density (Zhang et al., 1995; Davé et al., 1999; Schaye, 2001). We can use this relation to translate each H I column density in the sample into a physical density, inverting Equation 8 of Schaye (2001):

$$n_{\rm H} \approx 10^{-5}{\rm cm}^{-3}\left(\frac{N_{\rm H\ I}}{2.3\times10^{13}{\rm cm}^{-2}}\right)^{\frac{2}{3}} \times T_4^{0.17}\Gamma_{12}^{\frac{2}{3}}\left(\frac{f_g}{0.16}\right)^{-\frac{1}{3}}. \tag{3.2}$$

The last three factors represent scaling corrections for the gas temperature, ionizing background, and fractional mass in diffuse gas, and are likely to be of order unity as argued by Schaye. This relation was derived assuming that the local collapse of Ly-α forest clouds occurs nearly in hydrostatic equilibrium. This may break down at high H I column densities where structures become nonlinear,

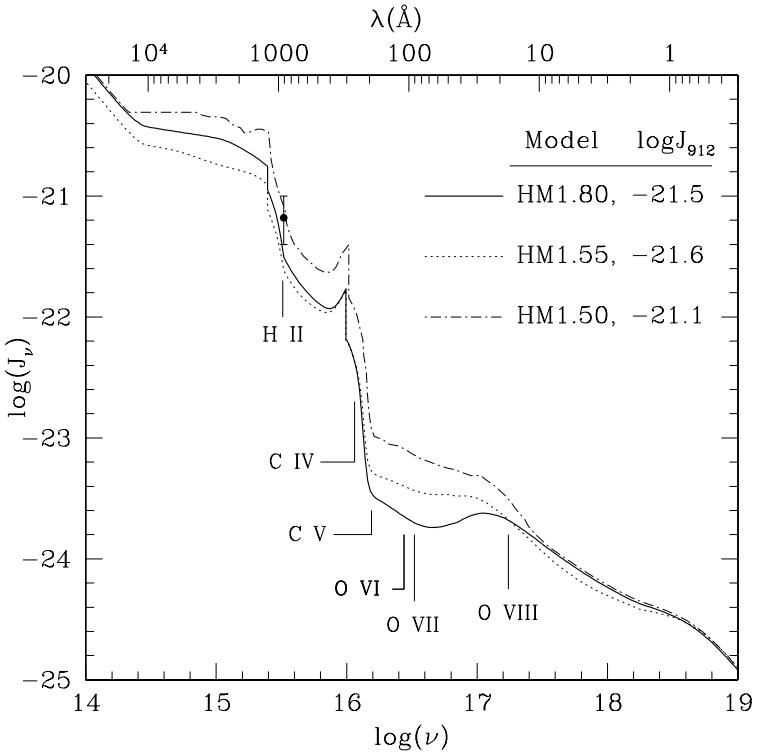

Figure 3.2 Three representative models of the UV/X-Ray background used in the analysis. The solid line represents our favored HM1.80 model. The ionization edges for several important transitions are labeled, with the convention that the "O VI " label marks the wavelength associated with the ionization of O V to O VI. The point with errorbars represents the Scott et al. (2000) estimate of $\log J_{912}$ from the proximity effect.

though numerical simulations indicate that the scaling remains accurate at least to $N_{\rm H\,I} \lesssim 10^{16}$ (Davé et al., 1999).

The intergalactic gas is highly ionized by ambient ultraviolet/X-Ray radiation, whose spectrum at $z \sim 2.5$ is dominated by quasar light that is reprocessed by radiative transfer through the IGM. We have run sets of ionization calculations for several different forms of the ionizing background spectrum, which were computed as described in Haardt and Madau (1996) and kindly provided to us by F. Haardt. A range of these spectra is shown in Figure 3.2; details about their construction are provided in Appendix A. The curves differ both in their normalization, and in their underlying UV spectral slope. The discrepancies reflect uncertainty in the exact shape of the source function in the radiative transfer equations - i.e., the average UV spectral slope intrinsic to QSOs. All of the models assume that quasar spectra in the UV are pure power laws: $F_\nu \propto \nu^{-\alpha}$. Intergalactic H I and He II absorption and reemission modulate this raw spectrum, producing the features seen in the $10 - 1000$Å range of Figure 3.2. We have named the models according to their input spectral slope, so that the HM1.80 model represents a spectrum with an input $\alpha = 1.8$ power law that has been propegated through the IGM. The overall normalizations of the spectra are specified at 912Å (1 Ry)

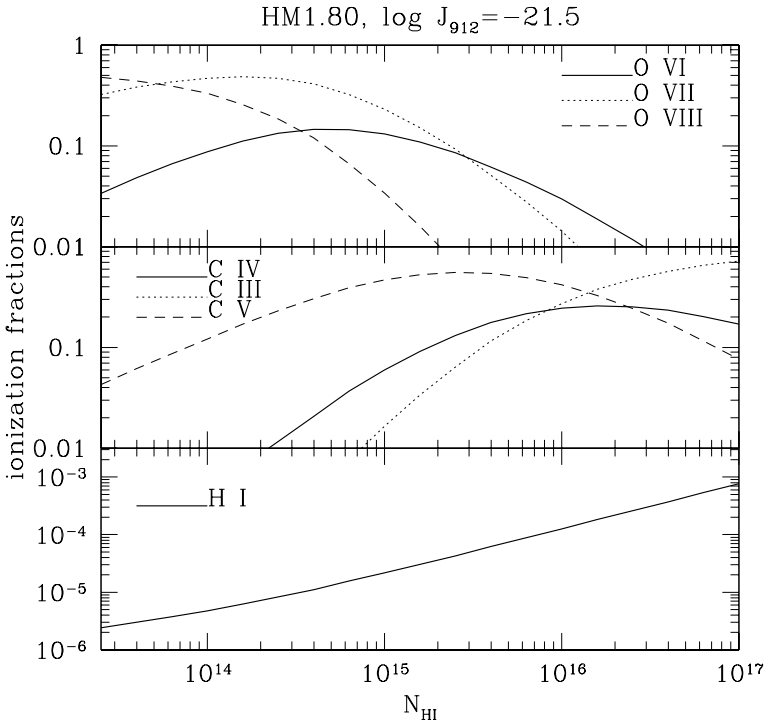

Figure 3.3 The ionization balances of several carbon and oxygen transitions relevant to C IV and O VI production, as a function of H I column density.

as indicated in the plot.

Recent attempts to measure α by averaging quasar spectra have produced varied estimates in the range $1.5 < \alpha < 1.8$. The original Haardt and Madau (1996) paper used an $\alpha = 1.5$ model, resulting in the curve labeled as HM1.50 in the plot. Subsequently, Zheng et al. (1997) published a revised estimate of $\alpha = 1.8$, based on FOS observations of 101 quasars. The most recent determination of the UV slope (Telfer et al., 2002, 184 QSOs) revises the value again to $\alpha = 1.57$, but raises the possibility of strong variations from object to object. Each of these papers used the entire sample of FOS quasar spectra in the HST archive at the time of its publication. The samples are therefore not uniformly chosen, and could be subject to selection effects. We have tested each of the different models; for consistency below we adopt the HM1.80 spectrum normalized to $J_{912} = -21.5$ (solid line in Figure 3.2) as our fiducial X-Ray/UV background. In this model, 95% of the helium in the universe has been ionized to He III by $z = 2.5$. Most of the remaining 5% is in He II , leading to $\tau_{\rm He\ II} \sim 1$. We shall show that the HM1.80 model results in the best match between the intergalactic distributions of [O/H] and [C/H]. It is also roughly consistent with observations of the proximity effect and X-Ray background at similar redshifts (Scott et al., 2000; Boyle et al., 1993).

Using these input spectra, we simulate the ionization balance of the IGM over a range of densities using the CLOUDY software package (Ferland et al., 1998). We treat the absorbing material as a

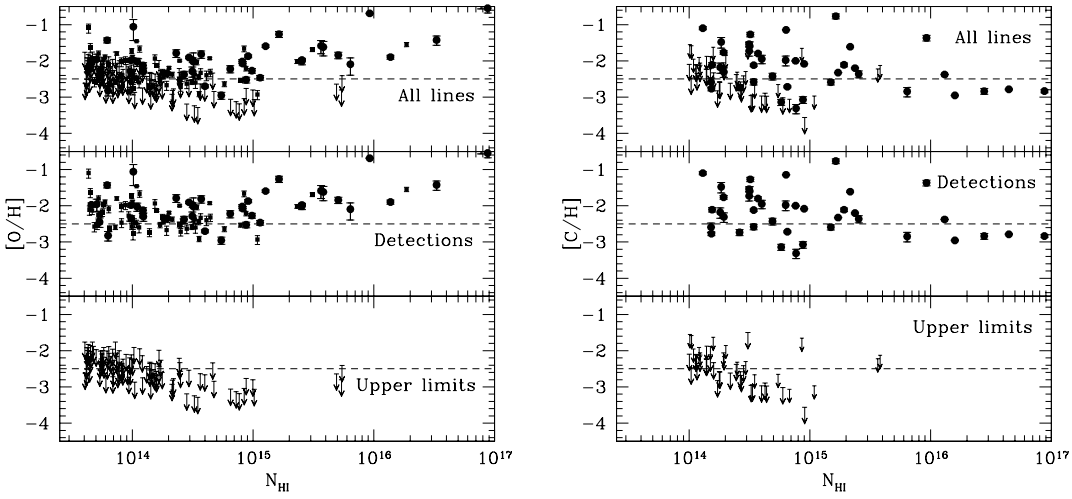

Figure 3.4 Scatter plot of individual metlalicity measurements for all O VI lines in the $N_{\rm H\,I} > 10^{13.6}$ sample. In the bottom two panels the detections and non-detections are shown separately for clarity. The dotted line drawn at [O/H]=-2.5 is not a fit to the data. The O VI detections exhibit a fairly constant metallicity with decreasing density. The slanted trend in the upper limits is purely due to the detection threshold of the data. In the most sensitive region between $10^{14} < N_{\rm H\,I} < 10^{15}$, there is more scatter in the upper limits toward low metallicity, revealing the presence of a population of low metallicity systems.

plane-parallel gas slab, and CLOUDY calculates the ionization balance for each element, from which we extract the ionization fractions $f_{\rm O\,VI}$, $f_{\rm C\,IV}$, and $f_{\rm H\,I}$. These are combined to calculate the second term in Equation 3.1 along a grid of H I points. The exact ionization correction for each absorption line in the sample is then obtained by interpolating its H I column within the grid, and we combine these with the $N_{\rm O\,VI}, N_{\rm C\,IV}$, and $N_{\rm H\,I}$ measurements from the data to calculate a value or 3σ upper limit for [O/H] or [C/H].

3.3.3 Metallicites of Individual Lines, and Trends with $N_{\rm H\,I}$

In Figure 3.4, we show the metallicity or its upper limit for each line in the O VI and C IV samples, plotted against H I column density. In this plot and those that follow, we have assumed the HM1.80, $\log J_{912} = -21.5$ fiducial spectrum for the UV background. The top panel includes all lines in each sample, and in the bottom two panels we have plotted detections and non-detections separately for viewing clarity. The dashed horizontal lines are drawn at an abundance of $[O/H] = -2.5$ to guide the eye, and are not fits to the data.

Looking first at the detections, we see that over a broad range in H I density there is little change in the average metal abundance. At the highest densities there is a clear trend toward increasing metallicity in the O VI sample, with no corresponding change in the C IV distribution. As discussed above, this could be caused by local enrichment, but is also likely due in part to model errors.

In particular, at high densities ($N_{\rm H\ I} \gtrsim 10^{15.5}$) many of the systems will be multiphase absorbers with hot collisionally ionized O VI and cooler, photoionized C IV (Simcoe et al., 2002). Thus at these densities the O VI and C IV might not be expected to follow each other too closely, and our photoionization models may break down. Nonetheless, at lower densities where the models are most accurate and where most of the lines are found, the metallicities of the detected systems are fairly uniform. To the limits of the survey ($\rho/\bar{\rho} \sim 1.6$) *we have detected no strong trend of decreasing metallicity toward the more tenuous regions of the IGM.*

This statement is based only upon the detected systems; the upper limits in the bottom panel reveal a different central result: that *a number of systems have metallicities significantly below the trend outlined by the detected systems.* This is most easily seen in the $10^{14.5} < N_{\rm H\ I} < 10^{15.0}$ range where our measurements can best sample the scatter both above and below the mean. In this regime most of the detected points fall near $[O/H] \sim -2.5$, but there are many non-detections whose 3σ upper limits are an order of magnitude lower, with little or no corresponding scatter at high metallicity (this is perhaps best seen in the top left panel of Figure 3.4). This pattern is likely to continue at lower densities, though we cannot test this hypothesis with the present data due to its limited signal-to-noise ratio (seen as a decrease in the sensitivity of the upper limits at low $N_{\rm H\ I}$).

In Figure 3.5 we show a collection of four low metallicity systems, to give a sense of the data quality used for our measurements. In each case, the H I profile is shown at bottom, along with the C IV 1549Å transition and one or both components of O VI. We also show with smooth curves the predicted strength of the metal absorption features for [O/H]=[C/H]=-2.5 and our fiducial HM1.80 ionizing background spectrum. Two model curves are shown; the narrower assumes thermal line broadening and the wider assumes pure turbulence. In each of these systems C IV should be marginally detectable, and O VI would have been clearly seen for thermal broadening and is sometimes visible for turbulent broadening as well.

The qualitative results of this section are not strongly sensitive to the choice of ionizing background spectrum, though there are some slight differences between the models. The harder HM1.50 UV background leads to a slightly lower average metallicity for the detected systems (by 0.1-0.2 dex), but there is still no positive or negative trend of metallicity with H I column density. The metallicity-density relation is affected by the strength of the soft X-ray background, in the sense that fewer X rays would introduce a correlation of decreasing metallicity with decreasing density (See Appendix C for a more detailed discussion of this effect). The upper limits on [O/H] for the lowest metallicity systems are not affected by changes in the X-ray background, but harder UV spectra can reduce these limits from $[O/H] \leq -3.15$ to $[O/H] \leq -3.4$

In physical terms, the H I densities probed by the survey extend roughly to the boundary between the filaments and voids seen in cosmological simulations. Within the filaments, where most baryons are found, the enrichment pattern does not appear to vary with overdensity. If strong overall

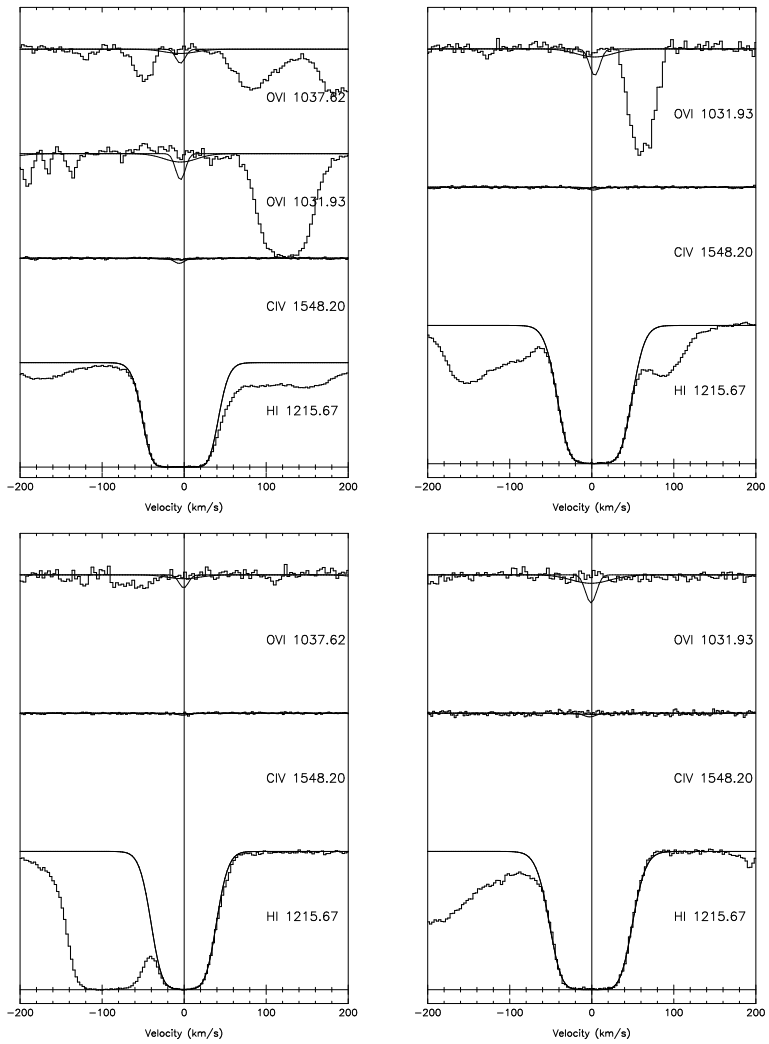

Figure 3.5 A montage of low metallicity systems. The H I Ly-α transition is shown in the bottom of each panel, along with the C IV 1548Å transition and one or both O VI transitions. The continuous curves show the predicted strength of O VI and C IV if [O/H]=[C/H]=-2.5. The narrow profile represents thermal broadening, and the broad profile represents turbulent broadening.

metallicity gradients do exist in the IGM, they must occur as the transition is made into the voids which fill most of the cosmic volume. In the moderate density regions where our O VI measurements are most sensitive, we detect significant numbers of metal-poor forest lines ($[O/H] \leq -3.2$), and we hypothesize that analogous low metallicity systems are likely to exist at lower densities. In the subsequent sections, we use the individual measurements and upper limits to better quantify the relative frequency of the enriched versus metal-poor systems in our sample.

3.3.4 Survival Analysis

To translate the measurements of individual lines into a statistical distribution of metallicity, a proper accounting must be made both of detections and of nondetections in the total sample. This problem is well suited to the methods of survival analysis, a branch of statistics that deals with "censored" datasets, which contain mixtures of measurements and upper limits.

The most general single variate survival statistic is the Kaplan-Meier product limit, which provides a non-parametric maximum likelihood estimate of a distribution directly from observed data. The Kaplan-Meier statistic and other survival methods have been discussed extensively in the astronomical literature (e.g., Feigelson & Nelson, 1985; Schmitt, 1985; Wardle & Knapp, 1986). We follow these examples, modifying notation slightly to suit our particular application. We shall use the term "measurement" to describe the combined set of detections plus upper limits; "detection" and "upper limit" will be used when the specific context requires. We also use the notation $Z_{\rm true}$ to represent the actual metallicity of a line, so that for detections $Z_{\rm true} = Z_i$, while for upper limits its value is unknown beyond that $Z_{\rm true} < Z_i$.

Consider a sample of lines for which a single variate - the metallicity Z - has either been detected or an upper limit has been determined. We assume that the total set of measurements $Z_i, i = 1, 2, 3...N$ has been sorted in order of increasing metallicity such that every $Z_i \leq Z_{i+1}$ (where multiple measurements result in the same value, censored data points are considered smaller). We wish to use this sample to estimate the cumulative probability distribution $P(Z \geq Z_i)$: the fraction of Ly-α forest lines above any given metallicity threshold.

We begin at the maximum of the distribution, since for all $Z^+ > Z_N$, every measurement in the sample is at lower metallicity, hence we estimate $P(Z < Z^+) = 1$. According to standard convention, then

$$P(Z \geq Z^+) = 1 - P(Z < Z^+) = 0. \tag{3.3}$$

Subsequent values of $P(Z \geq Z_i)$ at are constructed at each i by stepping downwards from the Nth measurement using the rules of conditional probability. As the first such example, we calculate

$P(Z \geq Z_N)$:

$$\begin{aligned} P(Z \geq Z_N) &= 1 - P(Z < Z_N) \\ &= 1 - P_{[Z<Z_N|Z<Z^+]} \cdot P(Z < Z^+) \\ &= 1 - P_{[Z<Z_N|Z<Z^+]} \end{aligned} \tag{3.4}$$

where $P_{[Z<Z_N|Z<Z^+]}$ denotes the conditional probability that $Z < Z_N$ given that $Z < Z^+$. It follows that $P(Z \geq Z_{N-1})$ becomes

$$P(Z \geq Z_{N-1}) = 1 - P_{[Z<Z_{N-1}|Z<Z_N]} \cdot P_{[Z<Z_N|Z<Z^+]} \cdot P(Z < Z^+), \tag{3.5}$$

or for arbitrary i,

$$P(Z \geq Z_i) = 1 - \prod_{j=i}^{N} P_{[Z<Z_j|Z<Z_{j+1}]}. \tag{3.6}$$

The conditional probabilities are estimated by counting measurements from the ranked sample as follows. For illustration, we first assume all data points in the sample are detections (i.e. no upper limits). In this event the conditional probability at each j would be

$$\begin{aligned} P_{[Z<Z_j|Z<Z_{j+1}]} &= \frac{\#\text{ detections with } Z < Z_j}{\#\text{ detections with } Z < Z_{j+1}} \\ &= \frac{n_{(Z<Z_{j+1})} - n_{(Z=Z_j)}}{n_{(Z<Z_{j+1})}} \qquad (\textit{no upper limits}). \end{aligned} \tag{3.7}$$

In a sample containing upper limits, the quantities $n_{(Z<Z_{j+1})}$ and $n_{(Z=Z_j)}$ are not uniquely known, since an upper limit Z_k measured at $k \geq j+1$ could have a true metallicity $Z_{k,\text{true}} \geq Z_{j+1} > Z_j$, or $Z_j < Z_{k,\text{true}} \leq Z_{j+1}$, or $Z_{k,\text{true}} < Z_j < Z_{j+1}$. In other words, an upper limit Z_k with $k > j$ does not provide useful information about the relative weights $n_{(Z<Z_{j+1})}$ and $n_{(Z=Z_j)}$ because the relation between $Z_{k,\text{true}}$, Z_j and Z_{j+1} is ambiguous. The Kaplan-Meier method circumvents this ambiguity by effectively ignoring upper limits with $k \geq j+1$ in constructing $P_{[Z<Z_j|Z<Z_{j+1}]}$, but retaining the useful information from upper limits with $k \leq j$. Accordingly, the conditional probability is expressed as

$$P_{[Z<Z_j|Z<Z_{j+1}]} = \frac{\#\text{ measurements which } \textit{must} \text{ have } Z_{\text{true}} < Z_j}{j}. \tag{3.8}$$

In practice, this probability can take on one of two values, depending on whether Z_j is a detection or an upper limit. If Z_j is an upper limit, then all of the lines up to *and including* line j must have true metallicities less than Z_j, hence $P_{[Z<Z_j|Z<Z_{j+1}]} = j/j = 1$. If Z_j is a detection, then the

conditional probability resembles Equation 3.8:

$$P_{[Z<Z_j|Z<Z_{j+1}]} = \begin{cases} 1 & Z_j = \text{upper limit} \\ \frac{j-n_{(Z=Z_j)}}{j} & Z_j = \text{detection} \end{cases} \tag{3.9}$$

Thus the Kaplan-Meier product limit estimate of $P(Z \geq Z_i)$, specified by Equations 3.6 and 3.9, is a piecewise step function, which jumps at the Z values of detections and remains constant through upper limits.

For the Kaplan-Meier estimator to be valid, two assumptions about the distribution of upper limits must be satisfied. First, the upper limits must be independent of one another. In our case, this is clearly true when upper limits are measured for lines that are not blends of two O VI or C IV components. This applies to virtually the entire sample (In some cases, detections are measured in regions with blends, but never upper limits). Second, the probability that a measurement will be censored should not correlate with the measurement value itself (i.e. the censoring should be random). Our data may not strictly meet this criterion, as very high metallicity points are not likely to be censored. Yet the sample was selected based on H I column density - not metallicity - and since [O/H] and [C/H] do not correlate with H I column density (see Figure 3.4) this selection method should randomize the censoring. Furthermore, since the measurements are made in data with a range of signal-to-noise ratio and blending from the Ly-α forest, the censoring will be further randomized by variations in the data quality. Thus, while the censoring pattern may not be random at the outset, several factors conspire to make it approximately random in the end. This can be seen in Figure 3.4, where upper limits are mixed in with measurements over much of the sample.

We have calculated the Kaplan-Meier distribution for our sample of metallicities using the publicly available ASURV V1.2 software suite (Lavalley et al., 1992; Feigelson & Nelson, 1985). The raw output for O VI is shown in Figure 3.6. We ran the calculations twice, once using our set of upper limit measurements that assume thermal line broadening (solid line), and once using the limits measured assuming turbulent broadening (dashed line). Both curves have included the entire *dd* and *bd* O VI samples, which will contain a (possibly large) number of false positive identifications. As expected, the curve for the turbulent sample is higher than that of the thermal sample. This is caused both by the turbulent upper limits being less sensitive than the thermal upper limits, and by the introduction of more false positive IDs from statistical fluctuations in the continuum. Because of the level of contamination from false O VI IDs, the raw Kaplan-Meier distribution represents only an upper bound on the true metallicity distribution.

Another point of interest is that when the analysis is repeated using only detected lines (i.e. the upper limits are ignored) the median metallicity increases by a factor of ~ 2, and the enrichment pattern is similar to what has been inferred in earlier studies of intergalactic enrichment (Ellison et al., 2000; Cowie & Songaila, 1998; Rauch et al., 1997b; Songaila & Cowie, 1996; Cowie et al.,

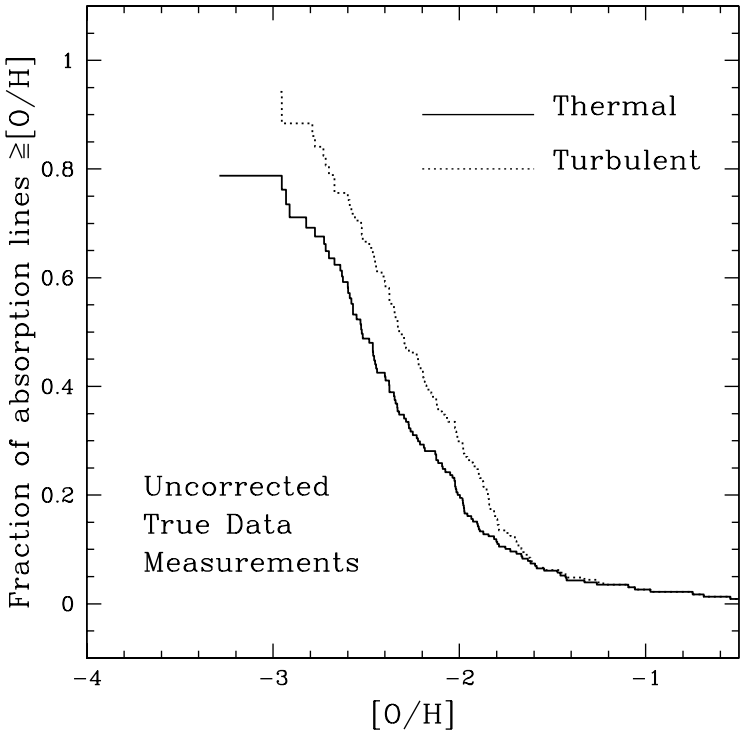

Figure 3.6 Uncorrected cumulative distribution function of [O/H] for the actual O VI data. The two curves illustrate the Kaplan-Meier estimates assuming turbulent and thermal line broadening.

1995b). The median [O/H] in this case is very near -2.5, with scatter of $0.75-1.0$ dex FWHM, and the cumulative probability distribution is $\geq 90\%$ by [O/H]=-3.0 as though there existed a metallicity "floor". A proper treatment of upper limits is therefore a critical component of the analysis, and will have important implications for the detectability of a universal, zero point metallicity for the IGM.

3.3.5 Corrections for False Positive O VI Identifications

Using the tools developed above, we are in position to calculate correction factors that remove the effect of false positive O VI IDs from the data. We accomplish this using Monte Carlo techniques, where pairs of H I and O VI lines are generated from a predetermined distribution of [O/H] and added to the data. We then use identical measurement methods and survival analyses to test our ability to recover the input metallicity distribution.

Our philosophy has been to avoid making corrections directly to the output of the Kaplan-Meier estimation. Instead, we note that the KM distribution is constructed from a list of metallicity detections and upper limits, where an unknown fraction of the detections are actually false positives. For a given detection at risk of being a false positive (e.g., a line in the *bd* sample), the column density that is measured is unquestionably at least an upper limit on the actual O VI strength. Hence for some unknown fraction of the sample, our metallicity "detections" are actually upper limits on the true metallicity. Our approach has been to use Monte Carlo simulations to determine this fraction of false positives. Then, we create several new "real" datasets from the actual data, where different random combinations but the same fraction of *bd* detections are demoted to upper limits. The KM distribution is calculated for each of these adjusted samples, and the results are averaged together to obtain our final estimate of $P(Z \geq Z_i)$.

To produce the Monte Carlo data set, we began with the observed $N_{\rm H\ I}$ and $b_{\rm H\ I}$ measurements for each quasar sightline, but reassigned a random redshift to each absorption system. The redshifts were distributed according to recent measurements of $dN/dz(z)$ in the Ly-α forest in our redshift range (Kim et al., 2001). For each H I line we then generated a corresponding O VI doublet at the same redshift. To determine the $b_{\rm O\ VI}$ values, we first assembled the distribution of $r_b = b_{\rm H\ I}/b_{\rm O\ VI}$ from observed *dd* systems, where our O VI identidications are most secure. This ratio varies from $r_b = 1$ for turbulent broadening to $r_b = 4$ for thermal broadening, with a rough probability distribution $P(r_b) \approx 0.5 - 0.07 r_b$. No variation in $P(r_b)$ was observed with H I column density. Values of r_b were drawn at random from the distribution and used to calculate $b_{\rm O\ VI}$ for each line in the sample based upon its H I linewidth.

O VI column densities were calculated for each line by inverting Equation 3.1 to find $N_{\rm O\ VI}$ given [O/H] and $N_{\rm H\ I}$. The ionization correction term as a function of H I strength was calculated with the same HM1.80 ionizing background spectrum used for the survey data (see Figure 3.2). The actual

metallicities for each line were drawn from an artificial, gaussian distribution with mean $\langle[O/H]\rangle = -2.8$ and $\sigma = 0.75$. This contrived metallicity distribution was chosen after several iterations with different backgrounds and metallicity prescriptions. We found that the correction factors did not change significantly when other reasonable backgrounds or input metallicity distributions were used. Our final background and contrived abundance distribution were chosen to resemble the patterns seen in the actual data.

We added the simulated set of H I and O VI lines to the actual spectra for all 7 quasar sightlines. This method should best replicate the actual sources of error and contamination in the real sample, including continuum fluctuations/errors, varying signal-to-noise ratio, Ly-α forest contamination, and instrumental or other more insidious effects. To minimize the possibility of artificial lines being added where real O VI was already present, none of the lines were placed at redshifts within 200 km/s of a known line with $N_{\rm H\ I} \geq 10^{13.5}$. The metallicity and O VI strength were kept hidden from the user to avoid bias in the detection process.

Finally, we searched the spectra for O VI absorption at the redshift of each artificial H I line in exactly the same manner that was used for the true data. We measured O VI column densities or upper limits for both the thermal and turbulent broadening cases at each redshift. These measurements were translated into metallicities, and a Kaplan-Meier estimate of their distribution function was constructed. These probability distributions are shown in the left panel of Figure 3.7. The thick solid line indicates the true metallicity distribution that was input to the Monte Carlo line generator. The dotted and dashed histograms represent the measured distributions assuming thermal and turbulent line broadening, respectively.

Clearly the measured distributions systematically overestimate the input distribution, presumably either because O VI column densities have been overestimated due to Ly-α forest blends, or because false positive interlopers have contaminated the sample. We cannot determine which particular detections are false positives, but the vast majority will be from the *bd* sample. To bring the measured distributions in Figure 3.7 into agreement with the input distribution, we have demoted varying fractions f_d of the *bd* detections to upper limits and recalculated the Kaplan-Meier distribution. The specific set of points to be artifically censored was chosen randomly (for several realizations), and f_d was varied until the resultant Kaplan-Meier curves produced the closest possible match to the input distribution in a least-squares sense. The exercise was repeated for both the thermal and turbulent distributions; the final corrected Monte Carlo measurements are shown in the right panel of Figure 3.7. Five different lines apiece are shown for the corrected thermal and turbulent distributions, corresponding to five realized combinations of the random censoring. It was not surprising to find that the false positive rate was quite high. For the thermal sample, the optimal demotion fraction was $f_d = 57\%$, whereas for the turbulent sample $f_d = 87\%$.

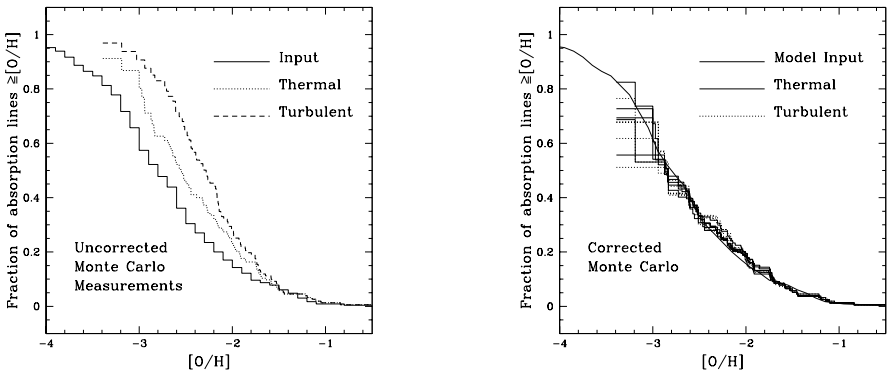

Figure 3.7 Illustration of the Monte Carlo method to determine correction factors for false positive O VI IDs in the data. The thick solid line (smoothed in the right panel) indicates the actual distribution of metallicities put into the simulated spectra. In the left panel, we show the raw Kaplan-Meier distributions resulting from measurements of the simulated lines, in the presence of noise and Ly-α forest blending. The corrected curves in the right panel are created by randomly re-assigning 57% of the 3σ thermal *bd* systems as upper limits (e.g. because of Ly-α forest contamination). An 87% correction was required when turbulent line broadening was assumed. Five realizations of the censoring are shown for each case of the assumed line broadening, to provide a sense of the random scatter in the distributions after our correction procedure.

3.3.6 Final Estimates of the Metallicity Distribution

Once the f_d factors had been determined, we applied the same corrections to the actual survey data. The results are shown in Figure 3.8. Encouragingly, the corrected thermal and turbulent distribution functions are in quite close agreement. Comparison of Figures 3.7 and 3.8 indicates that the magnitude and sense of our contamination corrections are similar for the Monte Carlo and real samples. This increases our confidence that the measurement and correction techniques are sound, at least for similar intrinsic distributions of [O/H]. As a test, we used the same correction factors to see whether we could recover a quite different artificial metallicity distribution - a step function with $P([O/H] < -2.5) = 1$ and $P([O/H] > -2.5) = 0$. Again, the Kaplan-Meier method performed well. A strong discontinuity was recovered at $[O/H] \approx -2.45$, though it was broadened by ~ 0.5 dex.

In Figure 3.9, we show the derived distributions of [O/H] and [C/H] together. For this figure only, we have restricted the O VI systems to have $N_{\rm H\ I} > 10^{14}$, for fair comparison with the C IV sample. The distributions were generated using the HM1.80 model of the ionizing background normalized to $\log J_{912} = -21.5$. We have tested a wide range of slopes and normalizations for the background spectrum, and chosen this form as our best case, since it produces the best match between the curves in Figure 3.9. The difference between the two distributions is well within the errors of the data over the entire observed range of metallicity.

The distribution in Figure 3.8 (which includes all O VI lines) is our best estimate of the metallicity distribution function of the Ly-α forest. Even at the lowest observed values, the cumulative

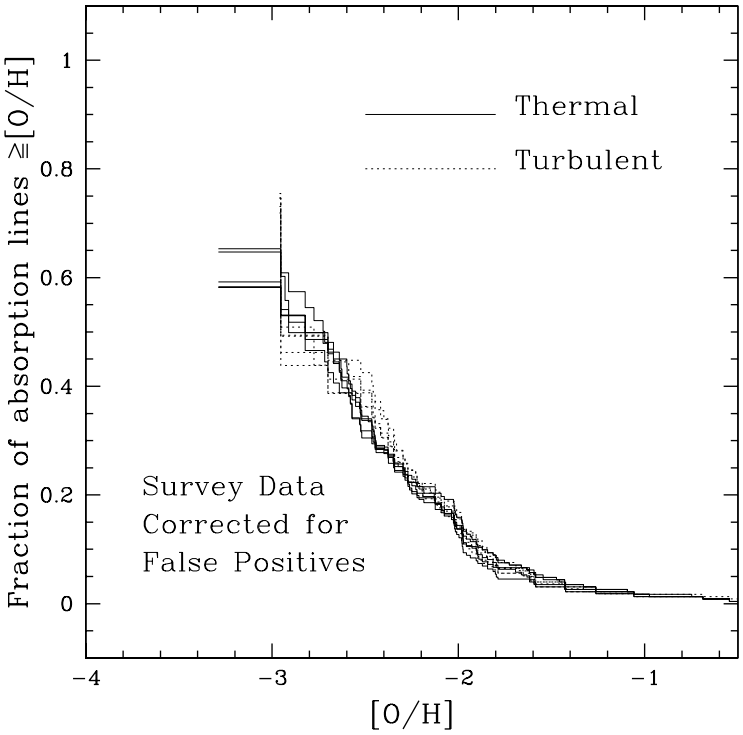

Figure 3.8 The contamination corrected cumulative distribution of [O/H] in the Ly-α forest. We have applied the censoring factors determined from Monte Carlo testing. Again, five censoring combinations are shown for each broadening case, as an indication of the residual scatter from the contamination correction.

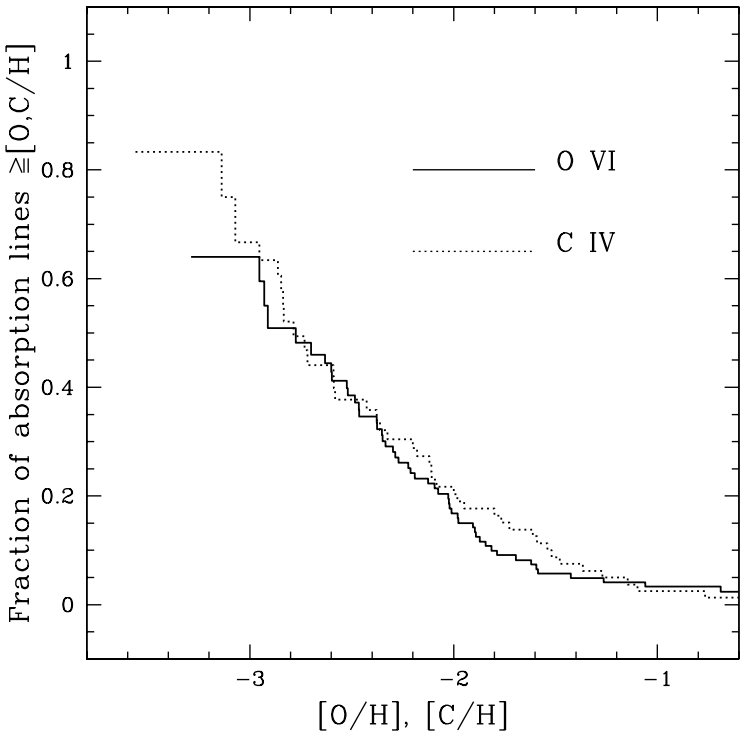

Figure 3.9 Comparison of the Kaplan-Meier distributions for oxygen and carbon. We have assumed our fiducial HM1.80 model for the UV background, which was chosen to produce the best possible match between these two curves (i.e., we have assumed $[O/C] = 0$). For harder models of the background, C IV is overproduced relative to O VI. This model produces an excellent statistical match between the two distributions.

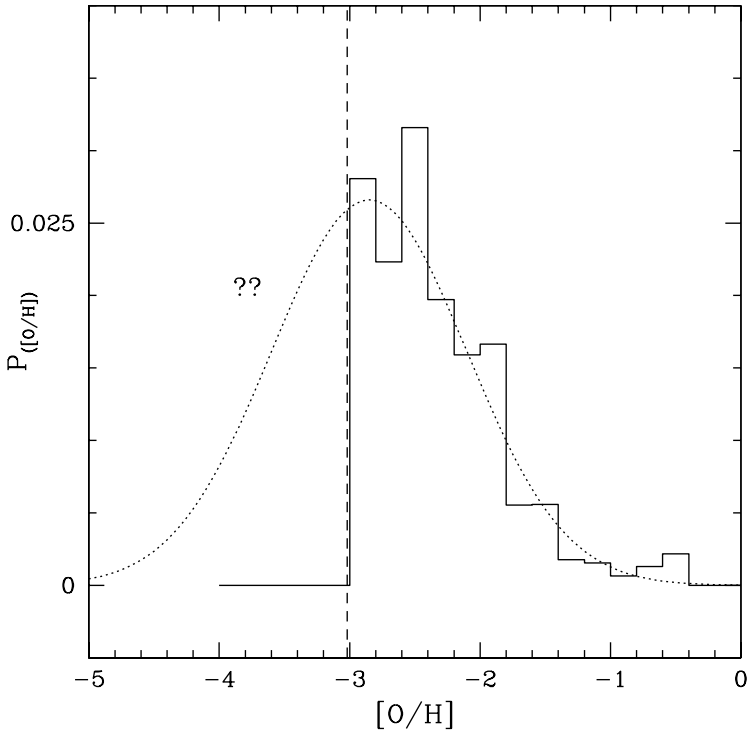

Figure 3.10 The differential distribution function of [O/H], derived from the Kaplan-Meier estimator. The dashed vertical line represents the approximate detection limit of the survey. The dotted curve is a unit area gaussian, with mean $\langle [O/H] \rangle = -2.85$ and $\sigma = 0.75$, a reasonable analytic estimate of the IGM metallicity to the limits of our data.

distribution does not reach 100%. Roughly 70% of the forest has been enriched to $[O/H] \geq -3.5$. Thus *we have detected neither a metallicity "floor" in the IGM, nor a transition toward chemically pristine gas at low densities.* An abundance floor could exist at $[O/H] \leq -3.5$, or some of the remaining 30% of lines may be nearly metal-free.

We find a median intergalactic abundance of $[C, O/H] = -2.81$, quite similar to prior studies suggesting $-2.5 \leq [O/H] \leq -2.0$ (Cowie & Songaila, 1998; Ellison et al., 2000), though a factor of $2 - 4$ lower. The mean is formally unconstrained, as our lowest measurements are upper limits. Some further insight may be gained by examining the *differential* abundance distribution, which we have also calculated using ASURV using the algorithms presented in Wardle and Knapp (1986). The differential O VI distribution is shown in Figure 3.10, and is quite similar to the C IV distribution which is not shown. The vertical dotted line indicates the weakest detection in the sample (though there are some lower upper limits). The lines appear to be drawn from a single, fairly uniform distribution in [O/H] that peaks near the median metallicity. We cannot probe the lower half of the distribution as it lies below our sensitivity threshold, but we know that there must be a substantial dropoff - since we have already accounted for $\sim 70\%$ of the lines (in a statistical sense), the integrated

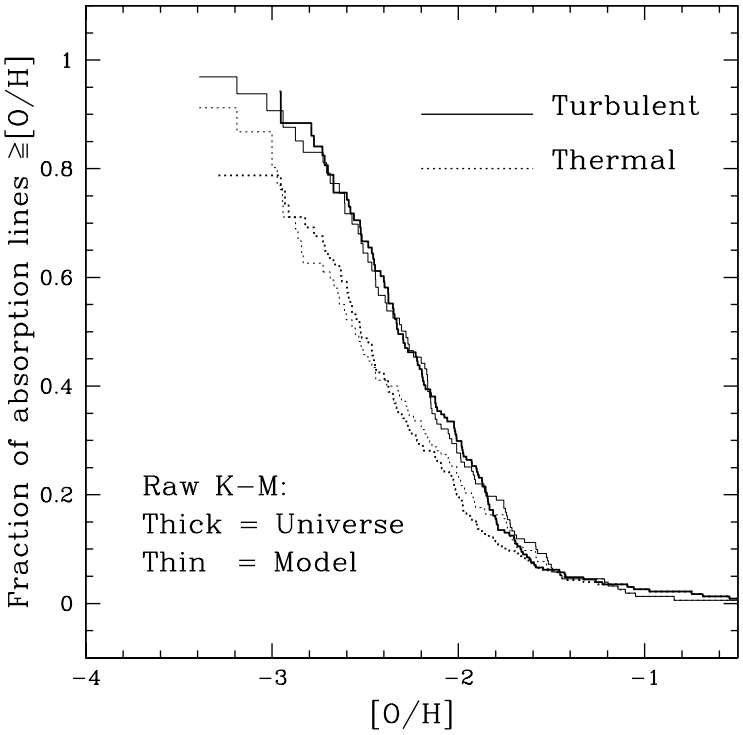

Figure 3.11 Comparison of the raw (uncorrected) [O/H] distribution seen in the survey data (thick lines) with the raw distribution produced by adding simulated systems to the spectra with our best estimate of the differential [O/H] distribution (thin lines). Our simple lognormal metallicity model mimics the real spectra over a broad range of [O/H].

area to the left of the sample cutoff should be at most $\sim 30\%$ of the forest lines. The observed part of the distribution resembles a unity normalized gaussian PDF, with mean $\langle [C, O/H] \rangle = -2.85$, and $\sigma = 0.75$ dex. In terms of $Z/Z_{\odot}$, the distribution of metallicity would be lognormal.

To illustrate how our model corresponds to what is seen in the actual spectra, we show again in Figure 3.11 the *raw* Kaplan-Meier O VI distribution, which has not been corrected for false positive identifications. Both the thermal and turbulence broadened measurements are shown, as the thick dotted and solid lines, respectively. On the same graph, we have plotted the *raw* Kaplan-Meier distributions of a simulated dataset with the lognormal metallicity distribution described above (shown as matching thin curves). A simple, single population model for the metallicity distribution (along with a uniform ionizing background) reproduces the actual survey results extremely well, over the entire measureable range.

3.3.7 Cosmic Mass and Volume Fractions Probed by the Survey

We now present a simple method for recasting the observed fractions of absorption lines at different abundances into more physical terms. We are particularly interested in the mass and volume fractions

of the universe that are enriched to various levels. To estimate this distribution, we first recall that we have fit Voigt profiles to every H I line in the Ly-α forest. This was originally done to remove higher order H I transitions for the O VI search, but the line lists also provide detailed information on the column density distribution of H I in the exact redshift window of the survey. This information may be used to calculate the total mass fraction of baryons probed by the survey, and by extension the volume fraction.

Our mass fraction calculation follows the development of Schaye (2001), and we begin with his Equation 16:

$$\Omega_g \propto \int N_{\rm H\ I}^{1/3} f_{(N_{\rm H\ I},z)} dN_{\rm H\ I}. \tag{3.10}$$

Here, $f_{(N_{\rm H\ I},z)} = d^2\mathcal{N}/dN_{\rm H\ I}dX$ represents the number of H I absorption lines per unit $N_{\rm H\ I}$ and per unit absorption pathlength [4], and is calculated directly from the H I line lists. We have assumed (as in Schaye) that the gas is isothermal, and that the fraction of the total cosmic mass contained in gas is close to Ω_b/Ω_m. Using Equation 3.10, we may infer the fraction of Ω_g contained in each decade of $N_{\rm H\ I}$:

$$\frac{d\Omega_g}{d\log N_{\rm H\ I}} = \frac{d\Omega_g}{dN_{\rm H\ I}} \cdot N_{\rm H\ I} \propto N_{\rm H\ I}^{\frac{4}{3}} \cdot f_{(N_{\rm H\ I},z)}. \tag{3.11}$$

This quantity is plotted in Figure 3.12, with the points and errors taken directly from the H I distribution of the data. The vertical normalization of the plot is arbitrary, and the points are equally spaced in $\log N_{\rm H\ I}$. The distribution should be quite accurate over the range $10^{12.5} < N_{\rm H\ I} < 10^{15}$, where distinct absorption lines are clearly visible in the data and line saturation is not severe. At higher $N_{\rm H\ I}$ there is an increased uncertainty in our column density measurements for some systems. Since the primary purpose of the line fits was to facilitate the O VI search, the fit quality was not as uniformly high over all H I transitions for high density systems that did not have bearing on an O VI measurement. Furthermore, the exact shape of the turnoff below $N_{\rm H\ I} \sim 10^{13}$ is the subject of some contention, as it results from a combination of real, physical effects and observational incompleteness. Though we may miss some amount of the mass in this region, cosmological simulations indicate that there should be a real and significant drop in the mass density contained in systems below $N_{\rm H\ I} \sim 10^{12.5}$. Whatever the case, the accuracy of the data is highest over the range which contains most of the mass. We shall show below that these uncertainties do not change our qualitative results.

The H I cutoff of the O VI sample ($N_{\rm H\ I} \geq 10^{13.6}$) is shown in Figure 3.12 as a vertical dashed line. We wish to determine what fraction of the total gas mass lies to the right of this line. A simple inspection suggests that this fraction is close to one half, which turns out to be remarkably close to

[4] The absorption pathlength is similar to a redshift interval, scaled to comoving units. In a flat universe, a QSO sightline ranging from z_{min} to z_{max} has an absorption pathlength of $\Delta X = \frac{2}{3\Omega_M}\left[\sqrt{\Omega_M(1+z_{max})^3+\Omega_\Lambda} - \sqrt{\Omega_M(1+z_{min})^3+\Omega_\Lambda}\right]$.

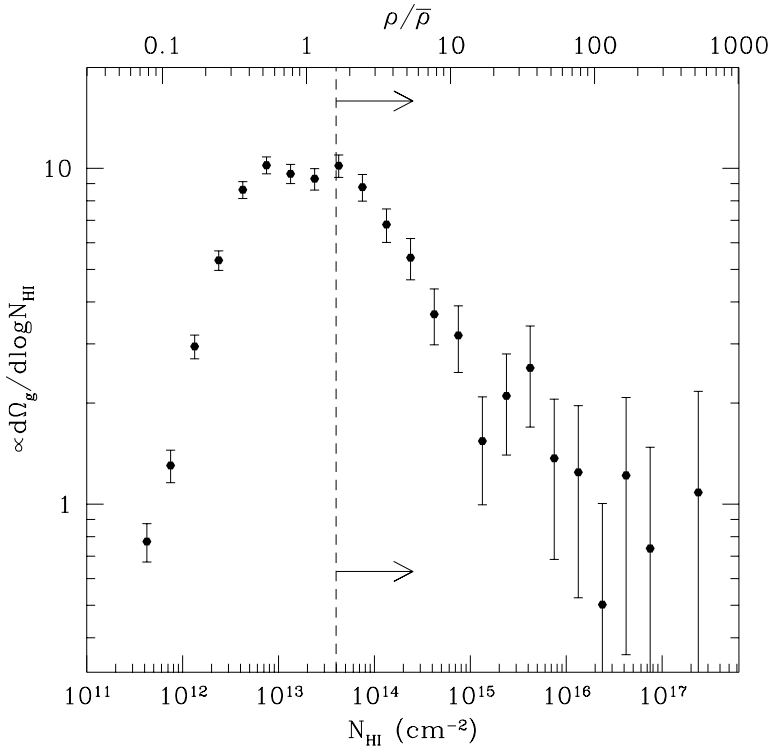

Figure 3.12 The mass fraction of intergalactic gas contained in each decade of H I column density for our line samples. The vertical dashed line indicates the low density cutoff of the O VI sample, which encompasses ~ 50 of Ω_g.

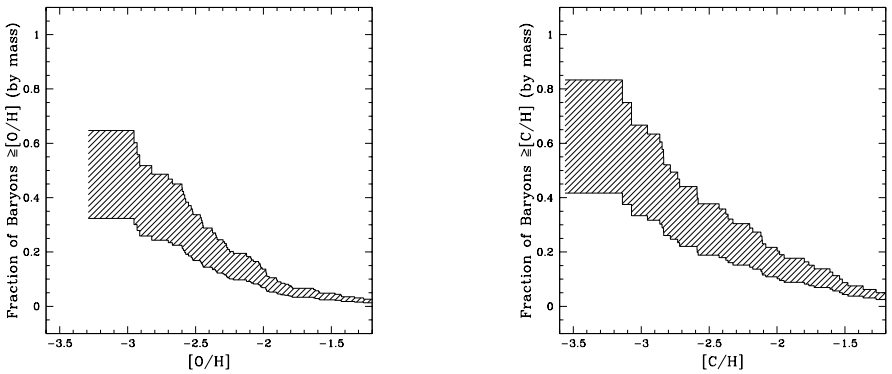

Figure 3.13 The enriched mass function of the IGM, calculated from the O VI and C IV observations.

the true value. Since the data are equally spaced in the log, we may simply sum the points to the right of the line, and normalize by the sum of all points to determine what fraction of Ω_g is probed by the survey. Depending on whether lines with $N_{\rm H\ I} > 10^{17.5}$ are included in the calculation (since they suffer from small number statistics), we find that the survey probes between $51 - 57\%$ of the total Ω_g. Incompleteness at $N_{\rm H\ I} < 10^{12}$ has little effect on the results, although incompleteness at $10^{12} \leq N_{\rm H\ I} \leq 10^{12.5}$ could reduce our coverage to $\sim 42\%$ of Ω_g if we have undercounted these lines by a factor of 3 (a fairly conservative estimate). Accounting for a range of uncertainty in our measurement of the H I column density distribution, we estimate that our survey probes roughly $42 - 57\%$ of the gas in the universe at $z \sim 2.5$ by mass, with the most likely value being close to 50%.

In Figure 3.13, we apply this information to determine the mass fraction of baryons that have been enriched to a given oxygen abundance, which we call the enriched mass function, or EMF. The two curves that bound the shaded region of the plot represent upper and lower limits on the EMF, derived using two different assumptions about the trend of [O/H] versus $N_{\rm H\ I}$ below our survey's H I threshold. If we define $p_{([O/H],N_{\rm H\ I})}$ as the differential probability that a line with $N_{\rm H\ I}$ will possess an oxygen abundance $[O/H]$, the EMF is defined as

$$\mathrm{EMF} = f_{\mathrm{mass}(\geq[O/H])} = \frac{\int_{[O/H]}^{\infty}\int_{-\infty}^{\infty} p_{([O/H],N_{\rm H\ I})}\frac{d\Omega}{d\log N_{\rm H\ I}}d(\log N_{\rm H\ I})d\left(\left[\frac{O}{H}\right]\right)}{\int_{-\infty}^{\infty}\frac{d\Omega}{d\log N_{\rm H\ I}}d(\log N_{\rm H\ I})}. \qquad (3.12)$$

To produce the upper bound, we suppose that the intergalactic enrichment pattern seen in our data continues to arbitrarily low densities, filling the entire volume of the universe. In this case, $p_{([O/H],N_{\rm H\ I})}$ is independent of $N_{\rm H\ I}$ (See Figure 3.4) and the integrals over $\log N_{\rm H\ I}$ and $[O/H]$ may be separated. The ratio of the density integrals reduces to unity, and we are left with the expression

$$f_{\mathrm{mass}(\geq[O/H])} \leq \int_{[O/H]}^{\infty} p_{([O/H],N_{\rm H\ I})}d\left(\left[\frac{O}{H}\right]\right) = P_{(\geq[O/H])}. \qquad (3.13)$$

Thus the upper bound for the EMF is simply the cumulative distribution of *line* enrichment, i.e. the Kaplan-Meier distribution shown in Figure 3.8. We have implicitly assumed that the lowest density regions of the IGM are not *more* heavily enriched than the highly overdense areas.

To produce the EMF's lower bound, we suppose that all gas in clouds with $N_{\rm H\ I} < 10^{13.6}$ is chemically pristine, i.e., that we have already observed all of the heavy elements in the universe. Now, Equation 3.12 becomes

$$f_{\rm mass(\geq [O/H])} \geq P_{(\geq [O/H])} \times \frac{\int_{13.6}^{\infty} \frac{d\Omega}{d\log N_{\rm H\ I}} d(\log N_{\rm H\ I})}{\int_{-\infty}^{\infty} \frac{d\Omega}{d\log N_{\rm H\ I}} d(\log N_{\rm H\ I})} \approx 0.5 P_{(\geq [O/H])}. \tag{3.14}$$

In the last step, we have used the above estimate that $\sim 50\%$ of all baryonic mass is in clouds with $N_{\rm H\ I} \geq 10^{13.6}$. The upper and lower bounds on the EMF given by Equations 3.13 and 3.14 were used to produce the shaded regions in Figure 3.13.

It is more difficult to estimate the volume filling factor of enriched gas without reference to simulations, due to the complex nature of the Ly-α forest topology, and the lack of a simple analytic form for the volume fraction $dV/dN_{\rm H\ I}$. However, simulations can easily calculate the volume fraction within a given H I density contour, or which contains a certain fraction of Ω_b. Figure 20b in Miralda-Escude et al. (1996) may be used to estimate the filling factor of the contour containing half of the baryons at $z = 3$. This number turns out to be small, only $\sim 5\%$ of the total volume of the universe. One can guess why this is the case from Figure 3.12; we probe to an overdensity of $\rho/\bar{\rho} \sim 1.6$, and most of the mass in the universe is at densities slightly above the mean (the filaments), while most of the volume is at densities slightly below the mean (the voids). We again emphasize, *we have traced the metal distribution throughout the cosmic filaments, which contain most of the baryonic mass at high redshift.* The densities we measure do not reach the voids, which encompass most of the volume.

3.3.8 Contribution of Intergalactic Oxygen and Carbon to Closure Density

We have estimated the quantity $\Omega_{\rm C\ IV}$ using two different methods, initially to compare with previous studies and then to test the consistency of our ionization model. The first calculation takes a direct sum of the observed C IV column densities, as in Songaila (2001):

$$\Omega_{\rm C\ IV} = \frac{1}{\rho_c} m_{\rm C\ IV} \frac{\sum N_{\rm C\ IV,i}}{\frac{c}{H_0} \sum \Delta X_i}. \tag{3.15}$$

Here $\rho_c = 1.89 \times 10^{-29}$ gm cm^{-2} is the current closure density, $m_{\rm C\ IV}$ is the mass of the C IV ion, and the upper sum includes all observed C IV lines. The lower sum represents the total absorption pathlength of the sample (defined in the previous section), which summed over our 2 C IV sightlines

comes to $\Delta X = 3.27$. Applying this to the data we find $\Omega_{\rm C\ IV} = 3.50 \times 10^{-8} h^{-1}$ (where $H_0 = 100h$ km s^{-1} Mpc^{-1}). This is in excellent agreement with other estimates of $\Omega_{\rm C\ IV}$ at $z \sim 2.5$ from the literature (Songaila, 2001; Boksenberg et al., 2003).

With this benchmark in hand, we now recalculate $\Omega_{\rm C\ IV}$, this time starting from the observed distribution of H I in the forest, and applying our metallicity and ionization models to predict the total amount of C IV. A comparison of this result with the straightforward sum from Equation 3.15 tests the consistency of the enrichment model. We begin with the H I column density distribution function $f_{(N_{\rm H\ I},z)}$, calculated from our H I line fits as described in the previous section. We may perform a weighted integral of $f_{(N_{\rm H\ I},z)}$ to obtain an analogue of the last expression in Equation 3.15, with H I substituted for C IV :

$$\frac{\sum N_{\rm H\ I}}{\frac{c}{H_0}\sum \Delta X} \approx \left(\frac{c}{H_0}\right)^{-1} \int N_{\rm H\ I} f_{(N_{\rm H\ I},z)} dN_{\rm H\ I}. \tag{3.16}$$

Folding in metallicity and ionization corrections, we derive the C IV mass density, again through analogy with Equation 3.15:

$$\Omega_{\rm C\ IV} = \frac{1}{\rho_c} m_{\rm C\ IV} \left\{ \left(\frac{C}{H}\right)_\odot \cdot \left\langle 10^{[C/H]} \right\rangle \cdot \left(\frac{c}{H_0}\right)^{-1} \cdot \int N_{\rm H\ I} f_{(X,N_{\rm H\ I})} \frac{f_{\rm C\ IV}}{f_{\rm H\ I}} dN_{\rm H\ I}. \right\} \tag{3.17}$$

The ionization correction factors, taken from our CLOUDY calculations (and shown in Figure 3.3), are density dependent and therefore included in the integral. We assume the metallicity distribution is independent of $N_{\rm H\ I}$, after Figure 3.4. To calculate the mean metallicity, we assume the [C/H] and [O/H] distributions are identical, and use the approximation for the [O/H] distribution described Section 3.6 - a gaussian with mean $\left\langle \left[\frac{O}{H}\right] \right\rangle = -2.85$ and $\sigma = 0.75$. The distribution of $10^{[C/H]}$ is therefore lognormal, with mean

$$\left\langle 10^{[C/H]} \right\rangle = \exp\left[\ln 10 \times \left\langle \left[\frac{C}{H}\right] \right\rangle + \frac{1}{2}(\ln 10 \times \sigma)^2 \right] = 10^{-2.20}. \tag{3.18}$$

Using these values in Equation 3.17, we find $\Omega_{\rm C\ IV} = 1.78 \times 10^{-8} h^{-1}$, similar to the value found from Equation 3.15, but about a factor of 2 lower. This discrepancy is less significant than it may first appear, since the sum in Equation 3.15 is always dominated by the few strongest systems in the sample. In our case, three strong outliers from a sample of 83 lines contain over half of the total C IV column density. These are clearly seen in Figure 3.1; they are found within very strong C IV systems that probably do not represent tenuous intergalactic matter. A re-evaluation of Equation 3.15 without these three lines included yields $\Omega_{\rm C\ IV} = 1.31 \times 10^{-8}$, bringing the estimates from both methods into close agreement. This also suggests that a major portion of the C IV mass in the universe may be contained in a small number of systems that are highly enriched or harbor unusual ionization conditions.

Table 3.2. Contribution of Intergalactic Metals to Closure Density

Quantity	$\Omega(\times h^{-1})$	Method
$\Omega_{\rm C\ IV}$	3.50×10^{-8}	Eqn. 3.15 [1]
$\Omega_{\rm C\ IV}$	1.31×10^{-8}	Eqn. 3.15 [1]
$\Omega_{\rm C\ IV}$	1.78×10^{-8}	Eqn. 3.17
$\Omega_{\rm O\ VI}$	7.89×10^{-8}	Eqn. 3.17
$\Omega_{\rm Carbon}$	5.10×10^{-7}	Equation 3.17[2]
$\Omega_{\rm Oxygen}$	1.38×10^{-6}	Equation 3.17[2]

[1]The first row was calculated using the entire C IV sample; the second omits the three strongest lines (out of 83) which contain over half of the mass and may not be representative of the intergalactic distribution (see text).

[2]Calculated using Equation 3.17, but with the ionization correction factors $f_{\rm C\ IV}$ or $f_{\rm O\ VI}$ omitted.

When estimating $\Omega_{\rm O\ VI}$, it is considerably more difficult to perform the calculation in Equation 3.15 because of Ly-α forest blending and false positive identifications. We have accounted for these effects in our determination of the metallicity distribution, so it is much more strightforward to apply Equation 3.17, yielding $\Omega_{\rm O\ VI} = 7.89 \times 10^{-8}$. By omitting the O VI or C IV ionization corrections from Equation 3.17 (but retaining the H I correction) we may estimate the total contribution of carbon or oxygen in all ionization states to the closure density. The resulting values are listed in Table 2 along with the values for the C IV and O VI ionization states. Qian et al. (2002) have constructed an observationally motivated enrichment model for the galactic halo, requiring several generations of supernovae from very massive stars. Their prediction for $\Omega_{\rm C\ IV}$ from this model is an order of magnitude lower than the estimate presented here, and their $\Omega_{\rm O\ VI}$ is 1.65 times larger than our measurement. We caution the reader that estimates of [C/O] from our measurements will not be meaningful, as we have constrained our models of the ionizing background by requiring a solar [C/O] ratio.

Equation 3.17 is of further interest because it can be used to determine what fraction of the total C IV (or O VI mass) in the universe has been detected in the survey. This is achieved by changing the limits of the H I integration to match our column density cutoffs - $N_{\rm H\ I} \geq 10^{13.6}$ for O VI and $N_{\rm H\ I} \geq 10^{14.0}$ for C IV. According to this method, our limits probe 98.8% of the C IV mass and 90% of the O VI mass.

3.4 Discussion

We have shown that cosmological filaments are enriched with oxygen and carbon to near the mean gas density in the universe, and that the median $[C, O/H] = -2.82$ is similar to previous estimates, though about a factor of 2 lower. We have also shown several systems with very low abundances, implying that $\sim 30\%$ of Ly-α forest lines have metallicities of $[C, O/H] \lesssim -3.5$. In this section, we examine our results in the context of cosmic chemical evolution models, to assess their relevance for distinguishing between different enrichment mechanisms.

In Figure 3.14, we show a variant of the metallicity-density relation from the O VI sample, now recast in terms typically used in numerical simulations. All points from the *dd* and *bd* samples are shown, so $\sim 60\%$ of the detections are false positives. The error bars on detected points have been omitted for clarity. Along with the data points, we have indicated the expected metallicity-density relations for different chemical enrichment scenarios. We consider two classes of models: one where metals are expelled at very early times by the first generation of stars, and one where the ejection epoch occurs much later and is associated with bursts of "normal" star formation and galactic winds.

Recent studies of star formation in zero metallicity environments show that the first stars in the universe probably formed via H_2 cooling (Abel et al., 2002; Bromm et al., 2002; Ostriker & Gnedin, 1996). These "Population III" stars were uniformly massive ($M \sim 150 - 250 M_\odot$) and short lived, culminating in pair-instability supernovae that disrupted the entire mass of the star, leaving no remnant (Heger & Woosley, 2002). Yield calculations by these authors indicate that fully half of the total stellar mass can be converted into metals and expelled. All of this takes place prior to $z \sim 30$, at which point the stars are in comparatively small haloes that are close together. Thus the Population III objects provide a potentially efficient mechanism to enrich a large fraction of the cosmic volume. However, this mode of star formation is also self-regulating, which leads to a natural limit to the quantity of metals that can be produced. When the first Population III objects form, they shine brightly in the near ultraviolet and emit enough photons in the Lyman Werner bands to photodissociate all of the nearby H_2, turning off the cooling source required to produce more stars. Thus the first major epoch of star formation and metal enrichment is thought to end at $z \sim 25 - 30$ (Mackey et al., 2003).

The resulting contribution to the intergalactic metal abundance depends on fairly uncertain models of the star formation rate prior to $z \sim 30$ and the efficiency with which the supernova ejecta can escape protogalactic haloes and mix with distributed gas. In the figure we have shaded a region that reflects current estimates of the Population III metal production, for mixing efficiencies between 5% and 50% (Mackey et al., 2003). The horizontal dashed line represents a more strict upper limit to the Population III enrichment level. Bromm et al. (2001) have shown that massive, H_2 cooled stars will not form from gas with metallicity above this value, as atomic line cooling becomes too

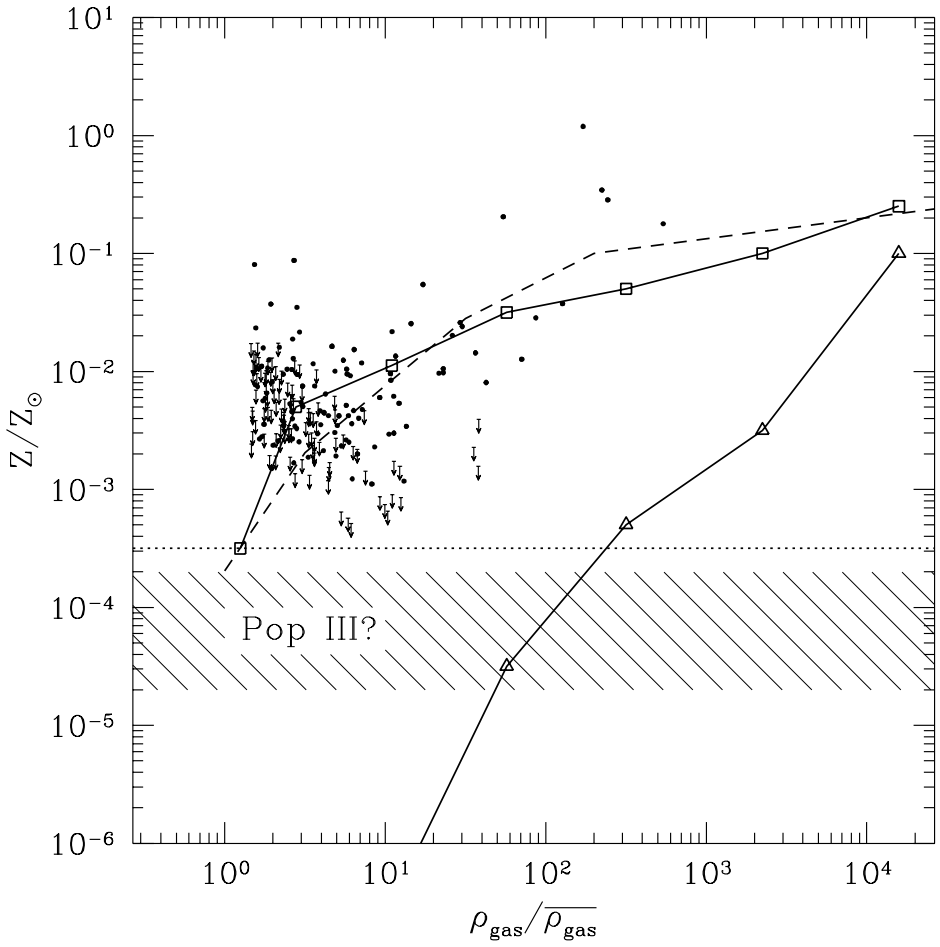

Figure 3.14 Oxygen abundances for individual Ly-α forest lines, plotted against their gas overdensity derived from $N_{\rm H\,I}$. Data from the *dd* and *bd* sample are shown as solid points, though error bars have been suppressed for clarity. 3σ upper limits are shown with arrows. The continuous curves depict predictions for several numerical calculations of the intergalactic enrichment, based on phenomenological models of star formation and metal ejection. The open squares and triangles represent $z = 2.3$ models from Springel & Hernquist (2003) with and without winds, respectively. The dashed line is taken from the $z = 3$ wind model of Aguirre et al. (2001). The shaded region encompasses a possible range of enrichment from H_2 cooled Population III stars, while the horizontal dotted line represents an absolute upper limit on the metallicity of these objects (Bromm et al., 2001, also see text).

efficient to maintain large scale stability, and a collapsing cloud fragments into smaller mass units.

It is clear that the metals we have detected at $\rho/\bar{\rho} \gtrsim 1$ are in excess of the Population III production levels, in some cases by several orders of magnitude. Some of our most sensitive upper limits are within a factor of 2 of the model predictions (recall that these are 3σ limits), indicating that parts of the IGM could still possess Population III enriched gas. It is also intriguing that an extrapolation of the Kaplan-Meier cumulative metallicity distribution (Figure 3.8) suggests a universal floor just below $[C, O/H] = -4.0$, about where one might expect to pick up Population III metals. This speculation is neither ruled out, nor required by the data.

We now turn to chemical enrichment models based on more recent star formation and galactic winds. This mode of metal production is more familiar, as starburst galaxies and superwinds have been observed extensively at low and high ($z \lesssim 5$) redshifts (Lehnert & Heckman, 1996; Pettini et al., 2001; Dawson et al., 2002). The stellar physics and populations basically resemble those in the local neighborhood, except that at $z \gtrsim 2.5$ the star formation rate in the typical galaxy was much higher, and the IMF may have been tilted towards high mass (Pettini et al., 2002). The physics of superwinds is extremely complex, and a detailed understanding of their impact on the IGM requires numerical simulations that draw heavily on observationally motivated recipes for star formation, metal yields, and wind energetics. Once these ingredients are in place, the simulations provide an excellent view of how ejecta interact and mix with the surrounding IGM.

We have shown the predicted metallicity-density relations from 3 different simulations with continuous curves in Figure 3.14. The solid line connecting open triangles represents a simulation from Springel & Hernquist (2003) that includes local metal enrichment but no galactic winds. The solid line with open squares represents a separate run by the same authors, this time with a fiducial wind model tuned to match observations at low redshift. Both curves are for $z = 2.3$. The dashed curve shows the "W128" simulation of Aguirre et al. (2001) at $z = 3$, which was calculated by applying a wind model to already completed numerical simulations. Again, the star formation and feedback parameters were adjusted to match local observations.

We confirm these authors' finding that models with galactic winds are able to enrich the universe to the levels required by observations. Moreover, the model without winds grossly underestimates the cosmic metallicity, implying that *essentially all of the heavy elements yet observed in the IGM were expelled from galaxies at relatively recent epochs*, loosely $3 \lesssim z \lesssim 10$. Both wind models predict a mild correlation of increasing $Z/Z_\odot$ with density, and there is a weak indication that this trend follows the data. However, we again caution that our metallicity measurements are less accurate at $\rho/\bar{\rho} > 100$ (see Sections 3.1,3.2), and the correlation is very weak at lower densities. No such trend is seen in the C IV data. Many of the absorption lines in the range $\rho/\bar{\rho} = 100 - 300$ may in fact represent snapshots of the evolving winds themselves, in which case our photoionization models will probably overestimate [O/H]. These absorbers are complex and multiphased, but their abundances

have been crudely estimated at $[O/H] \gtrsim -1.5$ (Simcoe et al., 2002), roughly consistent with the models.

Many of our points and upper limits fall well *below* the wind model predictions. This is most clearly seen at $\rho/\bar{\rho} \sim 8-50$ and may extend to lower densities; the lack of measurements at $\rho/\bar{\rho} \sim 1-2$ and $Z/Z_{\odot} \leq 10^{-3}$ is a selection effect, caused by the signal-to-noise dependent detection thresholds of the data. Unfortunately, our data are not sensitive enough to probe $\rho/\bar{\rho} \leq 1$, where both wind models predict sharp abundance falloffs. With the large parameter space spanned by the wind and no-wind models, it seems likely that any plausible abundance pattern could be reproduced given a proper distribution of wind ejection velocities and metal content. The model curves represent a volume average of $Z/Z_{\odot}$ at different densities; it will be interesting to test the dispersion in simulated metallicities with density against the data, though this is beyond the scope of this paper.

It appears Population III derived metals do not dominate the intergalactic distribution until one enters the underdense IGM. Even then, their spatial variation could be strongly affected if Population III star formation is strongly biased. It will be difficult to probe these metals using direct O VI measurements, as the fluctuations are at the $\sim 1\%$ level from the continuum. Larger telescopes with very stable instrumentation will be required, and even then the effects of the Ly-α forest may render such measurements impossible. A more promising approach for the far future will be to search for intergalactic O VII and O VIII absorption, as these are the dominant ionization states in the voids. However, the technical challenges involved in observing weak O VII and O VIII at high redshift will still be major obstacles for many years to come.

3.4.1 The Ultimate Closed Box?

We now consider a simple, global model of the chemical evolution of the universe. This model is analogous to chemical models of the galactic ISM, but rather than focusing on the transport of mass and chemicals between stars and the ISM, we study the transport of mass and chemicals between galaxies and the IGM, to determine the average chemical yield of galaxies in the early universe. As in galactic chemical evolution models, we assume that metals are recycled instantaneously, so for each $dM_{\rm gal}$ of mass flowing into galaxies, a corresponding mass $ydM_{\rm gal}$ of heavy elements is immediately returned to the IGM. The quantity y is therefore a heavy element yield for galaxy formation. The instantaneous approximation should work marginally well for the IGM, since the timescale for massive stellar evolution ($\tau \lesssim 10^7$ years for a $M \gtrsim 15M_{\odot}$ star) and galactic winds ($\tau \sim 10^7 - 10^8$ years; Shapley et al., 2001) is shorter than cosmic timescales ($\tau \sim 10^9$ years) at $z \sim 2.5$.

We define $\phi_{\rm gal}$ as the rate of mass deposition into galaxies from the IGM; this mass may either be converted into stars or reside in the ISM of the galaxy. In each galaxy that is formed, a fraction $f_{\rm ent}$ of the ISM may be entrained in outflows and removed from the galaxy before it is substantially

enriched. The exchange of mass due to galaxy formation is then governed by the equations:

$$\frac{dM_{\rm IGM}}{dt} = -(1-f_{\rm ent})\phi_{\rm gal} \tag{3.19}$$

$$\frac{d}{dt}(ZM_{\rm IGM}) = y(1-f_{\rm ent})\phi_{\rm gal} - Z(1-f_{\rm ent})\phi_{\rm gal} \tag{3.20}$$

where $M_{\rm IGM}$ is the total mass of gas in the IGM, and as usual Z is the fraction of $M_{\rm IGM}$ bound up in heavy elements. By differentiating Equation 3.20 and dividing by Equation 3.19, we obtain

$$M_{\rm IGM}\frac{dZ}{dM_{\rm IGM}} = -y. \tag{3.21}$$

We have assumed that the total mass $M_{\rm tot} = M_{\rm IGM} + M_{\rm gal}$ remains constant, i.e., there are no significant sources or sinks. We further assume the initial conditions $Z(t_0) = 0, M_{\rm gal}(t_0) = 0, M_{\rm gas}(t_0) = M_{\rm tot}$. This is equivalent to the "simple closed box" model of galactic chemical evolution. Obviously, the IGM plus galaxies represent the ultimate closed system.

The solution to Equation 3.21 is

$$Z_{\rm IGM} = y\ln\left(\frac{M_{\rm tot}}{M_{\rm IGM}}\right). \tag{3.22}$$

We may use this relation to constrain the metal yield from galaxies in the era before $z \sim 2.5$. We have calculated Z from the metallicity measurements provided above, noting that $Z_{\rm IGM} = \left\langle 10^{[\rm O/H]}\right\rangle Z_\odot$, with $\left\langle 10^{[O/H]}\right\rangle \sim 10^{-2.2}$ and $Z_\odot = 0.02$, hence $Z_{\rm IGM} = 1.3\times10^{-4}$. The quantities $M_{\rm tot}$ and $M_{\rm IGM}$ may be estimated using recent observations, first noting that

$$\frac{M_{\rm tot}}{M_{\rm IGM}} \approx \frac{\Omega_b}{\Omega_{{\rm Ly}\alpha}}, \tag{3.23}$$

where $\Omega_{{\rm Ly}\alpha}$ is the contribution to closure density from diffuse gas in the Ly-α forest. The value $\Omega_b h^2 = 0.0224$ is now fairly secure from WMAP observations of the CMB (Spergel et al., 2003) and Big Bang Nucleosynthesis observations (O'Meara et al., 2001). Our estimation of $\Omega_{{\rm Ly}\alpha}$ is somewhat less certain. A lower bound on this quantity has been estimated using observations of the average flux decrement in the Ly-α forest, either by matching the observations to simulations (Rauch et al., 1997c) or by requiring that the redshift and real-space extent of Ly-α forest clouds are of similar magnitude (Weinberg et al., 1997). Rescaling Weinberg's conservative estimate to a cosmology with $(\Omega_M, \Omega_\Lambda) = (0.3, 0.7)$ gives $\Omega_{{\rm Ly}\alpha}h^2 \geq 0.020$ while Rauch finds $\Omega_{{\rm Ly}\alpha}h^2 \geq 0.021$. It seems that there is basic agreement on a lower limit for the mass of the forest: $\Omega_{{\rm Ly}\alpha}/\Omega_b \gtrsim 0.92$.

We can estimate an upper limit for $\Omega_{{\rm Ly}\alpha}/\Omega_b$ by noting that $\Omega_b \approx \Omega_{{\rm Ly}\alpha} + \Omega_* + \Omega_{\rm DLA} + \Omega_{\rm WH} + \Omega_{\rm hot}$, accounting for most known sources of baryons in the universe. The various terms represent the mass of the Ly-α forest, stars, damped Ly-α systems, warm-hot ($T = 10^5 - 10^7$ K) gas, and hot gas in

galaxy clusters, respectively. To produce a conservative upper limit for $\Omega_{\mathrm{Ly}\alpha}$, we subtract estimates of the mass density in damped systems and stars from Ω_b. Of all the consitituents of Ω_b, these two are the ones most likely to represent local star forming regions at high redshift.

The value of Ω_{DLA} has been estimated using extensive quasar surveys both at high and low resolution. We use the measurements in Storrie-Lombardi and Wolfe (2000) for $2 < z < 3$, $\Omega_{\mathrm{DLA}} = 0.0009 \pm 0.0003 h_{70}^{-1}$. The stellar mass density Ω_* is much more difficult to measure since it is characterized in emission rather than absorption. Dickinson et al. (2003) have used IR photometry to directly integrate the total Ω_* contained in luminous Lyman break galaxies from the HDF. Their photometry corresponds approximately to rest-frame optical wavelengths, which should be less subject to dust extinction and/or bursting star formation than rest-frame UV measurements. They estimate a conservative lower bound of $\Omega_* \gtrsim 0.0002$ at $z \sim 2.5$, with their best estimate of the true value being a factor of 5 larger. Combining the most conservative estimate of Ω_* with the measured Ω_{DLA}, we find $\Omega_{\mathrm{Ly}\alpha} \lesssim \Omega_b - \Omega_{\mathrm{DLA}} - \Omega_* = 0.0446$, leading to the final constraint

$$0.92 \lesssim \frac{\Omega_{\mathrm{Ly}\alpha}}{\Omega_b} \lesssim 0.97, \tag{3.24}$$

assuming $h = 0.71$. Entering these values into Equation 3.22, the corresponding range for the galactic yield is

$$0.0015 \lesssim \ y \ \lesssim 0.0041. \tag{3.25}$$

In other words, typical galaxies in the early universe recycled $0.1 - 0.4\%$ of their input mass back into the IGM as heavy elements.

It is also interesting to compare the galaxy yield y with the stellar yield interior to the galaxy, y_*. The stellar yield specifies the amount of metals released into the galaxy's ISM, $y_* dM_*$ for each dM_* of stars formed. If we assume that a fraction f_{ej} of the metals formed in a given starburst are ejected from the galaxy into the IGM, we may crudely relate the stellar and galactic yields for a galaxy:

$$y(M_* + M_{\mathrm{ISM}}) = y_* M_* f_{\mathrm{ej}}. \tag{3.26}$$

Here, M_* and M_{ISM} represent the amount of mass within the galaxy locked up in stars and gas, respectively. These terms may be rearranged to produce the following expression:

$$f_{\mathrm{ej}} = \frac{y}{y_*}\left(1 + \frac{M_{\mathrm{ISM}}}{M_*}\right). \tag{3.27}$$

For bare stars, the ejected metal fraction is simply the ratio of the galactic and stellar yields; conversely, for galaxies with inefficient star formation more of the synthesized metals must escape in order to boost up the galactic yield. We saw in the previous section that most of the intergalactic enrichment is caused by relatively recent winds from star forming galaxies. Since high redshift galaxies

show evidence for preferential enrichment by Type II supernovae, we estimate y_* by integrating the supernova yields of Woosley and Weaver (1995) over an initial mass function, from $0.1M_\odot$ to $100M_\odot$. We have used various prescriptions for the IMF, including Salpeter (1955), Kennicutt et al. (1994), and Miller and Scalo (1979), which produce weighted yields ranging from $y_* = 0.001$ (Miller-Scalo) to $y_* = 0.011$ (Kennucutt). The yield in the solar neighborhood is approximately $y_* \sim 0.02$. We may set a conservative lower bound on $f_{\rm ej}$, using $y = 0.0015$ (Equation 3.25) and $y_* = 0.011$, with the result

$$f_{\rm ej} \gtrsim 14\% \left(1 + \frac{M_{\rm ISM}}{M_*}\right). \tag{3.28}$$

The actual value is probably at least twice this and possibly higher, since at earlier times less of the gas has been converted into stars. This could be mitigated to some extent if the high redshift IMF is extremely top-heavy, which drives up y_*.

Despite our crude models and large uncertainties, the overall impression is that galaxies at high redshift are quite efficient at returning the metals they produce to the IGM. On average, they will eject over $\frac{1}{10}$ of their nucleosynthetic byproducts. Such vigorous recycling suggests that much of the star formation in early galaxies occurred in bursts, rather than a more quiescent, gradual mode that would allow them to retain their metals.

Observations of local starbursts indicate that the yields and ejection fractions we derive are fairly reasonable for star forming dwarf galaxies. For example, the nearby dwarf NGC 1569 is driving a galactic wind that contains $\sim 34,000M_\odot$ of oxygen at $Z \sim Z_\odot$ (Martin et al., 2002). The parent galaxy has a combined $M_{\rm ISM} + M_* = 1 - 1.5 \times 10^8 M_\odot$. If we assume a solar mass fraction of oxygen relative to total heavy element mass (0.378), the implied yield for this galaxy is $y = 0.0007$ - roughly a factor of 2 below our lower limit for the high redshift yield. The authors also find that the wind carries away nearly all of the metals produced by the starburst, while the neutral gas disk holds ~ 5 times more oxygen from prior periods of quiescent star formation, implying a metal ejection fraction of $f_{\rm ej} \sim 20\%$ over the lifetime of the galaxy. We do not wish to overinterpret an isolated example when discussing the global properties of all galaxies in the early universe. We simply note that similar objects at high redshift could produce and distribute the quantity of heavy elements seen in the IGM, provided their wind velocities are high enough to efficiently mix debris over large scales.

3.5 Summary and Conclusions

We have presented new observations of O VI and C IV absorption at $z \sim 2.5$, which were used to estimate the metallicity distribution function of the intergalactic medium. Seven quasar sightlines were used to measure O VI for lines with $N_{\rm H\ I} \geq 10^{13.6}$; two of these with exceptionally high signal-to-noise ratios were also used to measure C IV for lines with $N_{\rm H\ I} \geq 10^{14.0}$. These limits probe densities

of $\rho/\bar{\rho} \sim 1.6$ relative to the cosmic mean. For each line in the samples, we estimated [O/H] and [C/H] by applying density-dependent ionization corrections to the measurements of $N_{\rm H\ I}$, $N_{\rm O\ VI}$, and $N_{\rm C\ IV}$. We experimented with several prescriptions for the ionizing radiation background, eventually settling on a model that produced the best match between the distributions of [O/H] and [C/H]. This model is dominated by quasar light with an original spectrum of $F_\nu \propto \nu^{-1.8}$, that has been reprocessed through the IGM, and normalized to a flux of $\log J = -21.5$ at the H I Lyman limit.

Our sample contains a mixture of detections and upper limits on the metallicity for each absorption line in the forest. The individual O VI and C IV lines are observed to scatter both above and below the trend of $[C, O/H] = -2.5$ observed in previous studies of the intergalactic metallicity, and several upper limits lie nearly an order of magnitude lower. Since the sample contains upper limits, we have used survival statistics to construct a Kaplan-Meier product limit estimate of the [O/H] and [C/H] distributions within the Ly-α forest. For the O VI distribution, we carefully corrected for the effects of false positive identifications that might result from interloping H I lines in the Ly-α forest. Our basic results may be summarized as follows:

1. The mixture of heavy elements within cosmological filaments does not differ qualitatively in regions of high and low density (for roughly $1 \lesssim \rho/\bar{\rho} \lesssim 100$). We have not observed any significant variation in the [O/H] or [C/H] distribution that correlates with $N_{\rm H\ I}$.

2. Roughly 30% of lines in the Ly-α forest are enriched to abundances below $[C, O/H] \lesssim -3.5$. Thus we have not detected evidence for a metallicity floor in the IGM. If such a floor exists, extrapolation of the cumulative abundance distribution suggests it would lie in the range $-5 \lesssim [C, O/H] \lesssim -4$, about a factor of 3 lower than the limits probed by our survey. Nevertheless, some portion of the cosmic volume is very metal poor, even in regions with $\rho/\bar{\rho} \sim 10$.

3. The median abundance of the filaments is $[C, O/H] = -2.82$. By differentiating the cumulative abundance distribution, we obtain the probability density for [O/H] and [C/H], though we cannot construct the lowest metallicity portion of the distribution with our data. For the $\sim 70\%$ of lines which we do measure, the distribution may be approximated as a gaussian with mean $\left\langle \frac{O}{H} \right\rangle = -2.85$ and $\sigma = 0.75$ dex. The distribution of $Z/Z_\odot$ is therefore lognormal, with mean $\left\langle \frac{Z}{Z_\odot} \right\rangle = 10^{-2.2}$.

It is also instructive to express our results in terms of an enriched mass function, defined as the cumulative mass fraction of the universe that is enriched above a given abundance level. We place upper and lower bounds on the EMF by assuming either that the abundance pattern observed at $\rho/\bar{\rho} \geq 1.5$ extends to arbitrarily low density, or that we have detected all heavy elements and that lower density clouds are chemically pristine. If the true pattern lies between these two extremes, then $\sim 50 - 60\%$ of all baryons in the universe have been enriched to $[C, O/H] \geq -3.5$ by $z \sim 2.5$. We have not calculated similar constraints for the enriched volume fraction, since even at these low

column densities we only probe $\sim 5\%$ of the spatial extent of the universe. Generally, then, our conclusions apply to the gas found in cosmic filaments at $z \sim 2.5$, where most of the mass resides. We have not yet reached the voids which contain most of the cosmic volume.

We have examined our measurements in light of two established models for cosmic chemical enrichment. The first model describes metal production from the Population III stars postulated to form at $z \geq 30$ from H_2 cooling, and the second describes metal-laden superwinds that are driven from starburst galaxies at more recent epochs. Comparison of these models with our data suggests that Population III stars do not produce enough metals to enrich the cosmic filaments at observed levels.

Models incorporating galaxy outflows similar to those seen at low redshift *can* reproduce the observed average intergalactic metallicity. The significant scatter observed towards low $Z/Z_{\odot}$ indicates that there may be local variations in the frequency or efficiency of these winds. Yet it seems likely that the models will be able to match these trends given proper tuning. The wind models predict a substantial decrease in the average metallicity at H I densities slightly below the threshold of our survey. The measurements presented herein do not have sufficient sensitivity to detect this decline; pixel-statistical methods may improve on this in the near future, and long term prospects may include searches for intergalactic O VII and O VIII , which are the dominant ionization species at these densities.

To find regions of the universe whose metals are derived from Population III stars, it will be necessary to survey the cosmic voids. However, if Population III star formation is significantly biased then it is possible that the underdense IGM could remain nearly chemically pristine. The chemical enrichment of cosmological filaments is dominated by the debris of galactic outflows, and therefore must have taken place relatively recently. Taken together with our estimates of the enriched mass function, this indicates that roughly half of all baryons have either been processed through a galaxy or mixed with material that has done so in the first 3 Gyr after the Big Bang.

Finally, we present a simple closed-box model of the chemical evolution of the universe. We use this model along with our metallicity measurements to estimate the average metal yield of galaxies prior to $z = 2.5$. For a galaxy, the metal yield is determined in part by the star formation rate and raw stellar yields, but also by the efficiency with which outflows can expel metals from the galaxy's gravitational potential. We find that the typical galaxy ejects $\sim 0.1 - 0.4\%$ of its formed mass into the IGM as heavy elements. This amounts to at least $\gtrsim 14\%$ of the total quantity of metals synthesized within these galaxies. These yields are not qualitatively different from what is seen in some local dwarf starburst galaxies.

Appendix A

Comparison with Other Recent O VI Surveys

Since the publication of Chapter 2, two groups have reported on similar searches for O VI at $2 \lesssim z \lesssim 2.5$ using data from the VLT/UVES spectrograph. Carswell et al. (2002) observed O VI absorption towards the quasars HE 1122-1648 and HE 2217-2828, and found 24 systems in the two sightlines (recall that we found 12 intergalactic systems in 5 sightlines). Their higher discovery rate appears to reflect different selection criteria. The UVES sample was designed to detect as many O VI lines as possible, while ours from Chapter 2 was designed to minimize contamination from interloping Ly-α lines. It is nearly impossible to produce an O VI sample that is both complete and uncontaminated, so Carswell's approach forms an important complement to our work in Chapter 2. We have also addressed this issue by studying a fairly complete but heavily contaminated sample of O VI systems in Chapter 3.

The search strategy in Carswell et al. (2002) was to "try O VI in all possible cases and retain it as a reasonably firm identification when a physically self-consistent fit [could] be obtained." Their cleanest identification (at $z = 2.180$ in HE 2217-2818) resembles the systems described in Chapter 2, and contains a mixture of O VI, C IV, C II, Si IV, Si III, and Si IItogether with strong H I ($N_{\rm H\ I} = 10^{15.7}$). Their remaining O VI lines are all similar to the *bd* systems from Chapter 3, where one of the O VI components is dominated by blending from the Ly-α forest. The authors estimate their fraction of false positives at $\sim \frac{1}{3}$ of their sample of 24 lines. Our calculations in Chapter 3 suggest that this may be somewhat optimistic, although the UVES sample is at slightly lower redshift, where the Ly-α forest is thinner.

Bergeron et al. (2002) also published preliminary results of a UVES O VI search at $z \sim 2.2$ in the quasar Q0329-385. They identify 7 intergalactic systems in this single sightline. At least two of these are very convincing examples of *photoionized* O VI, since the lines are too narrow to admit the temperatures required for collisional O VI production. These systems are clearly different from what we have found in Chapter 2, and may well represent enriched, photoinionzed cosmic filaments. The

authors are compiling a sample of $\sim$ 20 quasar spectra to study O VI absorption; analysis of these spectra and the other 5 systems from Q0329-385 (not described in their preliminary paper) should reveal whether the UVES data contain more examples of photoionized O VI.

Both Carswell et al. (2002) and Bergeron et al. (2002) limit their discussion of the O VI physical environment, using the subsets of their samples that are conducive to ionization modeling. CLOUDY is most straightforward for photoionized systems, and these papers place special emphasis on the absorbers that fit this interpretation. As was shown in Chapter 2, the stonger, collisionally ionized systems contain several gas phases at different temperatures, and are quite difficult to model with confidence. Neither we nor Carswell et al. (2002) found any systems that clearly *required* photoionization models like the two best systems described in Bergeron et al. (2002). However, the majority of the systems described in Chapter 3 and Carswell et al. (2002) are at least *consistent* with photoionization. There are probably many of these systems hidden amongst the Ly-α forest lines; only chance can dictate when clean examples like those in Bergeron et al. (2002) will be observed. Our results suggest that this should be a rare occurrence. However, even a few such systems remind us that O VI arises in varied environments at high redshift, and that systems must be examined on a case by case basis before their nature can be determined.

Appendix B

A Note on Models for the UV/X-Ray Ionizing Background

The models used in Chapter 3 for the metagalactic ionizing background spectrum were provided to us by F. Haardt, using his CUBA package. This software performs calculations similar to those described in Haardt & Madau (1996), with some new features. The basic principle is to integrate the best available redshift-dependent luminosity functions from the literature to create an average source spectrum of galaxies and quasars at each redshift. Then, the photons are statistically propegated through the a parametrized model of the IGM to simulate absorption and reemission at important ionization edges. The newer models extend the range of the original Haardt & Madau (1996) spectra by including the X-ray background, which turns out to be quite important for O VI in the low-density IGM. We have already described in Section 3.3 some of the uncertainties in the UV portion of the spectrum (e.g. the range in measurements of the spectral slope α) and their effects on our results.

The model for the X-ray background is calculated independently from that of the UV/optical light in the new models. It is assumed to originate only from AGN, and its source function is calculated by integrating the X-ray luminosity function at each redshift. This function is assumed to evolve independently of the optical/UV LF, and its redshift-dependent form is taken from Boyle et al. (1993). Seyfert I galaxies contribute flux at all X-ray wavelengths, since the IGM is exposed to the bare X-ray flux from the central AGN engine. The core of Seyfert II galaxies is covered by an obscuring torus which absorbs soft X-ray photons but transmits hard X rays ($E \gtrsim 1$ keV). The hardness of the X-ray background is thus sensitive to the relative numbers of Seyfert I and II galaxies at each redshift.

The UV/X-ray background models use weighted combinations of Seyfert I and II X-ray spectra, constructed as described in Madau et al. (1994). The evolution in number ratio of Seyfert I / Seyfert II galaxies is estimated by assuming that AGN with B-band luminosity above a given threshold are always Seyfert I, while those below are Seyfert II. This is normalized to locally observed Type I/Type II fractions. The models match observations of the UV and hard X-ray backgrounds at

low redshift, within errors (Haardt & Madau, 2001). The local soft X-ray background is less well constrained, partly because of galactic foregrounds. This range turns out to be most important for our O VI results.

At $z \sim 2.5$, the UV/optical luminosity function is near its peak value over the history of the universe. Since the models calculate the Type I/Type II AGN fraction based on optical flux, this means that nearly all the AGN at this redshift ($> 95\%$) are counted as Seyfert I, and the soft X-ray background is quite high. The models are still uncertain, but it seems more likely that the soft X-ray backgrounds used here would err on the high side rather than the low, since essentially no dilution by Type II AGN is included at these redshifts. This affects our results in the sense that a lower soft X-ray flux will enhance O VI production, as described in Appendix C.

We have performed the entire analysis for several models of the ionizing background, retaining the HM1.80 model with $\log J_{912} = -21.5$ since this produces the best match between the observed [O/H] and [C/H] distributions. The other models we tested included HM1.50 and HM1.55 slopes, with normalizations of $\log J_{912} = -21.1, -21.4, -21.5$, and -21.6. Our optimal normalization is similar to the Haardt & Madau value. It is slightly lower than estimates of J_{912} made using the proximity effect at similar redshifts, though the discrepancy is only at the $\sim 1\sigma$ level. The field of X-ray population modeling at high redshift is rapidly evolving with the comprehensive surveys being undertaken by XMM and Chandra, and much better models of the high redshift X-ray background should be forthcoming in the near future.

Appendix C

Effects of the X-Ray Background on Derived Oxygen, Carbon Abundances

It is seldom appreciated that for densities below $N_{\rm H\ I} \sim 3 \times 10^{14}$, the Oxygen in the IGM is actually *over*ionized relative to O VI - most atoms are in the O VII and O VIII states (See figure 4). In photoionization equilibrium, the density of O VI is governed according to the equation

$$n_{\rm O\ VI} \int_{138{\rm eV}}^{\infty} \frac{4\pi J(\nu)\sigma(\nu)}{h\nu} d\nu = n_e n_{\rm O\ VII} \alpha(T), \tag{C.1}$$

and likewise for other ionization states. Since at low densities $N_{\rm O\ V} \ll N_{\rm O\ VII}$, much more O VI is produced by recombination from O VII than photoionization of O V . Accordingly, the abundance of O VI is determined by the number of O VII ions available for recombination. At low densities, O VII and O VIII are found in similar proportions and their ratio is sensitive to the background flux at the O VII $\rightarrow$O VIII ionization edge. This ionization energy is in the soft X-ray band (739eV, or 17Å, indicated in Figure 3), which leads to the counterintuitive result that the intergalactic O VI abundance is critically sensitive to the intensity of the soft X-ray background at low densities. A decrease in the soft X-ray background favors a higher O VII abundance, and hence actually *enhances* O VI .

At densities above $N_{\rm H\ I} \sim 3 \times 10^{14}$, most oxygen is in either the O VI or O VII state. The ionic balance is then governed by the intensity of the UV background at the O V $\rightarrow$O VI and O VI $\rightarrow$O VII ionization edges (109.5Å and 89.5 Å, indicated in Figure 3). In this regime, a decrease in the background results in fewer photons with sufficient energy to create O VI , thus lowering the predicted O VI column densities. Thus *a decrease in the X-ray background flux will result in lower metallicities for our lowest density lines, but the higher density lines will remain unchanged. This net effect would be a dropoff in metallicity for regions below below* $\rho/\bar{\rho} \sim 3$ *(*$N_{\rm H\ I} \sim 10^{14}$*).* Our best current models do not find this trend, but the reader should bear in mind that a significant revision

of the X-ray background at $z \sim 2.5$ could affect this result.

Appendix D

The Large-Format Camera: A Wide-Field Imager for the Hale Telescope

D.1 Introduction

Over the past decade, an increasing number of nights on the 200 inch Hale Telescope (hereafter, the P200) have been allocated for deep imaging observations—particularly as the Keck telescopes have absorbed much of the heavy spectroscopic load. Many of these P200 programs require fast, deep exposures covering large areas of sky. A few such programs within the Palomar community include:

- Surveys for high redshift galaxies and quasars
- Searches for gamma-ray burst optical afterglows
- Imaging of galaxy clusters
- Surveys for globular clusters in the extended haloes of massive galaxies
- Support observations for space based observatories or key projects (e.g., GALEX, SIRTF/SWIRE)
- Surveys for Kuiper Belt objects.

The principal existing imager for the P200 (COSMIC; Kells et al., 1998) covered a 9×9 arcminute field. However, because the prime focus was originally used for photographic observations, its optics were designed to correct a significantly larger field of view. As affordable, edge-buttable CCDs in 2048×4096 format began to enter the market in the mid-1990s, it became possible to cover the entire focal surface of the P200 with science grade detectors. In June 1998, Mark Metger and I began designs for the Palomar Large-Format Camera (LFC)—a mosaic CCD instrument with the following desired properties:

1. The science detectors should properly sample the entire $24'$ diameter field of the P200 prime focus.

2. The UV throughput should be as high as possible.

3. Exposures should be uniform across the field, and allow short enough times to permit calibration of arbitrary filter sets using bright spectrophotometric standard stars.

4. The CCD array readout should be fast enough to maintain a high duty cycle for the instrument.

5. The systems should be durable enough to withstand public use.

Our final design contains a mosaic of 6 CCDs, covering a field approximately 24 arcminutes in diameter. The project had a significant head start, as we opted to use the existing wide-field corrector, eliminating the need for custom optical design and lens fabrication. The design and construction of the imager with related mechanical assembles were all completed within ~ 1.5 years (from the beginning of design to first light) by the team listed at the end of this Appendix. Further mechanical design iterations and CCD repairs were required for the next $\sim \frac{1}{2} - 1$ year before the instrument was released for fully public use. Since January 2001, the camera has been the principal optical imager for the observatory, logging some 200 nights on the telescope. Its design is competetive with other wide field imagers at major observatories. At commissioning the P200 was the largest aperture telescope (5m) to be outfitted with a wide field camera. Several smaller telescopes were already using dedicated imagers with larger fields (KPNO/CTIO MOSAIC cameras at 4m$\times 36'$ square, and CFHT 12K at 3.6m$\times 42' \times 28'$). However, the initial aperture advantage of the P200/LFC was largely offset the by poorer seeing conditions at Palomar relative to Kitt Peak and Mauna Kea. Since its commissioning the P200/LFC has been surpassed in aperture by the Subaru SUPRIME-CAM (8.2m$\times 34' \times 27'$), which will soon be joined by Magellan/IMACS (6.5m$\times 27'$ square).

In the following sections, I descibe the basic components and functionality of the LFC, and briefly discuss its performance since commissioning.

D.2 Optical Elements, Vignetting, and Image Distortion

The primary mirror of the P200 is figured as a paraboloid rather than a hyperbolic Ritchey-Chretian element; the prime focus corrector for this design consists of four all-spherical elements, and is described in detail in Wynne (1967) and shown in Figure D.1. The incoming f/3.34 beam from the primary is slowed slightly to f/3.52 at the image plane, which is shown at far right. The last element before the focal plane in the diagram is the dewar window, which posseses no optical power. The

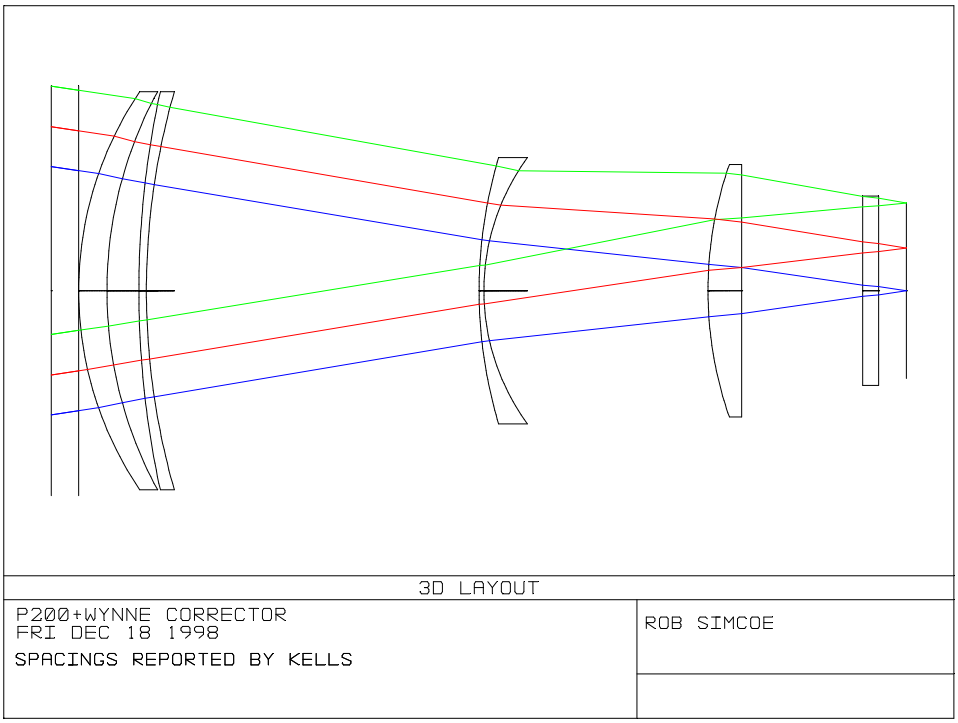

Figure D.1 Optical layout of the P200 Wynne corrector.

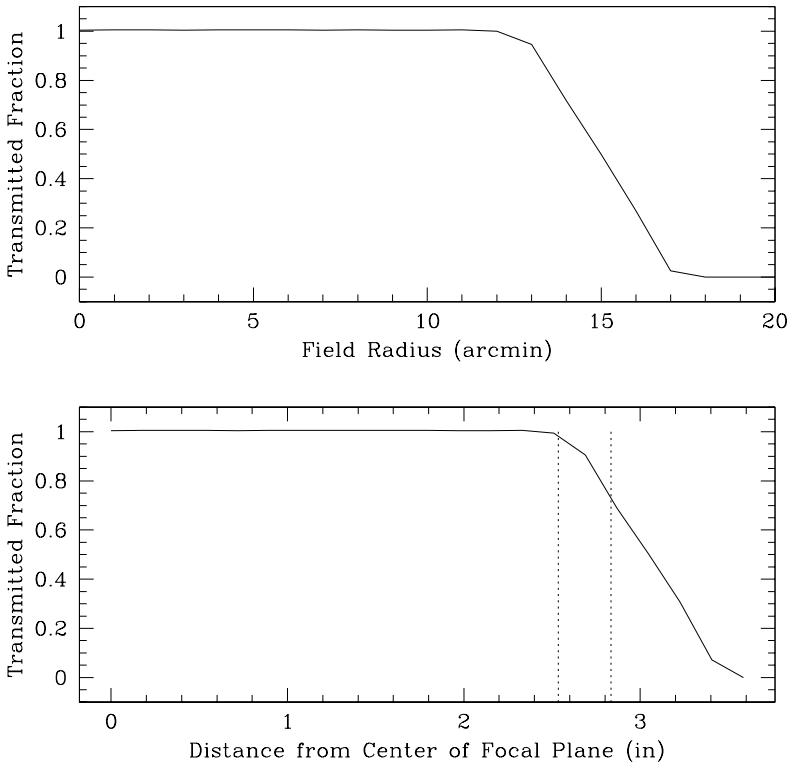

Figure D.2 Vignetting profile of the Wynne Corrector, as a function of distance from the center of the focal plane, and angle on the sky from the pointing center. The left vertical dotted line indicates the radius whhere the beam begins to contact the edge of the mosaic (the innermost circle in Figure D.3); the right line shows the radius of the outermost ray that contacts the mosaic (the outer circle in Figure D.3).

filters (not shown) are located between the last corrector element and the window, and also have no optical power.

The corrector's field of view is limited by the design of the P200 prime focus cage, which constrains the size of the first lens to be less than 28 cm unless substantial modifications are made to the cage structure. The three incoming beams shown in Figure D.1 correspond to sources at field angles of 0, 6 and 12 arcminutes. It can be seen from the figure that for field angles larger than $\sim$ 12 arcminutes, the lens housing for the first corrector element (indicated by a vertical line at the far left of the Figure) begins to vignette the beam. Figure D.2 presents a more detailed theoretical calculation of the vignetting as a function of field radius/angle.

The LFC detectors are approximately inscribed within the 24 arcminute circle defined by the unvignetted beam. The spatial orientation of the CCDs relative to the beam is shown in Figure D.3, where the innermost circle represents the full unvignetted area at focus. Most but not not all of the science area is fully illuminated; the most extreme field radii on the science detectors

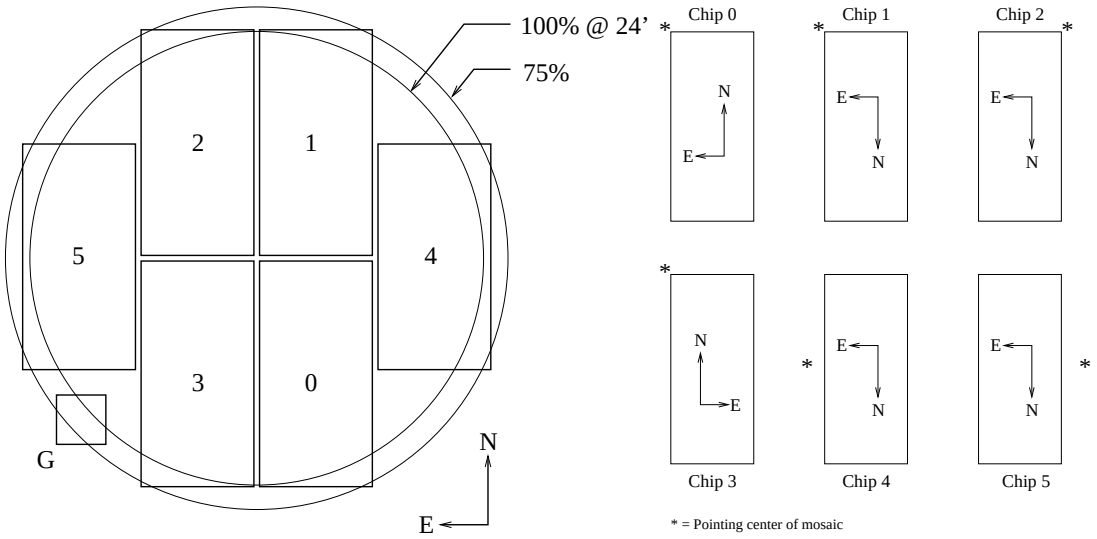

Figure D.3 Left: Orientation of the LFC focal plane on the sky, showing the relative positions and index numbers of all 6 science CCDs plus the guider. The inner circle indicates the unvignetted portion of the beam; the area enclosed by the outer circle recieves $\approx 75\%$ transmission. Right: On-screen display orientation of the six CCDs after readout. Since the CCDs have different amplifier configurations, their image display noes not always default to the cannonical "North-up East-left" orientation.

(shown with the outer circle in Figure D.3) experience a light loss of $\approx 25\%$. The shadowing is more severe for the guide CCD, which samples a 2.3×2.3 arcminute field in a notch of the cross-shaped pattern of science chips. The corner of the guide field closest to the telescope's pointing center is fully illuminated, but a vignetting loss of $\sim 50\%$ can be seen at the far edge of the field. In practice, one rarely has trouble locating a suitable guide star given the field size and sensitivity of the guide CCD. A notable exception is at high galactic latitude in the u' band. The lower density of stars and lower sensitivity of the guide CCD in this range sometimes force users to adjust their pointings to include a nearby bright guide object.

The Wynne corrector is designed to minimize coma and spherical abberation at the focal plane, but significant residual abberations remain (principally field curvature), causing astrometric and morphological distortions toward the edge of the field. In Figure D.4 we present spot diagrams for point sources at field angles of 0 (left) 6 (middle) and 12 (right) arcminutes, using colors roughly equivalent to Sloan $r'$and i'. We generated the spots using the ZEMAX ray tracing package, based on lens specifications from W. Kells (recorded in an Observatory Memorandum). The scale bar at left corresponds to 40μm, equivalent to 2.67 pixels or 0.48 arcseconds, and the focus has been optimized for objects at intermediate field angles.

While it is generally possible to obtain sub-pixel spot sizes over the inner $\sim 15 - 18$ arcminutes of the array, at larger angles the spots are stretched over several pixels in the radial direction, with nearly 2:1 axis ratios at the field edge. These spot diagrams represent a best-case scenario for the

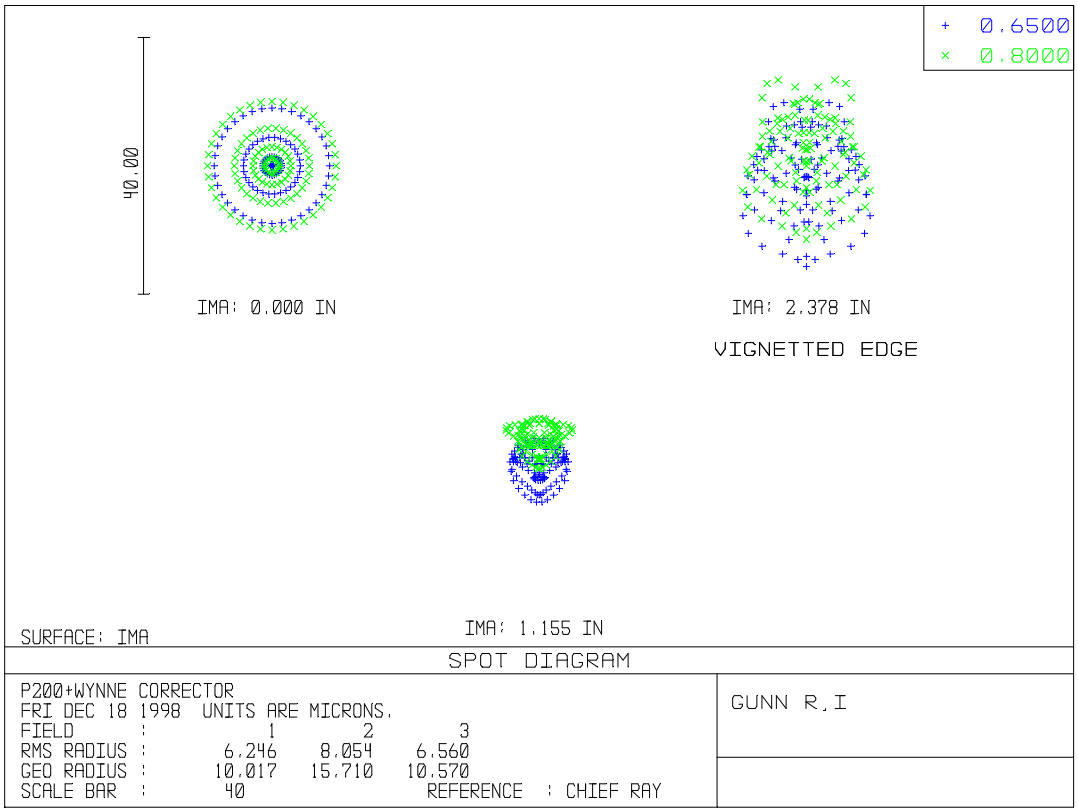

Figure D.4 Spot diagrams for the Wynne corrector at wavelengths approximating Sloan r'(blue) and i'(green).

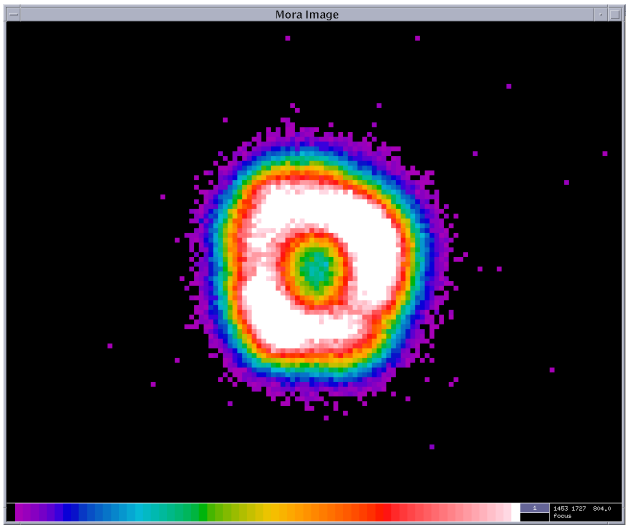

Figure D.5 Defocused star image taken through LFC mounted on the P200, illustrating primary mirror pinch.

optical design. In practice, the image degradation is exacerbated by alignment errors and mechanical flexure of the optics and telescope. For the P200 the most significant wavefront errors appear to be caused by problems with the primary mirror support structure, often called "mirror pinch." This is illustrated in Figure D.5, where we show a defocused stellar image from the LFC (the exposure is long enough to average out distortions due to seeing). A precisely figured primary would result in a pupil image that is perfectly round and uniformly illuminated. Clearly the optics have significantly distorted the incoming wavefront: the sense of these distortions varies with the telescope's gravity orientation and load.

D.3 Detectors and Electronics

The science field of LFC is populated with a set of six 2048×4096 SITe ST002A CCDs. These devices are thinned, backside illuminated, and AR coated to enhance their UV throughput. Their 15μm pixels subtend 0.18 arcseconds on the sky, so the focal plane is significantly oversampled for typical seeing conditions at Palomar (0.9-1.3" FWHM). The plate scale was essentially fixed by the design of the Wynne corrector and the CCD pixel size; reimaging to a coarser plate scale would only result in more dark silicon since the whole 24 arminute field presented by the corrector is covered. Often the array is operated in 2×2 binned mode, but on occasion we have experienced seeing of 0.5 arcseconds FWHM in i', so the fine sampling is sometimes useful. A single amplifier is used for readout on each CCD. In unbinned mode, the time required for a full mosaic read and disk storage is 115 seconds; in binned mode this reduces to 56 seconds. Residual charge on the mosaic is wiped before each exposure, requiring $\sim$ 5 seconds overhead between the expose command and the first

firing of the shutter.

The focal plane houses two additional 512×512 pixel scientific grade CCDs (SITe model SI502A). One of these is used for guiding, the other was to be used for active focusing, but is not wired within the dewar. The guider is located behind the shutter and filter, and is paused during readouts of the science array to prevent electronic crosstalk. Some crosstalk is seen between the readout channels of the science arrays, though this can be corrected using standard data reduction techniques.

The CCDs are driven by a set of Leach-II electronics (Leach et al., 1998) mounted in an enclosure on the side of the dewar. We have used a slightly modified version of the standard Leach-II power supply, where the 5V line used for digital circuitry is supplied by a separate external source from the analog 15V and 40V lines, in order to reduce the operating temperature of the analog supply. Besides the clock drivers, analog-to-digital conversion, and communications boards, the Leach-II system contains a "utility" board that may be used for temperature and shutter control, and a variety of other functions. For LFC, the utility card is primarily used to report on the status of position sensors located inside the mechanical assemblies of the shutter and filter wheel. The lines coming from the sensors are opto-isolated from the CCD electronics to prevent the introduction of electrical noise, since the CCD power source is independent from those of the motors and sensors.

The data, sensor information, and communication information are transmitted via fiber optic link from the prime focus cage to the LFC host computer, a dedicated Sun Ultra 1 workstation located in the P200 server room (immediately below the data room).

D.4 Mechanical Design

Because the LFC is only used for imaging, its design requirements are relatively straightforward. The limiting constraint in the design of the large mechanical components was the total distance from the last element of the Wynne corrector to the focal plane—only 4.3 inches. This sets the total thickness of the intervening mechanical assemblies, including the shutter and filter wheel.

D.4.1 Dewar/Focal Plane

The LFC dewar was custom built according to a design that is fairly standard for large mosaic cameras. A gold plated copper cannister (manufactured by G. Luppino at GL Scientific) containing 10L of liquid Nitrogen is suspended in an evacuated Aluminium chamber using G10 fiberglass standoffs. Copper straps are run from the LN2 can to the mounting packages of each of the 6 individual CCDs. The temperature of the entire focal plane is monitored through a series of thermistors and resistors bonded to the focal plane mounting surface. The thermal control loop is run by a Lakeshore (TM) temperature controller which is external to the dewar and mounted on the side of the P200 prime focus cage. The hold time for the dewar is slightly over 25 hours, so Nitrogen fills are required only

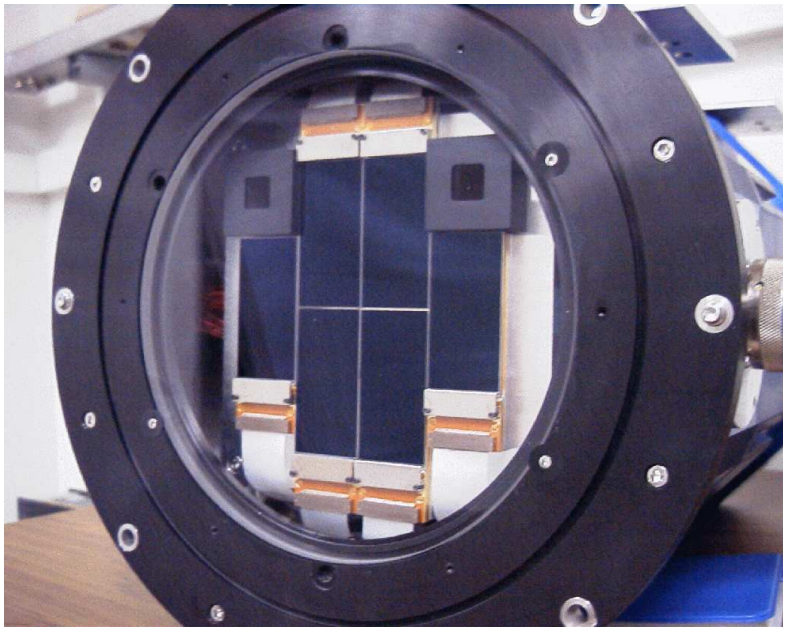

Figure D.6 View of the LFC focal plane through the dewar window.

once a day.

The active silicon for the ST002A CCDs is bonded to an invar packaging substrate that provides a set of threaded holes for mechanical mounting purposes. The RMS flatness of the devices is generally quite good, but in many cases there exists an edge-to-edge gradient of order 10μm created in the process of bonding the CCD to the mechanical mounting package. Therefore, the individual CCDs each need to be tilted slightly to ensure a planar imaging surface across the entire mosaic.

This was accomplished by bolting all of the CCDs to a single, precision ground, flat reference surface. The actual CCDs are mounted upon custom designed aluminum backplates, each of which also attaches to a cold strap on the face opposite the detectors. The backplates are then bolted to the reference flat, using a set of small individually ground spacer washers to compensate for tilt inherent to the CCDs. A set of rectangular holes machined in the reference flat prior to the grinding operation provide a pathway to route the cold straps from the CCDs through the mounting plate to the LN2 can.

This low order tilt compensation works fairly well, although observers have reported that the optimal focus varies somewhat across the field, particularly in the outer portions of the image plane. This is caused partly by field curvature, and partly by the fact that two of the outermost CCDs were installed after the 4 central chips, and have less accurately ground spacers. This represents a possible path for improvement in future servicing of the instrument. However, it involves a major disassembly of the enrire dewar and focal plane—in other words, a fairly risky operation.

The package design of the ST002A CCDs results in gaps of $\sim$ 15 arcseconds between the active imaging areas of adjacent CCDs on the mosaic.

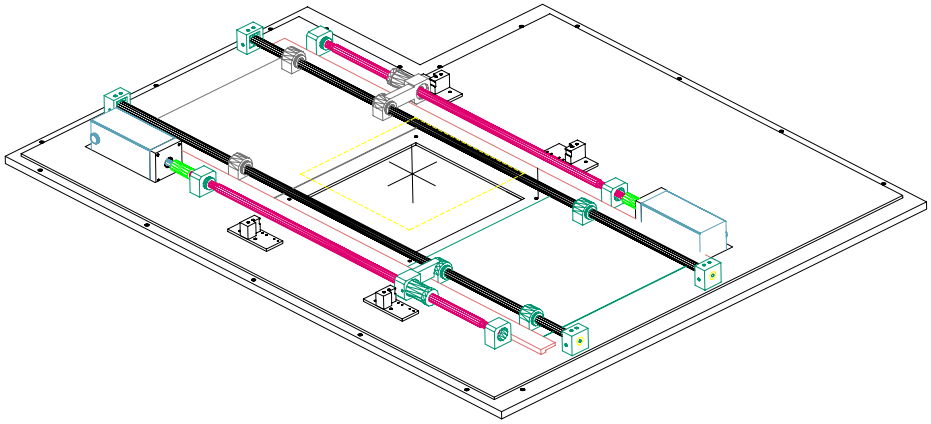

Figure D.7 Schematic of the LFC shutter assembly. The beam enters from below, through the aperture centered on the cross at middle. The two blades slide right and left along a set of rails (shown in black). They are driven by high pitch lead screws (red) coupled to small, high torque motors (blue). The shutter is shown in open configuration.

The guide CCD is also cooled, and bolted to the focal plane reference surface roughly 500 arcseconds South and 600 arcseconds East from the mosaic center. Its pixels are 24μm square, subtending ≈ 0.54 arcseconds at the edge of the LFC field. The field of the guider is 138 arcseconds square. The guide CCD's mounting package is not edge buttable, so the offset between the science and guide fields is fairly large. Also, the guide and focus devices were mounted to locate their imaging surfaces on the same plane as that of the science CCDs. This placed a portion of the SI502A packaging slightly above the active region of the science array, creating a potential scattered light problem for the science detectors (since the SI502A packaging is quite shiny). To reduce internal reflections, the the guide and focus chips were shrouded with small aluminium baffles (painted flat black and subsequently baked and tested in vacuum).

D.4.2 Shutter

The LFC utilizes a custom-built fast focal plane shutter with a double blade design. It is bolted to the bottom face of a thin enclosure which also contains the filter wheel (a view of this bottom face is shown in Figure D.7). The rectangular blades are constructed of 0.030" thick carbon fiber plates. With the shutter closed, one of the two blades entirely covers the incoming beam. The shutter is opened by sliding the occulting blade away from the aperture, and at exposure termination the second blade closes behind the first in the same direction. Both blades are driven along a set of rails at constant velocity, by high pitch lead screws coupled to brushless servo motors. This design allows for independent, extremely rapid position control of the two blades with minimal noise and vibration, and eliminates the need for potentially destructive mechanical hard stops. Also, it provides extremely uniform exposure times across the entire focal plane.

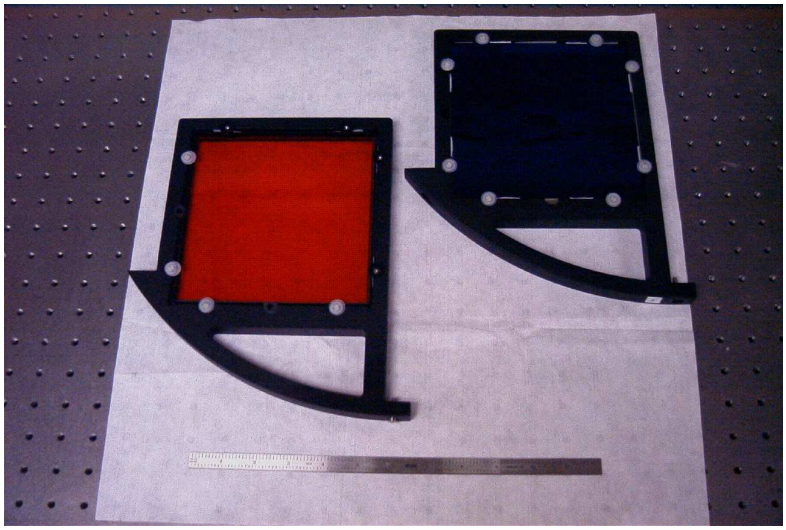

Figure D.8 Two LFC filters mounted in their handling cartridge assemblies. Each filter has 6.1 square inches of clear aperture.

The shutter blades are generously oversized relative to the beam to minimize light leaks; extensive baffling both within the shutter mechanism and on the blades themselves further protects against potential leaks.

The positions of the shutter blades are monitored before and after each firing by a set of hall effect sensors within the shutter enclosure. Because of the high speeds involved and the potential for damage to the mechanism, both blades are required to be in a known and "legal" position before either can be moved (e.g., if blade 1 is in the beam, blade 2 cannot also be moved into the beam). The combination of shutter speed and sensor response time sets a lower limit of $t = 0.6$ seconds on LFC exposures. The exposure time accuracy has been measured using standard stars, and is both accurate and repeatable to better than 6 ms RMS (1%) for exposures above this limit.

D.4.3 Filter Wheel

The LFC is outfitted with a set of Sloan u', g', r', i', z' filters. In addition, privately owned R_s and I and several narrowband filters are available for use. Four filters may be simultaneously mounted in the instrument; these reside in a wheel housed in the same enclosure as the shutter. The individual 6.1" square filters are permanently mounted in specially designed cartridges for ease of handling (see Figure D.8). These cartridges slide into the filter wheel through a port in the side of the shutter/filter wheel enclosure.

The wheel itself is friction driven, via a small tire that is spring-loaded against its outside diameter. The tire is geared down to a stepper motor mounted on the exterior of the shutter/filter wheel enclosure. The surface of the wheel which contacts the tire is a continuous knurled ring, and is located immediately below the plane of the actual filters.

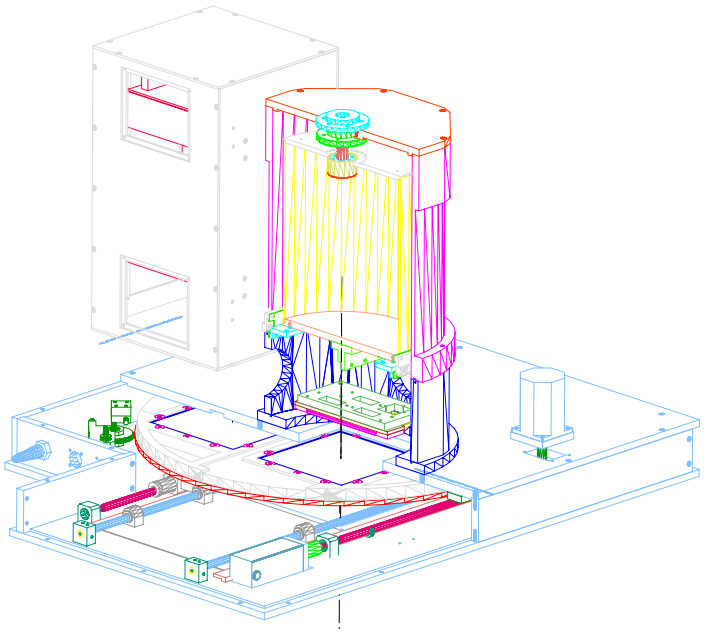

Figure D.9 Cutaway of the total LFC mechanical assembly. Shown are the shutter (partly visible at bottom), and filter wheel (gray disk partly visible at the top of the cutatway structure), and a cross section of the dewar with focal plane (shown in green) and the LN2 can (in yellow). The electronics enclosure is also shown mounted on the side of the dewar.

Filter moves are executed in open loop fashion, and when the filter is near a fiducial position a series of hall sensors is used both to determine which filter is in the beam, and also to achieve fine positioning of the wheel. A spring-loaded detent mechanism was built into the design, incorporating a swinging lever arm to lock a ball bearing into four notches at the cardinal points on the inside diameter of the knurled drive ring. However, when the detent mechanism was loaded enough to provide sufficient holding torque, it caused unacceptable slippage in the friction drive during filter moves. Plans were developed to disengage the detent arm during moves using a solenoid, but these were never implemented due to time constraints at commissioning.

In the current scheme, the detents are not used, and the wheel is simply fixed in place by the holding torque of the stepper motor. This torque should be quite small due to the large gear ratio between the filter wheel and stepper. From a design standpoint, the filter mechanism would clearly be improved by a repeatable mechanical definition of its four positions. This would allow the stepper to be turned off between moves, and minimize wobbling due to hysterisis in the gear mechanism. In practice though, users have been quite satisfied with the positional accuracy of the wheel; no problems with LFC's flat fielding properties have been reported, even after extensive tests by the mountain staff.

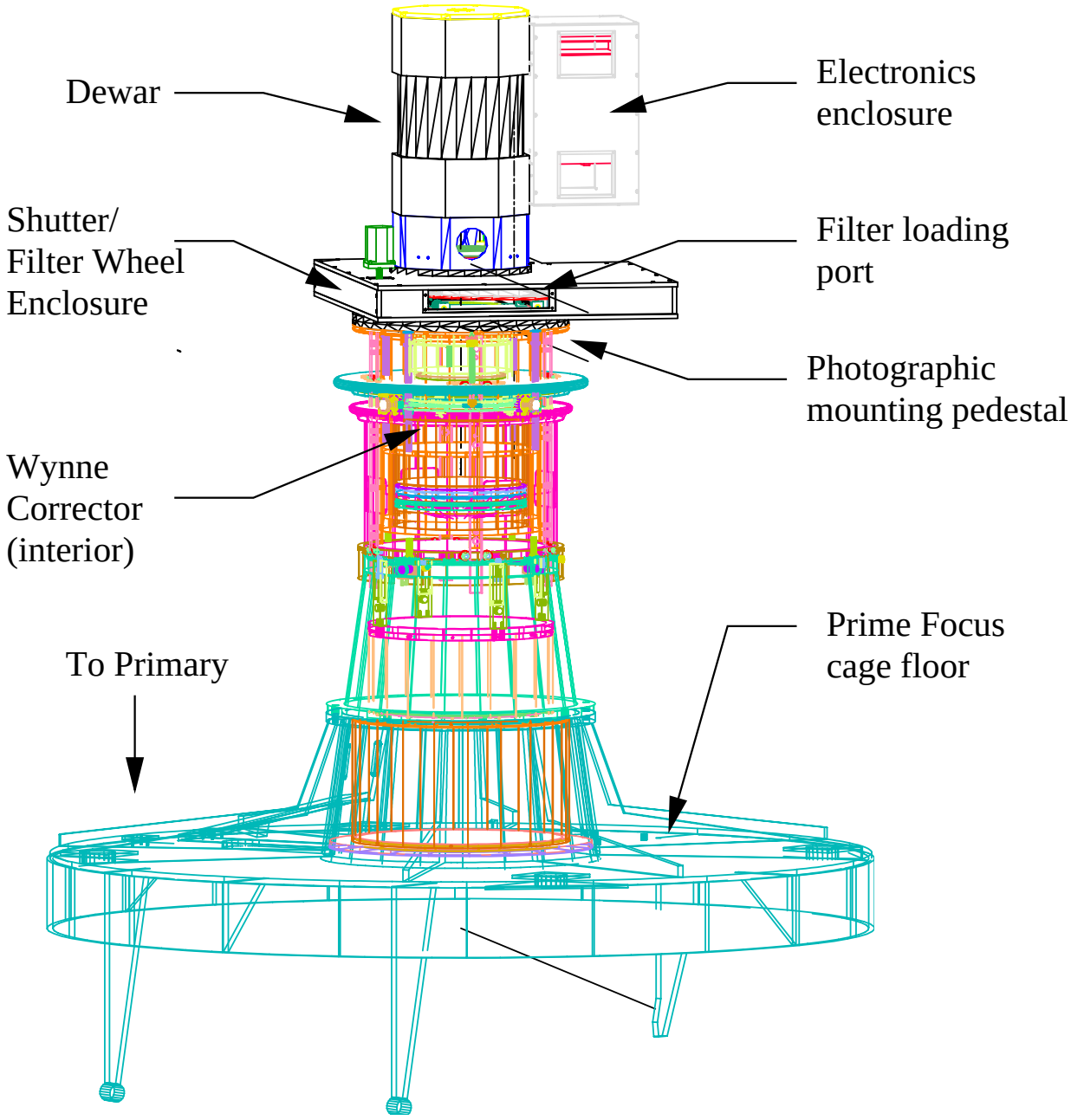

Figure D.10 LFC mechanical model mounted on the P200 prime focus pedestal. The Wynne corrector is mounted on the inside of the pedestal.

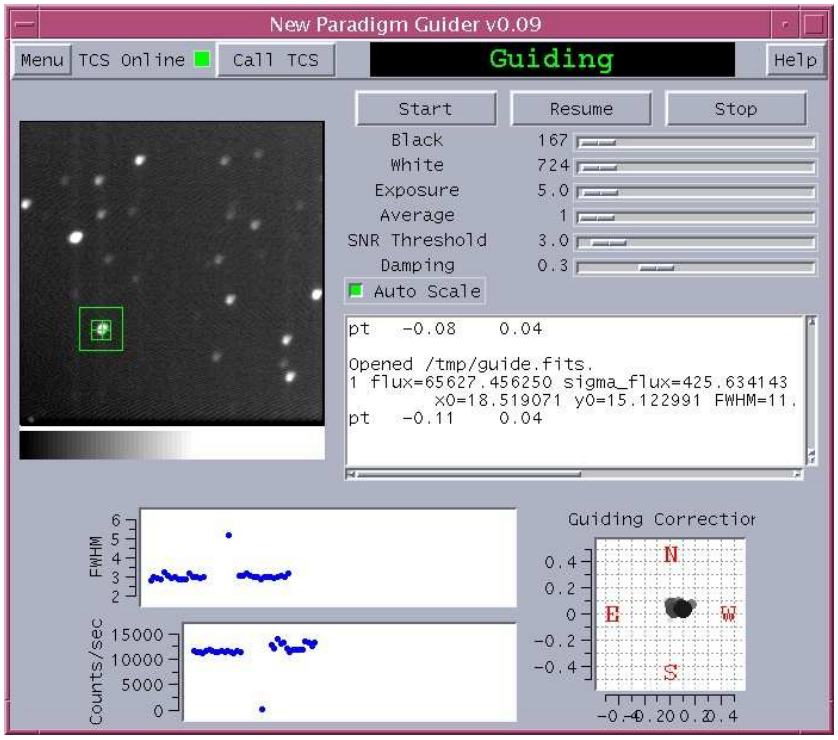

Figure D.11 Screen shot of the LFC guider.

D.5 Instrument Control

The coordination of all instrument functions is controlled by a dedicated host computer, which operates a software package ("mcdcom") designed by M. Metzger for running mosaic CCD cameras. The software communicates over three separate channels with the instrument. One runs the CCD electronics (over the fiber optic link), one runs the motor controllers (over the serial port), and one communicates with the P200 telescope control system (TCS, over the local intranet). Within the instrument itself, the software coordinates the timing of CCD readouts with shutter firings and filter moves, and performs all positional redundancy checks on the mechanical components. The TCS link is used both to obtain pointing and time stamp data for image headers, and also to send feedback to the telescope for focus changes, guiding corrections, and dithering moves. The software supports a primitive scripting capability, so users can design custom sequences suited to their observing or calibration needs (e.g., dither patterns, focus loops, filter/focus changes, flat field scripts).

Users operate the instrument from a second workstation located in the data room, which connects to the instrument host computer over the local intranet. Controls are issued through a simple command-line interface which requires a minimum of network bandwidth.

A more complex, GUI-based application is used to control the LFC guider. The software is a custom Tcl/Tk package written by T. Small, and permits the observer to fully control the guider. Typical guider functions are all supported, including guide image display/refresh (at a maximum

rate of 0.7 seconds/frame), exposure time adjustment and guide star selection. The user may also configure the guider to retain some hysteresis in the correction algorithm, and average the corrections over several guide frames in order to account for observing variables such as seeing or wind shake. Real time feedback on the observing conditions are logged for the user through a set of graphical strip charts recording the FWHM and total intensity of the guide star as proxies for the seeing and transparency. Further feedback on the telescope's tracking performance is provided on a radial plot that logs a history of the direction and magnitude of guide corrections. The FWHM of the guide star is typically somewhat larger than for objects on the science CCDs, due to the guide star's location in the periphery of the focal plane. As such, the guide FWHM is not an accurate absolute gague of the seeing, but it does provide relative feedback about temporal seeing variations. The guider is quite sensitive, allowing users to lock on stars with $g' = 18$, refreshing every few seconds.

The observer's workstation is also used for the display and analysis of images coming from the LFC with the observer's choice of software. These functions are the responsibility of the user; there is no default or real-time visualization of the images during readout. Although the LFC disk farm is attached to the instrument host computer, the display/analysis software is typically run locally on the user interface workstation, to avoid taxing the memory limits of the instrument host [1].

D.6 Performance

LFC has now been in operation for slightly over 3.5 years, logging some 200 nights on the P200. Its first year of operation saw many repairs and upgrades to improve mechanical reliability, and also to repair non-functioning CCDs. Since then, the instrument has undergone one significant round of servicing to improve the filter wheel mechanism.

D.6.1 Mechanical

The mechanical components of the instrument have performed at or near specification, although several failure modes of the shutter and filter wheel required attention in LFC's first year of duty.

At commissioning, LFC contained the largest fast focal plane shutter ever built. Focal plane shutters for other mosaic instruments were either cranked slowly by stepper motors or crashed into destructive hard stops with heavy-duty springs or bursts of compressed air. The air option was not available at the P200 prime focus, and we wished to avoid using hard stops, as these designs tend to require constant maintenance to replace the abused components. Our servo motor design has proven fairly reliable over time, although it did initially suffer from a major failure mode. These problems

[1] The Sun Ultra 1 instrument host currently holds the maximum amount of memory available for its architecture. Our Leach-II electronics use an SBus fiber optic interface card for the host computer (the PCI interface drivers were in their infancy at the time of commissioining). Hence, we cannot use later model workstations with larger memory capacities, since these lack SBus compatibility. Occasionally, allocation errors can lead to the loss of an exposure if the physical memory limits of the host computer are exceeded.

arose when high torques sheared a component coupling one of the motors to its drive screw. The torque was generated by inertial overshoot of the blade, which tripped a loose limit switch only when the telescope was in a particular gravity orientation. After several months of operation (and thousands of shutter cycles) the hard acceleration caused by this error condition caused one of the two shutter blades to fail. Much effort was expended in determining the root cause of this problem, although the camera was able to operate with only one of the two shutter blades in service for this period. Since the problem was identified and repaired the shutter has operated without malfunction.

Tests have shown that the shutter is extremely light-tight, and delivers gradient-free exposure times across the entire field (≤ 600 μs peak to peak for the minimum allowed exposure time). The original specifications for the shutter called for 0.5 second exposures and the motors could probably deliver these values. However, the CCD utility board requires an extra few tenths of a second to query the shutter position sensors for error conditions before firing a blade, to prevent collisions within the mechanism. In practice, the 0.6 second limit is short enough to permit exposures of bright ($\sim 11 - 12$ magnitude, for unbinned operation) standard stars without saturation, even in focus. On occasion users may want to defocus slightly to lower the count rate, but the adjustment need not be large.

The filter wheel mechanism has also encountered some slight problems, though no catastrophic failures. The wheel will sometimes get "lost" when its friction drive slips. Due to our constraints on the thickness of the combined shutter/filter wheel enclosure (to put the CCDs at the correct back focal distance), and the total size of instrument (to fit in the prime focus cage), we could not attach an absolute encoder to the filter wheel and were forced to operate it in open loop. Provided the initial open-loop move comes close to its requested position, a series of magnetic Hall-effect sensors can be used to adjust the wheel to an accurate final position. However, when the wheel slips significantly in its initial move, these sensors cannot find the Hall-effect magnets (embedded in the wheel) to perform the final adjustment. In these cases the wheel needs to be reset to its home position. This problem is especially apparent when the wheel is loaded with an imbalanced set of filters, creating a gravitational torque on the wheel when the telescope is at high airmass.

In Spring 2003 the Palomar engineering staff upgraded the design of the filter wheel mechanism, to make the wheel more rigid and better define its plane of motion. The original design only had the wheel supported by bearings on its central axle. Because the wheel is so large (over 2 feet across) it is subject to a large bending moment, causing a slight "wobble" of the wheel as it turns. This would sometimes lead to contact between the perimeter of the wheel and one of the shutter motor casings, since the clearance between these components is very tight. In the new servicing, further supports were added to restrain the wheel around its diameter, and eliminate the wobble. It is hoped that this will reduce the frequency with which the wheel needs re-homing.

D.6.2 Electronics/Software

During the first shipment of LFC to the mountain, 3 of the CCDs were damaged when the shuttle drove over a curb, so only 3 chips were available at first light. The damaged devices were replaced over the course of the next year. One of the replacement CCDs saturates at roughly half the light level of the other chips; this problem is thought to originate on the chip and not at analog-to-digital conversion. This chip has been positioned on the periphery of the array.

The CCDs otherwise perform reasonably well, aside from minor cosmetic defects. Bias frames show some pattern noise at the $\sim$ 10 DN level; this signal is likely to be related to electrical interference within the instrument and/or the P200 prime focus cage. The linearity of the CCDs is quite good over their whole dynamic range, although the gain and full-well capacity varies from device to device.

The most persistent electronics problem has been the Leach-II "utility" board. This board provides an interface for the CCD controller to the mechanical components, to coordinate shutter firings and filter changes with mosaic readouts. For unknown reasons the board will occasionally "hang" up to a few times per run. The only known solution to this problem is to reboot the electronics. Originally this required climbing into the prime focus cage, but the Palomar staff constructed a remote unit that permits the observing assistant to cycle LFC's power from the control room. With this fix a power cycle should only result in a few minutes of lost observing time.

The camera and guider software have both performed well. The only known failure mode of the guider happens when the home directory of the LFC user fills, in which case the guider freezes and TCS information stops being written to image headers. This can be fixed by clearing up space in the directory. The mosaic control software occasionally has problems when the LFC host computer runs out of memory allocation space, which can cause the loss of an exposure if it occurs during readout.

D.6.3 Optical

In Figure D.12 we show an example of a deep, stacked LFC I-band image. The image quality delivered by the camera is sub-arcsecond over the central 18-20 arcminutes of the field. Outside of this range, optical distortions quickly accumulate. M. Hunt has developed a special modification of the NOAO "mscred" IRAF scripts to astrometrically calibrate and stack LFC images. These scripts operate by comparing measured stellar centroids in the images with known positions from the USNO catalog. The offsets are used to calculate the geometric distortions of the optics and reproject the images onto an undistorted tangent plane for stacking.

Users report that it is fairly straightforward to produce distortion maps with small residuals in the central part of the field (the 18-20 arcminute area). It has been difficult to fit the residuals

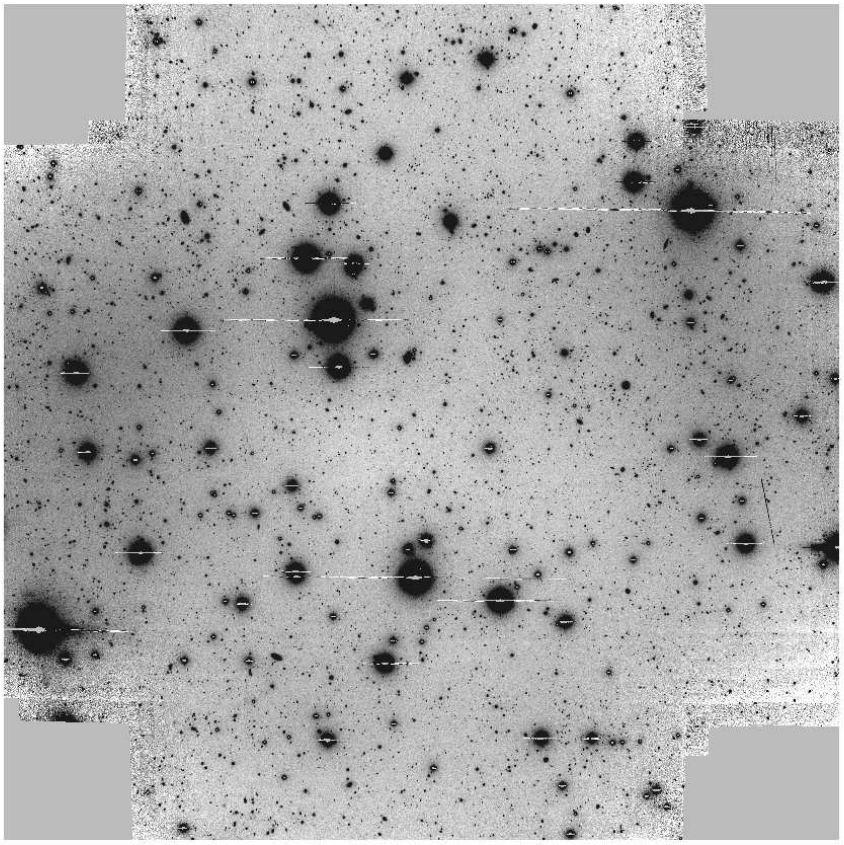

Figure D.12 Stacked mosaic of I band LFC images. Full 24 arcminute field is shown. (Courtesy of M. Hunt)

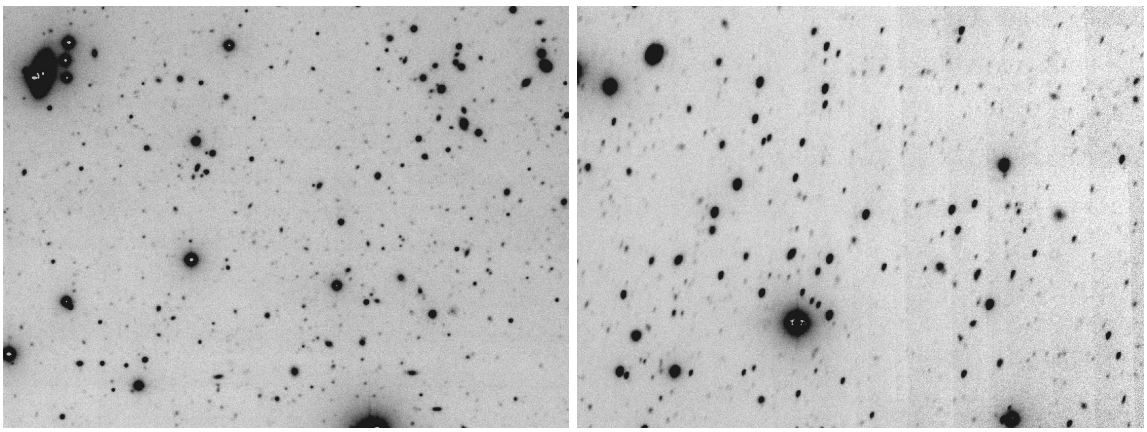

Figure D.13 Two enlarged potions of the same mosaic, each approximately 4.2×3.1 arcminutes. The left panel is taken from a point near the center of the mosaic, showing round images with 0.9 arseconds FWHM. The right panel is taked from the northwest corner of the mosaic (the upper right of Figure D.12), and illustrates the geometric distortion of point sources due to optical abberrations in the P200+Wynne system.

outside of this central region, because the standard IRAF routines use symmetric polynomials to solve for the distortion. The Wynne corrector's distortion pattern is not well suited to polynomial fits, since the map is quite flat over much of the field and quickly deteriorates at the edges. To fit the abrupt change, a high order polynomial is required, which can produce unstable solutions over the undistorted portions of the field if the density of stars for the fit is too sparse. Imaging of an astrometric field is therefore advisable as a calibration step for any LFC run. Ultimately a spline or "bspline" fit may be a better representation of the distortion, but these are not available in the present IRAF routines. In many cases, users have generated solutions which apply only to the central part of the field (since the outer portions were not needed for their science), or they have constructed separate solutions for the outer and inner portions of the field and merged these to make a master distortion map. With proper correction, the final RMS residuals across the field are generally $0.1 - 0.3$ arcseconds. The astrometry appears to be stable enough to design accurate slitmasks for LRIS.

LFC's throughput is best in the g' through i' range. In z', the image quality is quite good, but the detectors' quantum efficiency begins to tail off. The u' throughput was not as high as we had initially hoped, given the investment in UV sensitive CCDs. It appears that the u' sensitivity may be limited partly by telescope and site conditions. For example, at one point in the early operation of the LFC we had runs scheduled on either side of a re-aluminization of the primary. We found that the UV sensitivity improved by over 50% with the new surface, after no adjustments to the camera. However, u' images are also affected more than other bands by pattern noise in the electronics, which could probably be reduced with greater attention to interference sources (e.g., ground loops, stepper motor, switching power supply for shutter servos).

D.7 Summary

The LFC has provided the Palomar community with a dedicated wide field imager, at fairly low cost and fast turnaround time. Its design used the existing prime focus optics of the P200, but incorporated a new large shutter and filter wheel to accompany the mosaic of CCDs. The camera takes full advantage of the P200's field, though it is also subject to limitations imposed by the telescope and site (primary mirror pinch and coatings, and seeing). Following some early problems with the mechanical components and CCDs, LFC has performed fairly reliably. It is a logical addition to the complement of instruments for the observatory, and has been one of the most heavily used instruments at Palomar since its commissioning.

D.8 Team

- Mark Metzger: P.I., project management, CCDs, software, and electronics
- Rob Simcoe: Mechanical design, fabrication & assembly management, systems integration, and some machining
- John Yamasaki: Electronics design and construction
- Todd Small: Guider software
- Gaston Araya: Machining & fabrication

We also thank Rick Burruss for his efforts on the mountain during commissioning, and for his assistance in characterizing and documenting the performance of LFC on the telescope. This document makes use of several of his measurements. Further information about the instrument may be found at the following webpages:

- http://www.astro.caltech.edu/palomar/200inch/lfc/lfcopen.html
- http://www.astro.caltech.edu/∼ras/lfc/lfc.html

Bibliography

Abel, T., Bryan, G. L., & Norman, M. L. 2002, Science, 295, 93

Adelberger, K. L., Steidel, C. C., Shapley, A. E., & Pettini, M. 2003, ApJ, 584, 45

Aguirre, A., Hernquist, L., Schaye, J., Katz, N., Weinberg, D. H., & Gardner, J. 2001, ApJ, 561, 521

Aguirre, A., Schaye, J., & Theuns, T. 2002, ApJ, 576, 1

Bahcall, N. A. 1988, ARA&A, 26, 631

Barlow, T. A. & Sargent, W. L. W. 1997, AJ, 113, 136

Begelman, M. C. & Fabian, A. C. 1990, MNRAS, 244, 26P

Benjamin, R. A., Benson, B. A., & Cox, D. P. 2001, ApJ, 554, L225

Benson, A. J., Frenk, C. S., Baugh, C. M., Cole, S., & Lacey, C. G. 2001, MNRAS, 327, 1041

Bergeron, J., Aracil, B., Petitjean, P., & Pichon, C. 2002, A&A, 396, L11

Boksenberg, A., Sargent, W. L. W., & Rauch, M. 2003, astro-ph/0307557

Boyle, B. J., Griffiths, R. E., Shanks, T., Stewart, G. C., & Georgantopoulos, I. 1993, MNRAS, 260, 49

Bromm, V., Coppi, P. S., & Larson, R. B. 2002, ApJ, 564, 23

Bromm, V., Ferrara, A., Coppi, P. S., & Larson, R. B. 2001, MNRAS, 328, 969

Burles, S. & Tytler, D. 1996, ApJ, 460, 584

Carswell, B., Schaye, J., & Kim, T. 2002, ApJ, 578, 43

Cen, R., Miralda-Escude, J., Ostriker, J. P., & Rauch, M. 1994, ApJ, 437, L9

Cen, R. & Ostriker, J. P. 1999, ApJ, 514, 1

Cen, R. & Simcoe, R. A. 1997, ApJ, 483, 8

Cen, R., Tripp, T. M., Ostriker, J. P., & Jenkins, E. B. 2001, ApJ, 559, L5

Chaffee, F. H., Foltz, C. B., Bechtold, J., & Weymann, R. J. 1986, ApJ, 301, 116

Chen, X., Weinberg, D., Katz, N., & Davé, R. 2002, astro-ph/0203319

Connolly, A. J., Scranton, R., Johnston, D., Dodelson, S., Eisenstein, D. J., Frieman, J. A., Gunn, J. E., Hui, L., Jain, B., Kent, S., Loveday, J., Nichol, R. C., O'Connell, L., Postman, M., Scoccimarro, R., Sheth, R. K., Stebbins, A., Strauss, M. A., Szalay, A. S., Szapudi, I., Tegmark, M., Vogeley, M. S., Zehavi, I., Annis, J., Bahcall, N., Brinkmann, J., Csabai, I., Doi, M., Fukugita, M., Hennessy, G. S., Hindsley, R., Ichikawa, T., Ivezić, Ž., Kim, R. S. J., Knapp, G. R., Kunszt, P., Lamb, D. Q., Lee, B. C., Lupton, R. H., McKay, T. A., Munn, J., Peoples, J., Pier, J., Rockosi, C., Schlegel, D., Stoughton, C., Tucker, D. L., Yanny, B., & York, D. G. 2002, ApJ, 579, 42

Cowie, L. L. & Songaila, A. 1998, Nature, 394, 44

Cowie, L. L., Songaila, A., Kim, T., & Hu, E. M. 1995a, AJ, 109, 1522

—. 1995b, AJ, 109, 1522

Davé, R., Cen, R., Ostriker, J. P., Bryan, G. L., Hernquist, L., Katz, N., Weinberg, D. H., Norman, M. L., & O'Shea, B. 2001, ApJ, 552, 473

Davé, R., Hellsten, U., Hernquist, L., Katz, N., & Weinberg, D. H. 1998, ApJ, 509, 661

Davé, R., Hernquist, L., Katz, N., & Weinberg, D. H. 1999, ApJ, 511, 521

Dawson, S., Spinrad, H., Stern, D., Dey, A., van Breugel, W., de Vries, W., & Reuland, M. 2002, ApJ, 570, 92

Dickinson, M., Papovich, C., Ferguson, H. C., & Budavári, T. 2003, ApJ, 587, 25

Dopita, M. A. & Sutherland, R. S. 1996, ApJS, 102, 161

Edgar, R. J. & Chevalier, R. A. 1986, ApJ, 310, L27

Ellison, S. L., Songaila, A., Schaye, J., & Pettini, M. 2000, AJ, 120, 1175

Ellison, S. L., Yan, L., Hook, I. M., Pettini, M., Wall, J. V., & Shaver, P. 2001, A&A, 379, 393

Fang, T. & Bryan, G. L. 2001, ApJ, 561, L31

Fang, T., Marshall, H. L., Lee, J. C., Davis, D. S., & Canizares, C. R. 2002, ApJ, 572, L127

Feigelson, E. D. & Nelson, P. I. 1985, ApJ, 293, 192

Ferland, G. J., Korista, K. T., Verner, D. A., Ferguson, J. W., Kingdon, J. B., & Verner, E. M. 1998, PASP, 110, 761

Franx, M., Illingworth, G. D., Kelson, D. D., van Dokkum, P. G., & Tran, K. 1997, ApJ, 486, L75+

Giavalisco, M., Steidel, C. C., Adelberger, K. L., Dickinson, M. E., Pettini, M., & Kellogg, M. 1998, ApJ, 503, 543

Grevesse, N. & Sauval, A. J. 1998, Space Science Reviews, 85, 161

Haardt, F. & Madau, P. 1996, ApJ, 461, 20

Haardt, F. & Madau, P. 2001, in Clusters of Galaxies and the High Redshift Universe Observed in X-rays

Haehnelt, M. G., Steinmetz, M., & Rauch, M. 1996, ApJ, 465, L95+

Heckman, T. M., Sembach, K. R., Meurer, G. R., Strickland, D. K., Martin, C. L., Calzetti, D., & Leitherer, C. 2001, ApJ, 554, 1021

Heger, A. & Woosley, S. E. 2002, ApJ, 567, 532

Hellsten, U., Hernquist, L., Katz, N., & Weinberg, D. H. 1998, ApJ, 499, 172

Hernquist, L., Katz, N., Weinberg, D. H., & Jordi, M. 1996, ApJ, 457, L51+

Jannuzi, B. T., Bahcall, J. N., Bergeron, J., Boksenberg, A., Hartig, G. F., Kirhakos, S., Sargent, W. L. W., Savage, B. D., Schneider, D. P., Turnshek, D. A., Weymann, R. J., & Wolfe, A. M. 1998, ApJS, 118, 1

Kells, W., Dressler, A., Sivaramakrishnan, A., Carr, D., Koch, E., Epps, H., Hilyard, D., & Pardeilhan, G. 1998, PASP, 110, 1487

Kennicutt, R. C., Tamblyn, P., & Congdon, C. E. 1994, ApJ, 435, 22

Kim, T., Hu, E. M., Cowie, L. L., & Songaila, A. 1997, AJ, 114, 1

Kim, T.-S., Cristiani, S., & D'Odorico, S. 2001, A&A, 373, 757

Lavalley, M., Isobe, T., & Feigelson, E. 1992, in ASP Conf. Ser. 25: Astronomical Data Analysis Software and Systems I, 245–+

Le Fevre, O., Hudon, D., Lilly, S. J., Crampton, D., Hammer, F., & Tresse, L. 1996, ApJ, 461, 534

Leach, R. W., Beale, F. L., & Eriksen, J. E. 1998, in Proc. SPIE Vol. 3355, p. 512-519, Optical Astronomical Instrumentation, Sandro D'Odorico; Ed., 512–519

Lehnert, M. D. & Heckman, T. M. 1996, ApJ, 462, 651

Loveday, J., Maddox, S. J., Efstathiou, G., & Peterson, B. A. 1995, ApJ, 442, 457

Lu, L., Sargent, W., Barlow, T., & Rauch, M. 1998, astro-ph/9802189

Mackey, J., Bromm, V., & Hernquist, L. 2003, ApJ, 586, 1

Madau, P., Ghisellini, G., & Fabian, A. C. 1994, MNRAS, 270, L17+

Martin, C. L., Kobulnicky, H. A., & Heckman, T. M. 2002, ApJ, 574, 663

McDonald, P., Miralda-Escudé, J., Rauch, M., Sargent, W. L. W., Barlow, T. A., Cen, R., & Ostriker, J. P. 2000, ApJ, 543, 1

Meyer, D. M. & York, D. G. 1987a, ApJ, 315, L5

—. 1987b, ApJ, 315, L5

Miralda-Escude, J., Cen, R., Ostriker, J. P., & Rauch, M. 1996, ApJ, 471, 582

Mulchaey, J. S., Mushotzky, R. F., Burstein, D., & Davis, D. S. 1996, ApJ, 456, L5+

Nicastro, F., Zezas, A., Drake, J., Elvis, M., Fiore, F., Fruscione, A., Marengo, M., Mathur, S., & Bianchi, S. 2002, ApJ, 573, 157

Norberg, P., Baugh, C. M., Hawkins, E., Maddox, S., Peacock, J. A., Cole, S., Frenk, C. S., Bland-Hawthorn, J., Bridges, T., Cannon, R., Colless, M., Collins, C., Couch, W., Dalton, G., De Propris, R., Driver, S. P., Efstathiou, G., Ellis, R. S., Glazebrook, K., Jackson, C., Lahav, O., Lewis, I., Lumsden, S., Madgwick, D., Peterson, B. A., Sutherland, W., & Taylor, K. 2001, MNRAS, 328, 64

O'Meara, J. M., Tytler, D., Kirkman, D., Suzuki, N., Prochaska, J. X., Lubin, D., & Wolfe, A. M. 2001, ApJ, 552, 718

Ostriker, J. P. & Gnedin, N. Y. 1996, ApJ, 472, L63+

Petitjean, P., Mueket, J. P., & Kates, R. E. 1995, A&A, 295, L9

Pettini, M., Rix, S. A., Steidel, C. C., Adelberger, K. L., Hunt, M. P., & Shapley, A. E. 2002, ApJ, 569, 742

Pettini, M., Shapley, A. E., Steidel, C. C., Cuby, J., Dickinson, M., Moorwood, A. F. M., Adelberger, K. L., & Giavalisco, M. 2001, ApJ, 554, 981

Prochaska, J. X., Howk, J. C., & Wolfe, A. M. 2003, Nature, 423, 57

Prochaska, J. X. & Wolfe, A. M. 2000, ApJ, 533, L5

Qian, Y.-Z., Sargent, W. L. W., & Wasserburg, G. J. 2002, ApJ, 569, L61

Rauch, M., Haehnelt, M. G., & Steinmetz, M. 1997a, ApJ, 481, 601

—. 1997b, ApJ, 481, 601

Rauch, M., Miralda-Escude, J., Sargent, W. L. W., Barlow, T. A., Weinberg, D. H., Hernquist, L., Katz, N., Cen, R., & Ostriker, J. P. 1997c, ApJ, 489, 7

Rauch, M., Sargent, W. L. W., & Barlow, T. A. 2001, ApJ, 554, 823

Rauch, M., Sargent, W. L. W., Barlow, T. A., & Simcoe, R. A. 2002, ApJ, 576, 45

Rauch, M., Sargent, W. L. W., Womble, D. S., & Barlow, T. A. 1996a, ApJ, 467, L5+

—. 1996b, ApJ, 467, L5+

Richter, P., Savage, B. D., Wakker, B. P., Sembach, K. R., & Kalberla, P. M. W. 2001, ApJ, 549, 281

Rollinde, E., Petitjean, P., & Pichon, C. 2001, A&A, 376, 28

Salpeter, E. E. 1955, ApJ, 121, 161

Sargent, W. L. W., Steidel, C. C., & Boksenberg, A. 1988, ApJS, 68, 539

Sargent, W. L. W., Young, P. J., Boksenberg, A., & Tytler, D. 1980, ApJS, 42, 41

Savage, B. D., Sembach, K. R., Tripp, T. M., & Richter, P. 2002, ApJ, 564, 631

Schaye, J. 2001, ApJ, 559, 507

Schaye, J., Aguirre, A., Kim, T.-S., Theuns, T., Rauch, M., & Sargent, W. L. W. 2003, astro-ph/0306000

Schaye, J., Rauch, M., Sargent, W. L. W., & Kim, T. 2000, ApJ, 541, L1

Schmitt, J. H. M. M. 1985, ApJ, 293, 178

Scott, J., Bechtold, J., Dobrzycki, A., & Kulkarni, V. P. 2000, ApJS, 130, 67

Shapley, A. E., Steidel, C. C., Adelberger, K. L., Dickinson, M., Giavalisco, M., & Pettini, M. 2001, ApJ, 562, 95

Simcoe, R. A., Sargent, W. L. W., & Rauch, M. 2002, ApJ, 578, 737

Songaila, A. 2001, ApJ, 561, L153

Songaila, A. & Cowie, L. L. 1996, AJ, 112, 335

Spergel, D. N., Verde, L., & Other, P. 2003, astro-ph

Springel, V. & Hernquist, L. 2003, MNRAS, 339, 289

Steidel, C. C., Adelberger, K. L., Dickinson, M., Giavalisco, M., Pettini, M., & Kellogg, M. 1998, ApJ, 492, 428

Strickland, D. 2001, astro-ph/0107116

Sutherland, R. S. & Dopita, M. A. 1993, ApJS, 88, 253

Telfer, R. C., Zheng, W., Kriss, G. A., & Davidsen, A. F. 2002, ApJ, 565, 773

Tripp, T. M., Giroux, M. L., Stocke, J. T., Tumlinson, J., & Oegerle, W. R. 2001, ApJ, 563, 724

Tripp, T. M. & Savage, B. D. 2000, ApJ, 542, 42

Tripp, T. M., Savage, B. D., & Jenkins, E. B. 2000, ApJ, 534, L1

Turnshek, D. A. 1984, ApJ, 280, 51

Tytler, D. & Fan, X. 1992, ApJS, 79, 1

Tytler, D., Fan, X.-M., Burles, S., Cottrell, L., Davis, C., Kirkman, D., & Zuo, L. 1995, in QSO Absorption Lines, Proceedings of the ESO Workshop Held at Garching, Germany, 21 - 24 November 1994, edited by Georges Meylan. Springer-Verlag Berlin Heidelberg New York. Also ESO Astrophysics Symposia, 1995., p.289, 289–+

Venemans, B. P., Kurk, J. D., Miley, G. K., Röttgering, H. J. A., van Breugel, W., Carilli, C. L., De Breuck, C., Ford, H., Heckman, T., McCarthy, P., & Pentericci, L. 2002, ApJ, 569, L11

Wardle, M. & Knapp, G. R. 1986, AJ, 91, 23

Weinberg, D. H., Miralda-Escude, J., Hernquist, L., & Katz, N. 1997, ApJ, 490, 564

Weymann, R. J., Carswell, R. F., & Smith, M. G. 1981, ARA&A, 19, 41

Woosley, S. E. & Weaver, T. A. 1995, ApJS, 101, 181

Wynne, C. G. 1967, Appl. Opt., 6, 1227

Zhang, Y., Anninos, P., & Norman, M. L. 1995, ApJ, 453, L57+

Zheng, W., Kriss, G. A., Telfer, R. C., Grimes, J. P., & Davidsen, A. F. 1997, ApJ, 475, 469